Characterisation of luminescent and electrochemical sensors.

Blair, Stephanie

University of DURHAM

Department of Chemistry

Characterisation of Luminescent and Electrochemical Sensors.

Stephanie Blair

A thesis submitted for the degree of Doctor of Philosophy

2001

Declaration

The work described herein was carried out in the Department of Chemistry at the University of Durham between October 1998 and September 2001. All the work is my own, unless stated to the contrary, and it has not been submitted for a degree at this or any other university.

Statement of Copyright

"The grand essentials of happiness are: something to do, something to love, and something to hope for."

Allan K. Chalmers

To Mum, Dad, Samantha and Paul.

Acknowledgements

I am grateful for the assistance of many people in the completion of this work. I would particularly like to acknowledge the following people:

I would like to say a huge thank you to Professor David Parker and Dr. Ritu Kataky, for their guidance, encouragement and help during my three years at Durham. I have enjoyed working with you both and will miss being part of the group!

I would also like to thank the support staff , especially Neil for making my flow-cells and Alan for the 'recovery' of the computer, after having crashed it again!

I would like to thank all the Parker and Kataky group members past and present for providing me with their valuable compounds, entertainment, a shoulder to moan on during the Ph.D. blues and also for their friendship. I would especially like to thank Dr. Rachel Dickins, Dr. Mark Lowe and Dr. James Bruce for all their help. A huge thanks to Mark O'Halloran for being a good friend and drinking buddy and being my (extremely bad) ballroom dancing partner. See you down South! Finally I would like to thank Meryl, Debbie and Ollie for being super-duper friends. Debs I'm going to miss you pal!

I would also like to thank Ingrid, the best friend a girl could have, for keeping me sane and for being there. Also thanks to my other 'weigie' drinking partners... Catriona and Jenny for providing me with regular doses of entertainment! I would also like to thank John for his love, friendship.....and excellent holiday location!

Finally, the biggest thanks of all are for my family; who are my mum Sarah, dad David, sister Samantha and brother-in-law Paul. Thank you all for your love and support and not forgetting your money. Thanks to my super mum for always having the right things to say on tap! and to my dad for telling me the best thing I could give myself was an education .....I love you all very much.x.

Abstract

This thesis is concerned with electrochemical and optical sensors based on potentiometric and luminescent transduction.

A series of oxa-diisobutylamide derivatives based on *cis-cis*-1,3,5-cyclo-hexanetriol was compared in standard polyvinyl chloride based ion-selective electrodes as ionophores for the detection of selected IA/IIA cations. The tripodal framework incorporated either mono-, di- or tri- substituted diisobutyl amide pendant groups to give possible coordination numbers of 4, 5 and 6 respectively, assuming a 1:1 cation:ionophore stoichiometry.

A Nernstian response towards the detection of Ca^{2+} was observed with the ISE incorporating the di-substituted diamide analogue. The selectivity of the ISE was assessed using the Fixed Interference Method and a Nernstian response was observed in the extracellular Ca^{2+} concentration range (1.16 – 1.32 mmol dm^{-3}) in the presence of a simulated extracellular background of interfering cations. The effect of pH on the response of the ISE was also investigated as was the enhancement of the lower detection limit by including a Ca^{2+} buffer in the inner filling electrolyte.

Luminescent lanthanide complexes were assessed as chemical transducers for the purpose of optical sensing of pH or dissolved oxygen, following immobilisation in sol-gel thin films prepared in acidic media.

pH-dependent intensity or ratiometric methods were defined for europium and terbium complexes of cyclen based frameworks (12-N_4). These systems incorporated phenanthridine derivatives or para substituted aryl sulfonamide moieties as the sensitising chromophores, typically with apparent pH sensing ranges of 5.5 to 8.0.

Dissolved oxygen-dependent modulation of the metal emission and excited state lifetime of a short series of terbium complexes was assessed. These systems were based on cyclen with either tetra-amide or mono-amide triphosphinate pendent groups.

Contents.

Abbreviations.

ATP	adenosine 5'-triphosphate
ADP	adenosine 5'-diphosphate
BBPA	bis(1-butylpentyl)adipate
BET	back energy transfer
BTB	bromothymol blue
DBP	dibutyl phthalate
CVD	constant volume dilution
DO	dissolved oxygen
DOS	bis(2-ethylhexyl)sebacate
DVM	digital voltmeter
EMF	electromotive force
ETEOS	ethyltriethoxysilane
ETH1001	(-)-(R,R)-N,N'-bis[11-(ethoxy-carbonyl)undecyl]-N,N'-4,5-tetramethyl-3,6-dioxaoctanediamide
FIM	fixed interference method
FNDPE	2-fluorophenyl 2-nitrophenyl ether
HCL	hydrochloric acid
HF	hydrofluoric acid
IC	internal conversion
ISC	inter system crossing
ISE	ion selective electrode
IUPAC	international union of pure and applied chemistry
KTpClPB	potassium tetrakis(4-chlorophenyl)borate
LED	light emitting diode
LMCT	ligand to metal charge transfer
LPJ	liquid junction potential
MPM	matched potential method
MSM	mixed solution method
MTEOS	methyltriethoxysilane
NaTFPB	sodium tetrakis[3,5-bis(trifluoromethyl)phenyl]borate
NaTPB	sodium tetraphenylborate

NHE	standard hydrogen electrode
o-NPOE	2-nitrophenyl octyl ether
PET	photo electron transfer
PVC	poly(vinyl chloride)
RTP	room temperature phosphorescence
SSM	separate solution method
TEOS	tetraethoxysilane
TMOS	tetramethoxysilane
VR	vibrational relaxation

Chapter 1
Introduction.

This chapter is a general introduction and describes basic concepts of potentiometric and fluorimetric chemical sensing and sol-gel technology. Brief reviews of sensing species for the purpose of optical pH and oxygen sensing are also reported.

1.1 Chemical Sensing.

Typical chemical sensors used to detect any kind of analyte tend to consist of two components, a recognition site selective towards the analyte and a transducer to translate the recognition event.[1] Recognition of the analyte can occur through some form of chemical reaction, such as complex formation, protonation or quenching of a fluorescent excited state. This chemical reaction then signals a change, for example in the electrical potential at a surface or the emission of fluorescent light to which the transducer responds. Its magnitude is translated into a measure of the amount of analyte detected. Chemical sensors can be grouped according to their means of transduction. This thesis is concerned with electrochemical and optical sensors based on potentiometric and luminescent transduction.

1.1.1 General Principles of Potentiometric PVC Based Cation Ion–Selective Electrodes.

The first liquid membrane ion selective electrode (ISE) to determine the activity of calcium ions in solution was reported in 1967.[2] Three years later *Moody et al*[3] used poly(vinyl chloride) (PVC) to produce a polymer film with enhanced sensing properties for calcium, compared to the original liquid membrane. Since then PVC based ISEs have formed one of the most important and commercially useful groups of analytical chemical sensors. Unlike other analytical applications such as Flame Emission Spectrophotometry that can measure the concentration of metal cations in solution, ISEs are advantageous as they can measure the activity of these ions.[4]

1.1.2 Concept of Activity.

In order for an ion to react either in solution or at the surface of an electrode, energy is required to free it from the surrounding sphere of oppositely charged ions. This results in a loss of energy of the system and a decrease in the chemical potential of the ion compared to its free state. As the density of the sphere is expected to be greater in solutions of high concentration, then so is the loss of chemical potential of the ion compared to that in an ideal solution. Hence to accurately describe the thermodynamic properties of dissolved ions, the activity of an ion has to be considered. As the analytical chemist is generally interested in the concentration of the ions in solution, it is important to understand the relationship between the activity, a_i, and the concentration of the ion, c_i. The relationship between concentration and activity is given in Equation 1.1.

$$a_i = \gamma_i \cdot c_i \qquad \textbf{Equ 1.1}$$

a_i activity of the ion.

γ_i activity coefficient of the ion.

c_i concentration of the ion (molarity, molality or mole fraction).

Fundamentally, the chemical potential is the change in free energy of a system when one mole of uncharged species *i* is added to an infinitely large quantity of the system, so that the overall composition of the system is held constant.[5] In an ideal solution the chemical potential of a species of type *i* can be described as,

$$\mu_i = \mu_i^{\circ} + RT \ln x_i \qquad \textbf{Equ 1.2}$$

μ_i chemical potential.

μ_i^o chemical potential (under standard conditions).

R universal gas constant.

T absolute temperature.

x_i mole fraction.

In a non-ideal solution, concentration is corrected for activity to account for interactions between the central ion and its surrounding ionic sphere.

$$\mu_i = \mu_i^\circ + RT \ln a_i \qquad \textbf{Equ 1.3}$$

$$= \mu_i^\circ + RT \ln x_i \gamma_i \qquad \textbf{Equ 1.4}$$

$$= \mu_i^\circ + RT \ln x_i + RT \ln \gamma_i \qquad \textbf{Equ 1. 5}$$

$$= \mu_i^\circ + RT \ln x_i + N_A U \qquad \textbf{Equ 1.6}$$

N_A Avagadro's number.

U potential energy associated with the surrounding ion sphere.

The expressions for ionic activity coefficients in Equations 1.4 and 1.5 are given for a single ion, however as single ion activities cannot be determined experimentally, activity coefficients are expressed as the mean activity coefficient for the electrolyte γ_{xy}.

$$\gamma_{xy}^{\ 2} = \gamma_+ \cdot \gamma_- \qquad \text{for NaCl.}$$

$$\gamma_{xy}^{\ 3} = \gamma_+ \cdot \gamma_-^{\ 2} \qquad \text{for } MgCl_2.$$

In Equation 1.5 the term $RT \ln \gamma_i$, corrects the ideal equation for the presence of the surrounding ionic sphere, and it is indeed related to U and the ionic strength of the solution through Debye-Huckel theory to give Equation 1.7.[6]

$$\log \gamma_{xy} = -A|z_+ \cdot z_-|I^{0.5} \qquad \textbf{Equ 1.7}$$

A Debye-Huckel constant, (~ 0.5/(mol kg^{-1})$^{0.5}$ for an aqueous solution at 25°C).

z_+, z_- charge on the cation and anion respectively.

I ionic strength.

$$I = 0.5\sum_i c_i z_i^2 \qquad \textbf{Equ 1.8}$$

Equation 1.7 is limiting to solutions with a concentration of less than or equal to 10^{-3} mol dm^{-3} (10^{-2} mol dm^{-3} in the case of multicharged electrolytes). The corrected Debye-Huckel equation for concentrations up to 10^{-2} mol dm^{-3} is given by Equation 1.9.

$$\log \gamma_{xy} = \frac{-A|z_+ \cdot z_-|I^{0.5}}{1 + BaI^{0.5}} \qquad \textbf{Equ 1.9}$$

Where

$$B = \sqrt{\frac{8\pi e^2 d_0 N_A}{DkT}} \qquad \textbf{Equ 1.10}$$

B a measure of the closest approach of the ions.

α ion size parameter.

D solvent dielectric constant.

d_0 solvent density.

For ionic strengths exceeding 10^{-2} mol dm^{-3}, the Guggenheim empirical correction[7] to Equation 1.9 can be used to describe the evaluation of activity coefficients more accurately up to an ionic strength of 0.1 mol dm^{-3}.

$$\log \gamma_{xy} = \frac{-A|z_+ \cdot z_-|I^{0.5}}{1 + BaI^{0.5}} + bI \qquad \textbf{Equ 1.11}$$

b a solute/solvent specific parameter characterising the solvation of the ions.

The terms A and B in the Debye-Huckel equations are constants that vary with the temperature, density and dielectric constant of the solvent. Where the ionic strength is greater than 0.1 mol dm^{-3} i.e. in seawater and blood, the Pitzer formalism for exceeding

the concentration limit associated with the Guggenheim convention, has been investigated.[8]

To fix the relationship between activity and concentration, a high concentration of inert electrolyte can be added to the sample solution. This has the effect of masking minor variations in the sample composition by producing a constant ionic strength background. Stabilization of the mean activity coefficient in this way allows the electrode to be used directly for concentration measurements.

1.1.3 Components of The Electrochemical Cell.

The potentiometric response of an ISE can be measured under galvanic conditions by incorporating the ISE as a half-cell in the electrochemical cell shown in Figure 1.1.

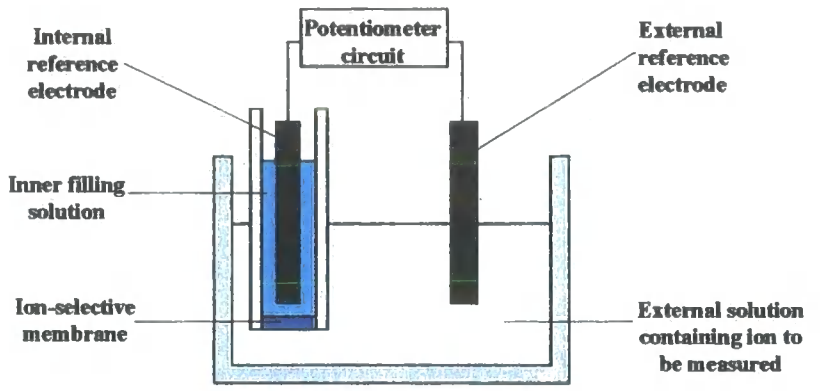

Figure 1.1: The electrochemical cell incorporating an ISE. (IFS = inner filling solution).

The typical cell assembly consists of the components:

1: The reference electrode and liquid junction assembly.

2: The sample solution.

3: The ion-selective electrode.

The reference electrode half-cell assembly is assumed to provide a constant potential against which changes in the ion-selective potential in different samples can be measured. The potential of the reference half-cell consists of the reference electrode potential as well as the potentials formed across the liquid junctions. The liquid junction potential at the sample/bridge electrolyte interface prohibits the true determination of single ion activities using ISEs. Although it is assumed to be independent of the sample composition and can be kept reasonably constant under specific conditions, its instability can be an important source of error in the potentiometric response of an ISE. The ideal measured cell potential or the electromotive force (EMF) is given by Equation 1.12.

$$EMF = E^o + E_M \qquad \textbf{Equ 1.12}$$

E^o is a constant parameter made up from contributions from the ion-selective inner filling solution, E_{IR}, the external reference electrode potential, E_{ER}, and the liquid junction potentials, E_{LJ}.

$$E^o = E_{IR} + E_{ER} + E_{LJ} \qquad \textbf{Equ 1.13}$$

The ion-selective membrane potential, E_M, is composed of three fundamental components; two boundary interfacial potentials, E_B', and, E_B'', and the internal membrane potential difference or diffusion potential, E_D.

$$E_M = E_{B'} + E_{B''} + E_D \qquad \textbf{Equ 1.14}$$

The diffusion potential is accepted to be negligible in most practical cases unless significant concentration gradients of ions with different mobilities arise within the membrane.[9] The boundary potential, E_B'', which is formed at the membrane inner filling solution interface, is assumed to be independent of the sample composition, and is therefore constant. Therefore, it is the boundary potential, E_B', which is formed at the membrane sample solution interface, which governs the response of the ISE and it is reflected in the EMF of the cell.

At the sample membrane interface, there is a region where electroneutrality does not hold and sample dependent changes can occur. E_B' arises from the absorption of the ion at this interface[10] and can be derived from basic thermodynamics. The chemical potential of a species in a non-ideal solution was given by Equation 1.3.

$$\mu_i = \mu_i^{\circ} + RT \ln a_i \qquad \textbf{Equ 1.3}$$

This equation can be extended further to account for the electrostatic forces between the charges of ionic species. Ions generate an electrical potential, ϕ, due to their charge, z_i. Following the addition of one mole of ions, additional changes in the free energy of the system can be defined as $z_i \phi$. The resultant contribution to the energy of a system from a transfer of matter and charge is known as the electrochemical potential.

$$\bar{\mu}_i = \mu_i + z_i F \phi \qquad \textbf{Equ 1.15}$$

For each phase of the interface the electrochemical potential can be described as:

$$\bar{\mu}_i(aq) = \mu_i(aq) + z_i F\phi(aq) = \mu_i^{\circ}(aq) + RT \cdot \ln a_i(aq) + z_i F\phi(aq) \qquad \textbf{Equ 1.16}$$

$$\bar{\mu}_i(org) = \mu_i(org) + z_i F\phi(org) = \mu_i^{\circ}(org) + RT \cdot \ln a_i(org) + z_i F\phi(org) \qquad \textbf{Equ 1.17}$$

$\bar{\mu}_i$ electrochemical potential.

μ_i chemical potential.

z_i valency of the primary ion.

F Faraday constant.

ϕ electrical potential.

μ_i^o chemical potential (under standard conditions).

R universal gas constant.

T absolute temperature.

Assuming relatively fast interfacial ion transfer and ion-ionophore interactions, the membrane interface is assumed to be in chemical equilibrium with the 'local' aqueous sample. Therefore, both the aqueous and organic electrochemical potentials are assumed to be equal and E_B' can be expressed as:

$$E_{B'} = \Delta\phi = \frac{-\mu_i^{\circ}(org) - \mu_i^{\circ}(aq)}{z_i F} + \frac{RT}{z_i F} \cdot \ln \frac{a_i(aq)}{a_i(org)} \qquad \textbf{Equ 1.18}$$

The activity coefficients for all ionic species within the membrane bulk are assumed to be constant due to the presence of lipophilic anions within the membrane.[11] Therefore, $a_i(org)$ is also assumed to be constant and can be combined with all other sample-independent potential parameters in the constant term E^{o}. Equation 1.18 is therefore reduced to the Nernst equation.

$$E_M = E^{o} + \frac{RT}{zF} \cdot \ln a_i(aq) \qquad \textbf{Equ 1.19}$$

A Nernstian response occurs when the membrane responds ideally over a range of activity of the primary ion. The response of a membrane can be observed by plotting the EMF vs the negative logarithm of a_i. If the plot is linear with a slope of $2.303RT/z_iF$ ($59.16/z_i$ mV per unit change with $-\log a_i$ at 298.15 K), then the membrane is responding ideally. However, quite often the response is described as Nernstian when the constant of proportionality deviates from the ideal response by ± 5mV.[4]

1.1.4 Selectivity.

Selectivity is the most important feature of a potentiometric sensor.[12] In practice the membrane can be sensitive to other ions in the sample as well as the primary ion. In mixed ion samples the membrane potential therefore has contributions from both the primary ion and the interfering ion, a_j For a mixed ion response the membrane potential is described by the semi-empirical Nicolskii-Eisenman equation,[13] where the

activity term in the Nernst equation is replaced by a sum of selectivity-weighed activities.

$$E = E^{o}_{i} + \frac{RT}{z_i F} \ln\left[a_i + \sum K_{ij}^{pot} a_j^{z_i/z_j} \right] \qquad \textbf{Equ 1.20}$$

K_{ij}^{pot} The potentiometric selectivity coefficient that describes the degree of selectivity of the membrane for the primary ion with respect to the interfering ion.

The selectivity coefficient is not a constant but an experimental value. The smaller the value of K_{ij}, the larger the amount of interfering ion activity that can be tolerated without perturbing the measurement of the primary ion activity to a significant extent. Selectivity coefficients can be determined according to IUPAC recommendations using three different methodologies.[14] Traditional methods are:

(1) The Separate Solution Method (SSM).
The EMF of the cell is measured in separate solutions of primary ion and interfering ion of the same concentration.

(2) The Fixed Interference Method (FIM).
The EMF of the cell is measured under standard addition when the concentration of the primary ion is varied in a background of interfering ion of constant concentration.

Many authors are aware that rarely do these traditional methods report the same selectivity coefficients from their respective data sets. Although the Nicolskii-Eisenman equation has been used for many years, it has a number of drawbacks that have only recently been addressed.[1,4,6,7,9,15]

The fundamental flaw in the calculation of selectivity coefficients with the SSM and the FIM lie in the theoretical assumption of the Nicolskii-Eisenman equation, that it

demands a Nernstian response for all ions measured including those interfering.[14] However, neither of these traditional procedures specifically require this condition with respect to the interfering ion response. The SSM depends on a single concentration measurement and the FIM is also a one-point measurement for the interfering solution. Although both methods yield information concerning the primary ion response, they fail to give information about the interfering ion response. Even with this in mind, rarely do 'real world' ISEs respond in a Nernstian manner towards highly discriminated ions, and non-Nernstian slopes are often non-reproducible.

Another problem associated with the Nicolskii-Eisenman equation is that it fails to yield the response in mixed solutions, where the ions that make a significant contribution to the EMF, have different valencies. The crux of this problem stems from the exponent $a_i^{Zi/Zj}$, which means the Nicolskii-Eisenman equation is non-symmetrical for ions that bear different charges i.e. a different EMF is obtained when the primary ion is treated as the interfering ion and vice versa.[12,13,16,17] This is because the equation was established in the late 30's to measure the interference of monovalent ions towards the glass electrode.[18] However, many researchers around the world have now adopted it to characterize all ISEs. As a result of these drawbacks associated with the Nicolskii-Eisenman equation, more authors are choosing empirical methods to determine membrane selectivity.

Empirical membrane selectivity can be calculated using the Matched Potential Method (MPM). This method was introduced by Gadzelepo and Christian[19] and is now recommended by IUPAC as a method for determining membrane selectivity. In practice the EMF of the membrane is measured in a reference solution of constant primary ion activity. The primary ion activity is then increased by Δa_i. Interfering ions are then added to an identical reference solution until the EMF matches that following the addition of the primary ion to the reference solution. The selectivity coefficient is then calculated as the ratio of the changes in the activity of the primary ion and the interfering ion for that respective potential change.

$$K_{ij}^{MPM} = \Delta a_i / \Delta a_j \qquad \textbf{Equ 1.21}$$

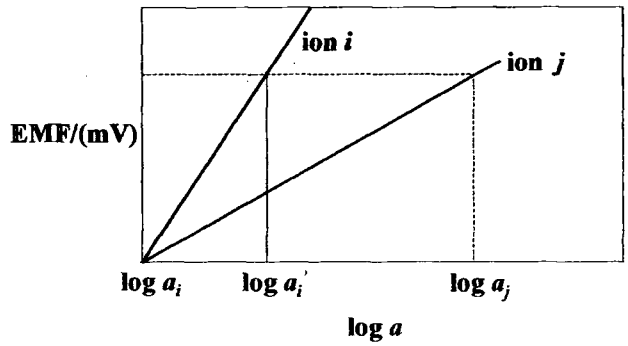

Figure 1.2: The Matched Potential Method (MPM).

As this method is independent of the Nicolskii-Eisenman equation, it treats ions of different valency in a similar manner, and it also does not assume Nernstian slopes for all ions measured. However, as the MPM is not governed by theoretical assumptions, it is difficult to predict results for different analytical situations.

1.1.5 Membrane Components.

The optimum composition for a plasticized PVC membrane based on neutral carrier ionophores is typically:[20] 66% w/w plasticizer, 32% w/w PVC, 1.2% w/w ionophore and 0.8% w/w lipophilic anion (mobile sites).

The importance of PVC is twofold. In addition to the mechanical support of the membrane, it also contains an important source of anionic impurities (fixed sites) that contributes to the cation permselectivity that is exhibited by PVC membranes. Their presence is assumed to arise from various processes i.e. sulfonates and sulfates from polymer initiating groups, carboxylates resulting from oxidation reactions and various surfactants such as phosphates used for emulsion polymerisation.[21]

The plasticizer forms a liquid like state with PVC in which the ionophore and additive can be dissolved. For neutral carrier based PVC membranes, the choice of plasticizer is important as the dielectric constant, ε, of the plasticizer can influence the selectivity coefficient of the membrane.[22] The preference of the membrane for monovalent ions over divalent ions increases as the dielectric constant decreases and vice versa. Another

feature associated with high ε values of the plasticizer is the increased salt co-extraction coefficient. Anionic interference for membranes that are selective towards monovalent cations can be eliminated using plasticizers of low ε , however membranes with o-NPOE tend to exhibit high anionic interference[23] that can lead to increased Donnan failure.[a,24]

Lipophilic ionic additives (mobile sites) such as sodium tetraphenylborate, (NaTPB), or potassium tetrakis(4-chlorophenyl)borate, (KTpClPB), were originally added to PVC membranes to reduce anionic interference from lipophilic anions such as SCN^- and ClO_4^- present in sample solutions. Their presence is also beneficial in that they can reduce the electrical membrane resistance, boost cation sensitivity in cases where the neutral carrier exhibit poor extraction capabilities and they also can have a significant effect on membrane selectivity. The amount of lipophilic anion added should not exceed the molar ratio of ionophore assuming a 1:1 stoichiometry of ionophore-primary ion complex. However, membranes that contain an excess of anion are assumed to be self-correcting i.e. the excess anion leaches from the membrane into the aqueous phase.[25]

In general the ionophore should be sufficiently lipophilic so that it does not leach significantly from the membrane. It should also be selective in complexation of the primary ion. Ionophores that are considered adequate for complex formation with the primary ion posses stability constants in the range of log K = 4 to 9 for a 1:1 stoichiometry.[26] If the binding constant is too small then the ionophore will be predominantly present in the uncomplexed form. However excessively high binding constants may result in non-Nernstian slopes as a result of 'slow' exchange kinetics and co-extraction of anions into the membrane.

1.2 Photoluminescence.

Photoluminescence is used extensively throughout analytical chemistry and is the process in which a material emits light following absorption of light of the same energy

[a]Donnan failure is when the permselectivity of the membrane breaks down, and ions of opposite charge to that of the primary ion *i* enter the membrane and influence the EMF response.

or higher. Photoluminescence can be categorised depending on the spin states of the excited electronic state and the corresponding state to which this decays during the transition. Fundamentally, fluorescence occurs from transitions between two states with the same multiplicity, and phosphorescence between two states with different multiplicity.[27] Transitions involving states of different multiplicity are generally spin forbidden, therefore emission rates of phosphorescence are slow (10^3–10^0 s^{-1}) and lifetimes are typically ms to s. Spin allowed fluorescent transitions have fast emission rates, typically 10^8 s^{-1}.[28] Processes that occur between absorbance and emission of light for a typical organic molecule can be represented by a Jablonski diagram as shown in Figure 1.3.

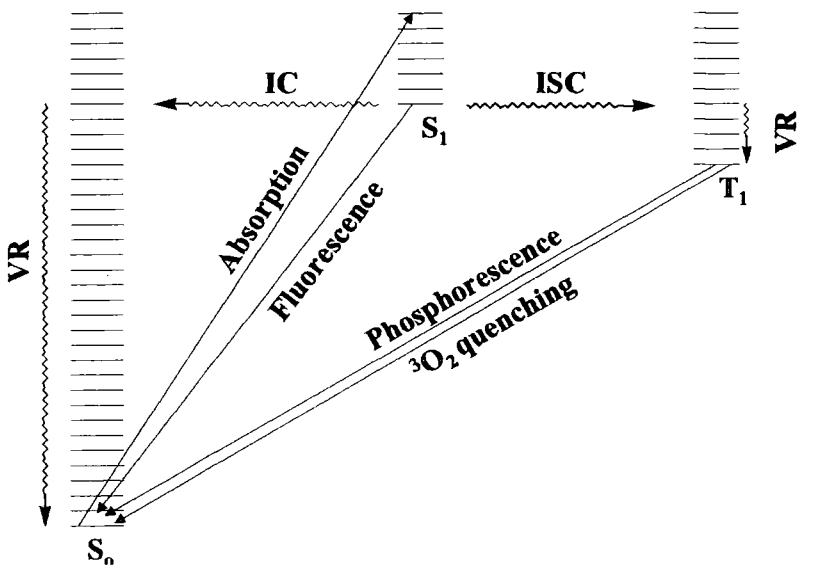

Figure 1.3: Jablonski diagram for a typical organic molecule.

Internal conversion (IC) occurs between isoenergetic electronic states of the same multiplicity i.e. S ↔ S. Inter system crossing (ISC) is the same process involving energy transfer between isoenergetic states with different multiplicities i.e. S ↔ T.

Deactivation from excited states can also occur by inter-molecular energy redistribution between the available electronic and vibrational levels. Vibrational relaxation (VR) is when a state loses its excess energy to the vibrational modes of the surrounding medium. Following ISC, deactivation of the populated T_1 state can also occur by quenching with molecular (T ground state) oxygen. As a result of these non-radiative decay and quenching processes, phosphorescence is rarely observed in aerated solutions at 298 K.

1.2.1 Photophysics of Lanthanide Ions.

There are 14 lanthanide elements going from La^{3+} to Lu^{3+}, in which the 4f orbitals are filled with electrons. These orbitals are shielded by the 5s and 5p shells, which are lower in energy but spatially located outside the 4f subshell. The poor spatial penetration of the 4f electrons results in minimal interactions with the surrounding chemical environment of the lanthanide ion. The electronic transitions within the $5s^2 5p^6 4f^n$ configurations are also marginally affected by the surrounding environment and therefore give rise to characteristic line like absorption and emission spectral bands with low extinction co-efficients in the order of 1 dm^3 mol^{-1} cm^{-1}.[29] Splitting of the energy levels of the $4f^n$ electrons are governed by Coulombic interactions, spin-orbit coupling and ligand field effects within the lanthanide ion. Typical splitting patterns for the Tb^{3+} $[Xe]4f^8 5d^0$ and Eu^{3+} $[Xe]4f^7 5d^0$ configurations are shown in Figure 1.4.

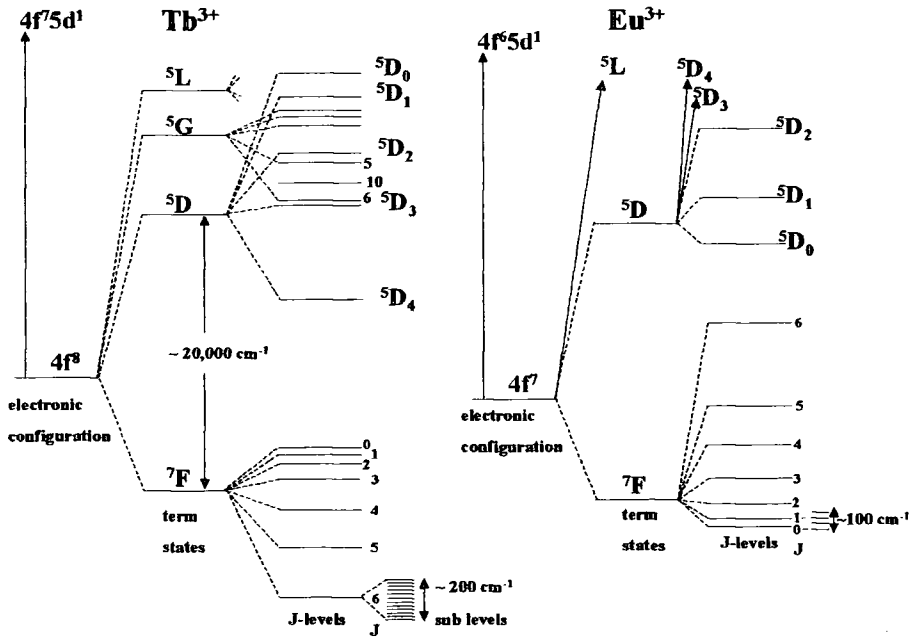

Figure 1.4: Typical splitting patterns for the Tb^{3+} $[Xe]4f^8 5d^0$ and Eu^{3+} $[Xe]4f^7 5d^0$ configurations.

Inter-electronic repulsions dominate and generate the term states, which are in turn split into the J-levels by spin-orbit coupling. These J-levels are described by the term

symbol $^{(2S+1)}L_J$ where 2S+1 represents the total spin multiplicity, L, the total orbital angular momentum and, J, the total angular momentum of the f electrons. Subsequently the degeneracy of the J-levels can be partially or fully removed by the electric field of the surrounding environment following co-ordination.[30] Therefore, crystal field splitting can yield information concerning the co-ordination symmetry of the ion, and appears as fine structure in the respective spectral band depending on the spectral resolution of the instrument.

1.2.2 Sensitised Luminescence.

Populating the excited states of the lanthanide ions directly using conventional light sources is weakened by their distinctive low molar extinction co-efficients that result from parity forbidden f $\rightarrow$ f transitions. To overcome this problem indirect excitation by sensitised emission is commonly adopted. Sensitised emission enhances the effective molar extinction co-efficient by incorporating an organic chromophore into the coordinating ion ligand. This serves as an antenna to absorb the incident radiation and transfer this energy to the lanthanide ion.[31] The general process of sensitised emission in luminescent lanthanide complexes is described in Figure 1.5.

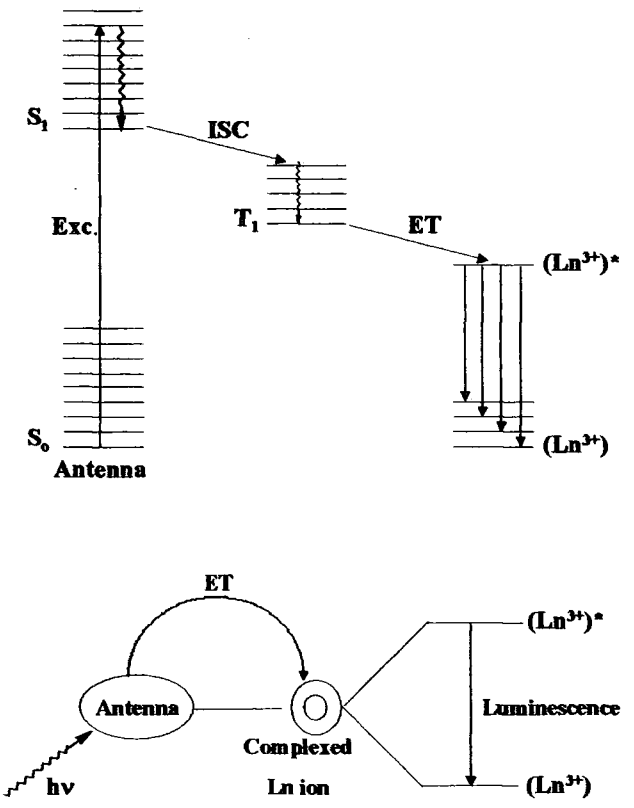

Figure 1.5: Sensitised emission.

Excitation of the chromophore into its allowed singlet–singlet transition is followed by ISC to yield the T_1 state of the chromophore. ISC competes with other processes that can occur from the singlet state of the antenna that are shown in Figure 1.3. In the case of Eu^{3+} ion, which has a reduction potential, of (E_{red} = -0.35 V vs. NHE,[32] for the free aqua ion and is typically –1.0 V vs. NHE[33] in octadentate polyamino-carboxylate/amide complexes), competitive deactivation by photoinduced electron transfer from the proximate S_1 excited state of the antenna may occur.[34] This ligand to metal charge transfer (LMCT) state decays non-radiatively and reduces the energy transfer process to the ion. For energy transfer to occur to the lanthanide ion, the antenna must be in close proximity. In order for energy transfer to occur, the T_1 state must be higher in energy, by at least 1700 cm^{-1}, than the emissive state of the lanthanide. If this gap is less than 1500 cm^{-1}, then the competitive process of thermally activated back-energy transfer can repopulate the T_1 state. Conversely, if the gap is too great then energy transfer is inefficient. To avoid unwanted excitation of biomolecules, the antenna needs to be

excited at wavelengths in excess of 350 nm (~ 28 600 cm^{-1}). In the cases of Eu^{3+} and Tb^{3+} their emissive $^5D_0$ and $^5D_4$ states have energies of 17 200 and 20 400 cm^{-1} respectively, hence the chosen antenna must exhibit a low singlet excited state energy and a small S_1–T_1 energy gap.[33]

Quenching of the emissive states of the lanthanide ions can occur through energy transfer to high energy vibrations of solvent molecules or oscillators of the complexing ligand. Water molecules that are bound directly to the ion are excellent quenchers of lanthanide luminescence. This is due to efficient Franck-Condon overlap of the emissive states of the lanthanides and the overtones of the oscillators ($^5D_0$ of Eu^{3+} with 3rd vibrational overtone of O-H, $^5D_4$ of Tb^{3+} with 4th vibrational overtone of O-H).[35]

1.3 Sol-Gel Technology.

Optical signalling of analyte recognition by selective receptors has provided many opportunities for the development of optical chemical sensors.[36,37] Sol-gel encapsulation offers an attractive feature from an analytical viewpoint. It is a convenient means of immobilisation of chemical species in a matrix that is permeable to analytes and compatible for optical transduction of the recognition process.

In simplistic terms, sol-gel technology enables the production of porous glasses through the polymerisation of inorganic alkoxide precursors at room temperature. Discovered in the 19th century, the process has been extensively studied and reported by Brinkler and Scherer,[38] and is now one of the fastest growing fields of material chemistry.[39] Sol-gels are an ideal matrix for optical sensors as the process allows ease of fabrication of sensor design, tunable pore size, low temperature encapsulation of sensing species, optical transparency, chemical inertness in most cases of extreme sampling conditions and good mechanical stability.

Sol-gel processing also allows flexibility and ease in terms of shaping sensor configurations in that a sol-gel can be spun or sprayed onto flat surfaces and dip-coated onto optical fibres. Spin-coating involves the deposition of sol-gel onto a spinning

substrate to produce thin films of uniform thickness in most cases, where film thickness can be controlled through modulation of both time and speed of spinning.[40]

The first report of a fibre-optic sol-gel based sensor was in 1991 by MacCraith,[41] whose research is in the forefront of applying sol-gel technology to the development of optical chemical sensors. In 1997 he was granted a generic European patent for sol-gel waveguide sensors.[42]

1.3.1 Sol-Gel Chemistry.

The most common precursors used for synthesising sol-gel glasses for optical sensing purposes are tetramethoxysilane (TMOS) and tetraethoxysilane (TEOS). These reagents can be hydrolysed and condensed under mild conditions to produce glasses with a pronounced hydrophilic surface, which makes them ideal for sensing aqueous ions such as the hydronium ion. In a typical sol-gel process the alkoxide precursor is subjected to a series of hydrolysis and condensation reactions to give a colloidal suspension known as a sol, to which sensing species can be added for entrapment. Other requirements for the process include water that has been acidified or basified with mineral acids and bases such as hydrochloric acid or ammonia, and a cosolvent such as methanol, as water is immiscible with the silica alkoxide. The simplified reaction sequence for sol-gel processing is shown in Figure 1.6.

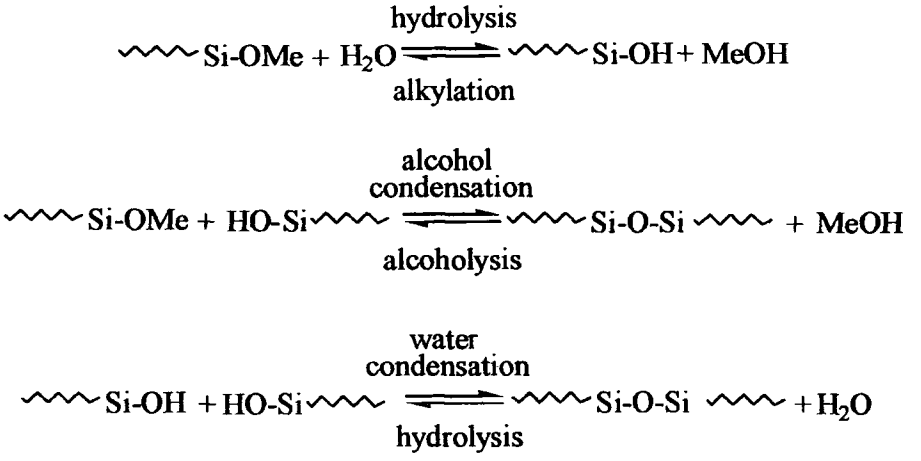

Figure 1.6: Reaction sequence for sol-gel processing.

In the first step hydrolysis generates a silanol group by replacing an alkoxide group with a hydroxyl group. These silanol moieties undergo condensation involving either another silanol group or alkoxide group that results in the formation of siloxane linkages and by products such as water and alcohol, which are generated in situ. As the number of siloxane bridges increases, the moieties jointly aggregate in the sol to form a gel network, trapping the volatiles and doped complexes within the silica cage network.

A number of variables can influence the hydrolysis and condensation reactions of the sol-gel process. Factors that predominantly affect the sol-gel network are type and amount of catalyst, i.e. pH of solution, water to alkoxide ratio and introduction of network modifiers. Other factors such as solvent effects, additives, ageing, drying and temperature can also contribute to the tailoring of the sol-gel network.[38]

1.3.2 Catalyst.

As this thesis is concerned with sol-gel processing using acid catalysis, discussions will focus on acid hydrolysis and condensation only. The pH of the starting solution is an important factor in the preparation of a sol-gel film. HCl or ammonia are the most common types of catalyst used in sol-gel processing, although others such as acetic acid, amines and HF have been used.[43]

Controlling hydrolysis and condensation rates allows the tailoring of the pore size of the silica network. The isoelectric point of silica occurs approximately at pH 2, and changes slightly depending on the degree of substitution on the Si atom. Acid catalysis is classed as occurring at $pH < 2$, where the surface charge becomes positive, hydrolysis rates are high and the rate of condensation is at a distinct minimum.[44]

The generally accepted mechanism for acid catalysed hydrolysis involves nucleophilic substitution followed by inversion of the reaction species. In a rapid first step protonation of the alkoxide group reduces the silica atom's electron density, making it more susceptible to attack from water.

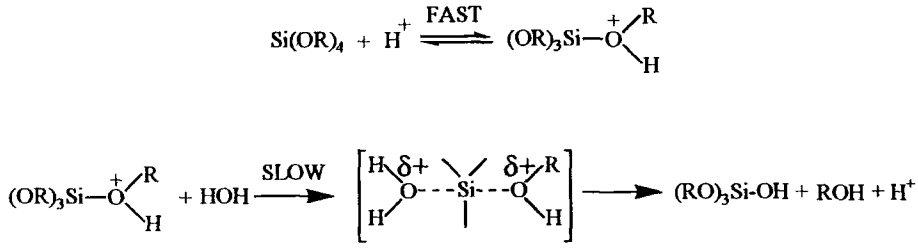

Figure 1.7: Hydrolysis mechanism.

Steric effects can influence the rate of hydrolysis as can inductive effects of side groups, but to a lesser extent. The rate of hydrolysis tends to be increased by substituents that reduce steric crowding and to a lesser extent stabilize the developing positive charges of the transition state (alkyl). The rate of hydrolysis decreases with each hydrolysis step as hydroxyl substituents withdraw electron density inductively.[38]

Condensation rates for acid catalysis tend to be slow and result in prolonged gelation times. Again the mechanism is believed to proceed via protonation of the silanol species making the Si atom more susceptible to nucleophilic attack.

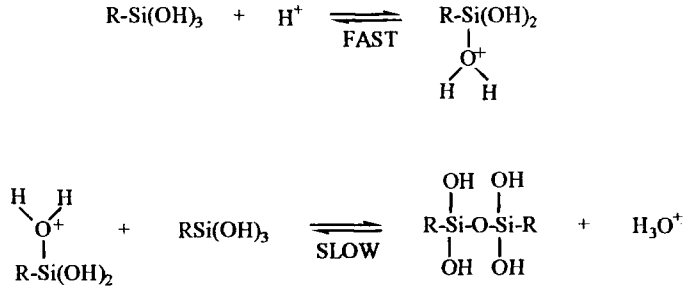

Figure 1.8: Condensation mechanism.

The rate of condensation is influenced by steric and inductive effects of the substituents attached to the Si atom. Electron withdrawing groups such as OH or OSi increase silanol acidity, destabilise the degree of positive charge in the transition state or the intermediate and reduce the condensation rate. The minimum condensation rate occurs at pH 2 where the groups are most acidic. Prepared under acidic conditions, condensation is thought to be favoured between the least acidic silanol groups found on the end of monomers or chains, and those with pronounced acidity located on branched

chains. End groups tend to be more readily hydrolysed than middle groups and the slight repulsion due to positive charges means the probability of condensation reactions depends on the interparticle collisions. The resulting sol-gels tend to be characterised by linear polymers that are weakly branched and exhibit microporous networks with nanometer pore sizes capable of encapsulating small sensing complexes.[45] Structural features within the sol-gels prepared using acid catalysis tend to be too small to scatter light. Therefore these sol-gels are generally transparent,[46] and can be used for optical sensing.

Although sol-gels prepared using acidic catalysis make ideal optical sensing matrices, many organic compounds cannot withstand the harsh pH environment required to ensure small pore size and entrapment of the sensing complex. The choice of acid catalyst can also bear some effect on the optical stability of sol-gel films. Sensing matrices prepared using HCl as the catalyst have shown susceptibility towards photodegradation compared to similar films prepared with other acid catalysis.[47]

1.3.3 Water Content.

The effect of the water content of the sol-gel preparation is such that for any given pH, increasing the molar ratio of water/silica, R, increases the rate of hydrolysis and condensation and the siloxane content of the gel. This results in a slighter denser structure with an enhanced degree of crosslinking. For most reaction conditions, condensation will begin before hydrolysis is complete. Because water is generated in situ during condensation and according to Equation 1.22, an R-value of 2 is theoretically adequate to ensure complete hydrolysis and generate anhydrous silica.

$$nSi(OR)_4 + 2_nH_2O \rightarrow nSiO_2 + 4nROH \qquad \textbf{Equ 1.22}$$

The fact that water is generated during the process makes the calculation of the optimum water content difficult. Even when an excess of water (R>2) is used with alkyl orthosilicates, reactions tend not to go to completion and instead result in a range of intermediates that can be described using the following formula $[SiO_x(OH)_y(OR)_2]_n$, where $2x+y+z = 4$.[38] Commonly used in literature preparations for sol-gel sensing

films, an R-value of 4 generates networks with smaller pore sizes, shorter gelation times and in some cases reduced leaching effects compared to R = 2 films. The latter can be related to a larger pore size in relation to the doped sensing complex, compared to R = 4 pore size.[44]

1.3.4 Organically Modified Sol-Gels.

Glasses with a pronounced hydrophobicity and reduced silanol content can be produced using organoalkoxysilanes. These precursors include methyltriethoxysilane (MTEOS) and ethyltriethoxysilane (ETEOS) and have the general structure $[R'_nSi(OR)_{4-n}]$. Incorporation of these organic moieties modifies the polarity and mechanical properties of the sol-gel structures. Organically modified silicate films prepared from these precursors, have been used for gas phase sensing of oxygen[42] and carbon dioxide.[48]

1.4 Optical pH Sensing.

1.4.1 Applications and Principles of Optical pH Sensors.

From an analytical viewpoint, the concentration of hydrogen ions is always described in terms of pH, where the p donates the 'negative logarithm of'.[49] The development of optical chemical sensors to sense pH has received significant attention due to the importance of pH measurement in numerous practical applications where conventional pH glass electrodes are considered unsuitable. Such areas include environmental, clinical and industrial where optical sensing would be most advantageous due to the feasibility of miniaturisation, associated with exciting possibilities for remote sensing and *in situ* measurement. Other reasons cited for the development of optical pH sensors include the lack of requirement of a reference sensor, resistance from electrical interference and improvements in electrical safety concerning clinical applications.[37,49,50]

The main application for optical pH sensors lies in the biomedical field where a narrow pH range exists. The clinical window covers the range between pH 5-8, with physiological pH operating between pH 6.9–7.5. For example the growth of tumour cells is often accompanied by variation in local pH; cells exhibit intra- and extra cellular

pH values of 7.2 and 7.4, and 7.4 and 6.9 for healthy and tumour cells respectively.[51] Hence signalling a change in the acidity in the human body may be an important feature of cancer diagnosis.

The continuous *in vivo* monitoring of blood pH in critically ill patients has not only directed research concerning the development of optical transduction of pH but also that of developing clinical microelectrochemical pH sensors. At present there exist no ideal methods to monitor neurological pH changes associated with brain injury or stroke.[52] Following ischaemia to the brain, studies have shown brain pH to decrease from pH 7.4 to 6.75. Continuous monitoring of brain pH would certainly benefit the treatment of comatose and stroke patients and outlines again the advantage of optical sensors over electrochemical means, in that fibre optics allow the transmission of light signals over significant distances and hence are ideal for sensing *in vivo*. They are also unaffected by electromagnetic interference and are compatible with magnetic resonance imaging.[53]

The accepted method of determining pH is by electrochemical measurement using a combined glass electrode. As changes in pH can indicate disease or trauma and also because it has an important role in monitoring many processes such as controlling the activity of enzymes,[54] the accurate measurement of pH is important.

Neither optical nor electrochemical methods allow the precise measurement of pH as thermodynamic compromises have to be reached that differ for each application. Although a good glass electrode will respond to the activity of the hydronium ion, electrochemical measurement can in practice only provide thermodynamically correct values concerning the activity of the whole electrolyte, as undefined errors due to the liquid junction potential (LJP) contaminate the value of single ion activities. Modern glass electrodes are designed to minimise the LJP, and it is assumed that the LJP can be removed through calibration, however under certain conditions, i.e. pH measurement in alcoholic media or mixed solvents, this assumption itself can be detrimental to the practical determination of pH.

Optical pH sensors measure the pH dependent variation of intrinsic optical properties of sensing species and in turn have limitations not encountered with electrochemical

measurement. The fundamental difference between electrochemical and optical methods is that the former shows a linear dependence on the activity of H^+, where measurements concerning the latter are related to the relative concentrations of the acid and base forms of the sensing species, where the degree of dissociation is dependent on the concentration of H^+.[50] The derivation of this relationship from the mass action law is given in appendix I.

Conversely, optical pH measurement based on the use of pH indicators is limited to a narrow pH range. Where the mass action law is strictly obeyed, a linear range is observed over the range covered by $pK_a \pm 0.5$ pH units. Beyond values typical of the pK_a value $\pm$ 1 the change in optical signal becomes increasingly smaller, introducing large errors in pH measurement. Therefore the two major limitations of optical sensors are their intrinsic narrow dynamic range and semi non-linear response. However even though a broad linear response is attractive as it simplifies calibration and facilitates sensitivity and precision measurements, as stated previously the physiological pH range is intrinsically narrow.

Parameters that can influence immobilised pK_a values include indicator concentration and solvent effects. Like the hydronium ion activity, pKa values are affected by the ionic strength of the surrounding medium. Following entrapment in ionic sensing matrices, deviations from the theoretical response, such as shifts in pK_a and broadening of the linear range, can occur due to a spectrum of electronic microenvironments experienced by the molecule. Generally, apparent pK_a values can be related to thermodynamic values according to the Davies equation.[55]

$$pK_{app} = pK_a + A\left(z_{HA}^2 + z_{A^-}^2\right)\left[\frac{\sqrt{\mu}}{1+\sqrt{\mu}} - 0.2\mu\right] \qquad \textbf{Equ 1.23}$$

μ ionic strength.

z charge.

A temperature coefficient.

Where the mass action law is strictly obeyed, a 90% signal change occurs over 2.54 pH units. However in the case of immobilised indicators, where deviations are normality, the pH range over which a 90% signal change occurs can be as great as 6.64 pH units,[56] and should be specified.

1.4.2 pH Sensitive Ru(II) Complexes.

Luminescent pH sensing is attractive as it is compatible with miniaturization where only low concentrations of sensing species are required to maintain good sensitivity.
Luminescent pH responsive Ru(II) complexes $[Ru(bpy)_2(dhphen)]^{2+}$ **1**[57] (bpy = 2,2'-bipyridine, dhphen = 4,7-dihydroxy-1,10-phenanthroline) and $[Ru(phen)_2[(phen)(OH)_2]]^{2+}$ **2**[58] or $[Ru(Ph_2phen)_2[(phen)(OH)_2]]^{2+}$ **3** (phen = 1,10-phenanthroline, Ph_2phen = 4,7-diphenyl-1,10-phenanthroline and $phen(OH)_2$ = 4,7-dihydroxy-1,10-phenanthroline) have been immobilised in Nafion and D4TMI-PEG-Jeffamine ($(SiRCH_3O)_4$ units with poly(ethyleneoxide) cross-linkers), polymer networks respectively. pH dependent changes in emission were observed over 1-8 pH units for the former, and 1-6 and 2-8 pH units for the latter cases. Relatively slow response times of several minutes were displayed in all films.

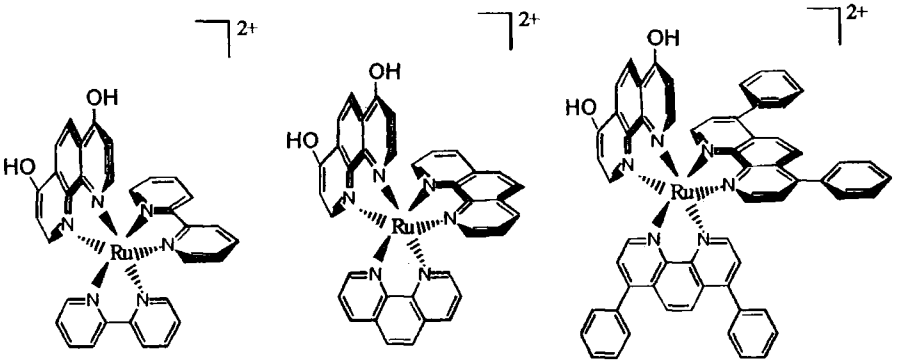

1 **2** **3**

Figure 1.9: Structures of luminescent pH responsive Ru(II) complexes **1-3.**

1.4.3 Probes for Extreme pH measurement and Single Molecule pH Sensing.

Recent solution studies of pH responsive species include the complex 1,9-dihydro-3-phenyl-4H-pyrazolo[3,4-*b*]quinoline-4-one **4**,[59] for extreme pH measurement and a SNARF-1 (10-amino-3-hydroxy-spiro[7H-benzo[c]xanthene-7,1'(3'H)-isobenzofuran]-3'-one)–dextran conjugate[60] for single molecule pH sensing. The former probe can measure over 2 pH ranges (1.8-3.4 and 11.6-13.3) as it was designed to include several H^+ receptors. Complexation of SNARF-1 **5** to the polysaccharide (0.6 dye per dextran) increased the dye's intracellular retention. The ratio between the fluorescent intensities at 580 nm and 640 nm was monitored as a function of pH in agarose gel media. For single molecule detection the concentration of conjugate used was in the order of 10^{-10}–10^{-9} mol dm^{-3}, and the pore size of the gels were adequate enough to prevent inter-pore diffusion yet retain rotational motion.

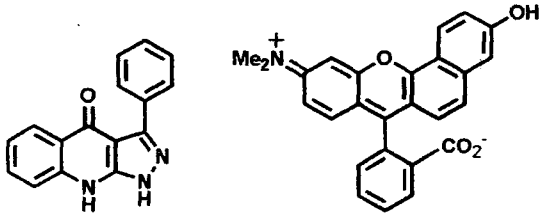

4 **5**

Figure 1.10: Structure of 1,9-dihydro-3-phenyl-4H-pyrazolo[3,4-*b*]quinoline-4-one **4**, and SNARF-1 **5**.

1.4.4 Sol-Gel Immobilised pH Sensors.

The effect of pH modulation on the transfer of energy between a pH insensitive phosphorescent donor to a mixture of pH sensitive dyes has recently been described as the first room temperature phosphorescent (RTP) optical sensor for pH.[61] Following immobilisation in a TMOS sol-gel, 6-bromo-2-naphthyl sulfonate (BNS) **6** and α-bromonaphthalene (BrN) **7** acted as donor molecules. A mixture of phenol red **8**, bromocresol purple **9** and bromophenol blue **10** were used as the acceptors as their absorbance spectra overlapped the emission spectra of the donors between 3.5-8 pH units. Both donors were capable of producing RTP emission in aqueous oxygenated media following sol-gel entrapment.

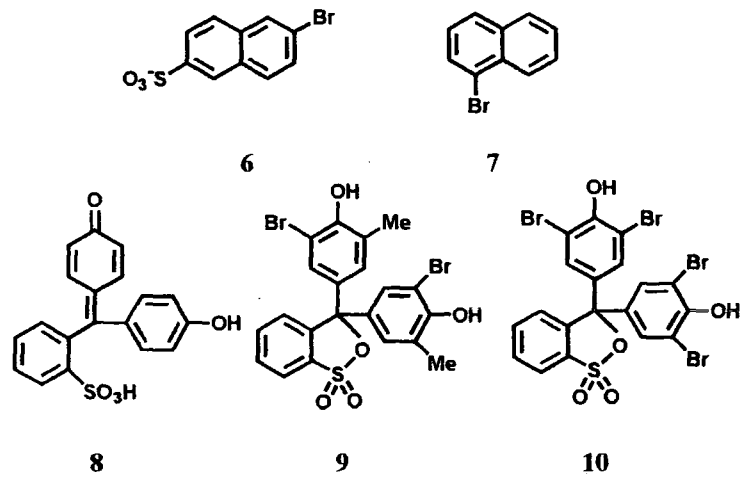

8 9 10

Figure 1.11: Structures of 6-bromo-2-naphthyl sulfonate (BNS) **6**, α-bromonaphthalene (BrN) **7**, phenol red **8**, bromocresol purple **9** and bromophenol blue **10**.

Monitoring the changes in luminescent intensity based signals, can often be inconvenient or unreliable due to limitations in stability and reproducibility of the sensing material, as a direct result of changes in the local probe concentration due to bleaching effects and leaching from encapsulating matrices. Following the covalent attachment of the pH sensitive species, aminofluorescein **11**, to sol-gel media, no apparent leaching of the complex was observed after a period of 20 hours. However, where immobilisation of **11** was due to physical encapsulation (doping) within a silica network, leaching of the complex was observed over a period of 6 months. The sensitivity of the covalently bound sensing species was reduced by 75 %, and its response time doubled, when compared to observations where immobilisation was due to doping.[56] An attractive alternative to intensity-based sensing is to use ratio-metric sensing or to monitor the lifetime decay of the sensing species. Both offer alternative means that are independent of fluctuations in the concentration of the sensing probes.

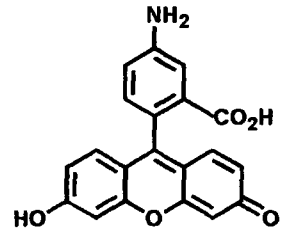

11

Figure 1.12: Structure of aminofluorescein **11**.

Luminescent lifetime optical pH sensors based on energy transfer from luminescent donor Ru(II) complexes to non-fluorescing pH acceptor indicator complexes have been studied in solution[62] and in a sol-gel matrix.[63] A sol-gel pH sensor based on phase fluorometric lifetime measurements has also been reported.[64] Following an increase in pH, the enhancement in the absorbance of the acceptor complex, bromothymol blue **12**, facilitated the energy transfer from the donor complex, Texas red hydrazine **13**, which was excited at 442 nm. Consequently this reduced the fluorescent lifetime of the donor. The working range of this sensor was between pH 6.8–7.8, and the total phase change was 7°. Resolution to less than 0.1 pH unit was also achieved.

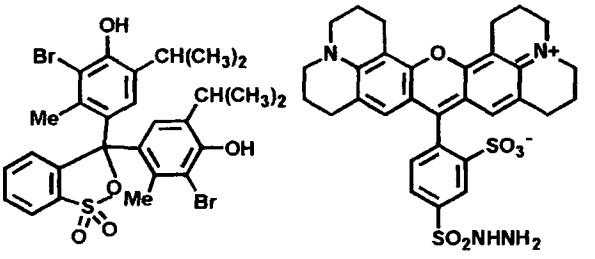

12 **13**

Figure 1.13: Structures of bromothymol blue **12**, and Texas red hydrazine **13**.

Many of the reports of sol-gel optical sensors are concerned with the measurement of pH due to the rapid diffusion of H^+ in sol-gel and also because of the vast number of pH response compounds available and suitable for optical transduction. pH sol-gel sensors incorporating a series of Ru(II) polypyridyls have been prepared by *Malins et al.*[65] Acid catalysis of TEOS immobilised the sensing species and enhanced the pH operating range of the species; a direct consequence of the microheterogeneity of the matrix, when compared to solution behaviour. Linear responses were observed over the pH range 3-9 for the $[Ru(phen(SO_3)_2)_3]$[66] **14** complex and increased signal stability and sensitivity over the range pH 3-8 was displayed by the $[Ru(bpy)_2(pt\text{-}OH)]$ **15** complex. The former was found to exhibit cross sensitivity to oxygen quenching while the latter showed minimal oxygen sensitivity and could detect pH changes of 0.05 pH units.

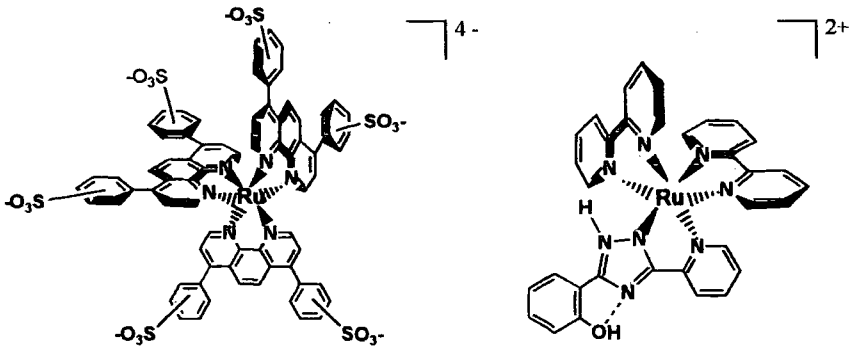

14 **15**

Figure 1.14: Structure of $[Ru(phen(SO_3)_2)_3]$ **14** and $[Ru(bpy)_2(pt\text{-}OH)]$ **15**.

Another recent sol-gel luminescent pH sensor has focused on the encapsulation of SNARF-1C **16** (seminaphthorhodamine-1 carboxylate). Following dip-coating onto optical fibres, the sensing layers were able to perform *in vitro* measurements in phosphate buffered saline and human whole blood.[53] In both cases a linear response was obtained and in the latter case, a fast (15 s) linear response in the clinically relevant range from pH 6.8-8 was observed. Subsequently *in vivo* measurements have been performed in the brain of a Sprague-Dawley rat.[52] The pH of the brain was modulated following the injection of sodium bicarbonate into the peritoneal cavity. pH changes of the rat's brain were also measured during the inducement of a stroke. Simultaneous measurements were performed using electrochemical sensors for comparison purposes.

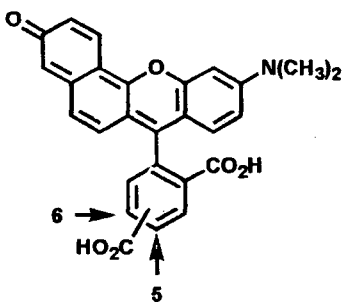

16

Figure 1.15: Structure of (seminaphthorhodamine-1 carboxylate) SNARF-1C **16**.

1.4.5 Lanthanides as pH Sensing Probes.

Despite the attractive optical characteristics of lanthanide complexes such as millisecond lifetime, spiked emission and large Stokes shifts, there is a conspicuous absence in the literature of their use as optical transducers for pH sensors. *Parker et al* have generated some interesting terbium and europium complexes incorporating cyclen (12-N_4) derivatives systems and a pH responsive phenanthridine antenna.[33] Alternative lanthanide systems for pH measurement focused on the pH dependent on/off ligation of a para-substituted sulfonamide pendant group and the associated switching of the hydration state of the lanthanide metal centre.[67]

The pH indicator BTB has been the obvious choice for the fabrication of systems where luminescence from pH inert Eu^{3+} complexes is quenched by energy transfer to acceptors, whose absorbing properties are pH sensitive. Such systems have been described based on the metal lifetime measurements of [2,2',2'',2'''-[4'-phenyl-2,2':6',2''-terpyridine-6,6''-diyl)-bis(methylenenitrilo)]tetrakis(acetato)]europium(III) **17** in aqueous solution[68] or intensity based changes of a Eu^{3+} complex **18** following immobilisation in a sol-gel film.[69] This is not surprising considering the absorbance maximum wavelength of BTB coincides with the hypersensitive $\Delta J = 2$ transition of europium, therefore ensuring good acceptor donor spectral overlap, which is required for long-range energy transfer. Structure **18** is shown as claimed in the literature. It is however implausible and involves octadentate binding to the ligand with one solvent molecule completing the europium coordination shell.

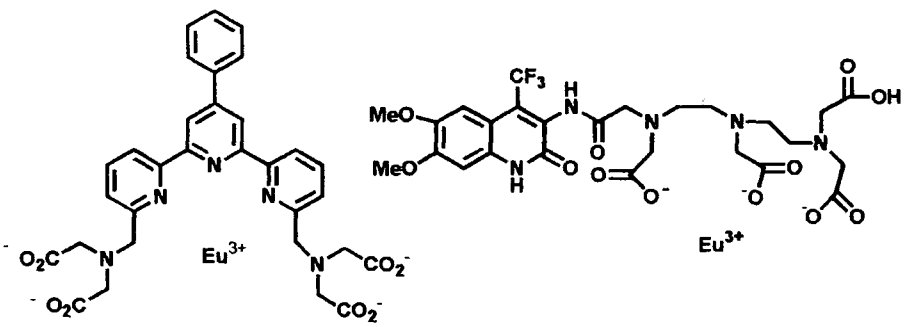

17 **18**

Figure 1.16: Structures of Eu^{3+} complexes **17** and **18**.

In the absence of BTB changes, the single exponential decay lifetime of the Eu^{3+}-terpy complex were pH insensitive. In the presence of 8 μmol dm^{-3} BTB indicator pH dependent changes in the lifetime of the Eu^{3+} complex were observed (τ = 244 μs at pH = 6.95, τ = 591 μs at pH 6.15 and τ = 936 μs at pH 5.47). This could be attributed to the strong and weak quenching capabilities of the blue basic and yellow acidic forms of the dye.

Following immobilisation of a Eu^{3+} complex incorporating an antenna function based on a 4-trifluoromethylcarbostyril derivative, the complex showed no signs of pH sensitive changes in the metal based emission that was apparent in solution studies following excitation at 370 nm. Following co-immobilisation of the Eu^{3+} complex and BTB in a sol-gel matrix, a 75% overall change in signal intensity was observed on going from pH 5.13-10.77. Response times observed for a 95% change in signal were approximately 100 s. The apparent pK_a of BTB in the sol-gel matrix was 7.29, which was 0.5 pH units greater than its value in homogeneous solution.

Luminescent Tb^{3+} complexes incorporating terpyridyl derivatives **19-20** as chromophores have been reported by *deSilva et al.*[70] These complexes function as lumiphore-spacer-receptor systems. **19-20** serve as sensitising antenna and include amino group functionality that act as H^+ receptors and electron donors in the H^+-induced suppression of Photoinduced Electron Transfer (PET) to the lanthanide ion. pH dependent metal-based luminescent enhancement factors of 16 and 10, and pK_a values of 6.8 and 4.9 were observed for the respective complexes, when measuring the delayed luminescence spectra. No H^+-induced shift in wavelength or spectral form was observed during the pH titration.

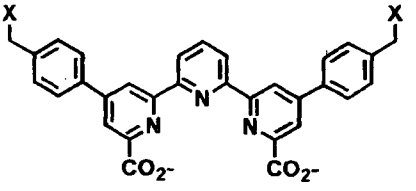

19 $X = NEt_2$

20 $X = N[(CH_2)_2]_2O$

Figure 1.17: Structures of terpyridyl derivatives **19-20.**

1.5 Dissolved Oxygen Sensing.

Anoxia and hypoxia are conditions that occur in an organ when there is a diminished supply of oxygen to the organ's tissue. Anoxia results when there is an absence of oxygen supply to the tissue, and hypoxia occurs when the oxygen supply to the tissue decreases despite there being an adequate blood supply to the organ in both cases. A number of events can lead to both conditions such as a heart attack, severe asthma, carbon monoxide inhalation and poisoning.[71] Therefore the ability to measure and monitor the dissolved oxygen (DO) level is important in environmental, industrial and clinical applications.

To ensure a flourishing aquatic habitat, it is important to monitor the DO level. The concentration of DO in sea and river water is not static but subsists as a dynamic equilibrium that is maintained by biochemical depletion and re-oxygenation. The introduction of pollution can disturb aquatic environments and diminish the concentration of DO to levels that are detrimental to most species of fish. Hypoxia, which can alter the behaviour of fish can occur when the concentration of DO < 3 ppm. In severe cases of pollution anoxic events ([DO] < 1 ppm) often cause mortality.[47]

The biochemical breakdown of sewage is achieved by bacteria working in aerobic conditions. Therefore, DO monitoring is important in waste treatment plants where an inadequate air supply can enhance the activity of anaerobic sulfate reducing bacteria, that produce the highly corrosive gas hydrogen sulfide. In contrast, as aeration is the main operating expense, oxygen levels that exceed the optimum concentration required are considered wasteful. Thus the monitoring of the oxygen supply in waste management is of economical importance.

Although the measurement of intracellular oxygen is not yet feasible using current sensing technology, the clinical assessment of DO levels in patients is important, as oxygen is evolved in many biochemical processes such as the production of energy used to synthesise ATP from the phosphorylation of ADP. In the body, oxygen is transported to the cells and tissues by blood and therefore to be able to monitor the local DO levels *in vivo* is the greatest challenge in designing oxygen sensors.

1.5.1 Current Techniques Used for Dissolved Oxygen Sensing.

The initial determination of DO was performed by titration using Winkler's Reagent. Following the addition of manganous sulphate to the reagent (NaOH and NaI), a white precipitate of manganous hydroxide is generated which is oxidised by oxygen in the sample to the brown manganic oxide-hydroxide. After acidification, Mn^{4+} reacts with iodide and liberates two molecules of iodine per molecule of oxygen consumed in the sample. The concentration of liberated iodine is then determined by titration against thiosulphate.[72]

For the past 50 years or so, quantitative DO determination has been achieved electrochemically using sensors based on the amperometric Clark electrode or the galvanic cell designed by Mackereth.[72] Both cells measure the rate of oxygen diffusion to the electrode. At the cathode the oxygen is reduced and converted into hydroxyl ions. Oxygen electrodes based on the Clark system consist of a chamber which contains an electrolyte such as KCl and two electrodes, one being a silver anode and the other either a platinum or gold cathode that is embedded in the end of a support rod. The tip of the cathode is covered with an oxygen permeable membrane such as polyethylene or Teflon. Following polarization of the two electrodes using an external polarizing potential, an electric current flows between the anode and cathode. Sensors based on the galvanic cell consist of a Ag cathode and Pb anode, which have different electrode potentials that produce a voltage that drives the current through the cell. Providing the temperature is maintained relatively constant, the current has a linear relationship with the concentration of DO.

Provided they are used correctly, electrochemical oxygen sensors can provide reliable and reproducible measurements. However their application to the determination of DO levels in blood is time consuming. Clinical measurement assessing the oxygen status of a patient is usually performed using a blood gas analyser that uses electrodes as the sensing device.[54] However, first the patient's blood has to be removed and transported to the laboratory for analysis. During this period, the patient's oxygen status may alter. Electrochemical sensors can also suffer from electrical interference and possess possible safety implications for medical application.

Optical oxygen sensors are easy to miniaturise and because they can be coupled to the distal end of optical fibres or wave-guides that can transmit light over long distances, they are attractive for remote sensing and *in vivo* applications. The optical detection of DO levels especially in the blood is considered a superior technique and is one of the greatest challenges in the sensing biomedical field.

1.5.2 Organic Dyes for Oxygen Sensing.

Oxygen quenching of excited states has been recognised as an important method for oxygen sensing. In the past two decades there has been a growing interest in optical sensing materials for oxygen detection. The majority of these sensing materials incorporate a dye whose luminescence is reversibly quenched by molecular oxygen. Early examples encapsulate organic dyes as the sensing species such as polycyclic aromatic hydrocarbons (perylene derivatives,[73] quinoline, pyrene and derivatives and phenanthrene),[74] in oxygen permeable polymers such as silicon rubber and polystyrene. Phosphorescence quenching of the dye α-diketone camphorquinone **21** following immobilisation in PVC produced a sensing film that could quantitatively determine oxygen in a gas stream in the range of 0.1 to 25% at room temperature. Properties of this dye include a relatively large Stokes shift (190 nm), and absorbance and emission in the visible range of the spectrum. Interestingly, Stern-Volmer plots based on phosphorescence intensity and lifetime data for oxygen quenching were linear following the immobilisation of **21** in PVC, yet displayed downward curvature at low oxygen concentrations, following encapsulation in a silica gel. This response was attributed to multisite quenching behaviour, where **21** was assumed to occupy different environments within the silica matrix, which have different accessibility to O_2.[75]

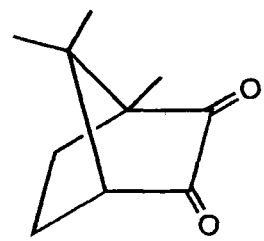

21

Figure 1.18: Structure of α-diketone camphorquinone **21**.

1.5.3 Luminescent Transition Metal Complexes for Oxygen Sensing.

An important class of optical materials for oxygen sensing are the luminescent complexes of the transition metals Ru, Re and Os.[76] Their optical properties include lifetimes that range from hundreds of nanoseconds to tens of microseconds. Their luminescent quantum yields are adequate for optical sensing (typical of 0.04 to 0.2, but can exceed 0.5). With intense visible absorbance and quantum yields that are independent of excitation wavelengths, sensitivity is enhanced as is the scope of excitation sources, therefore simplifying sensor design all round.

Luminescent Ru(II) diimine complexes have dominated the field of fluorescent oxygen sensors.[77,78,79,80,81] These complexes have shown exceptional potential for development into commercial oxygen sensors, mainly because they display long lifetimes (0.1-7μs), are easily excited and have high quantum yields.[82] Following encapsulation of tris(4,7-diphenyl-1,10-phenanthroline)-Ru(II) complex $[Ru(Ph_2phen)_3]^{2+}$ **22** in sol gel,[79] the sensing material displayed high sensitivity (I_o/I_{100}>26), to oxygen sensing in the gas phase. However one downfall of the Ru(II) complexes is they suffer the disadvantage of requiring excitation in the blue region of the spectrum near 450 nm.[83]

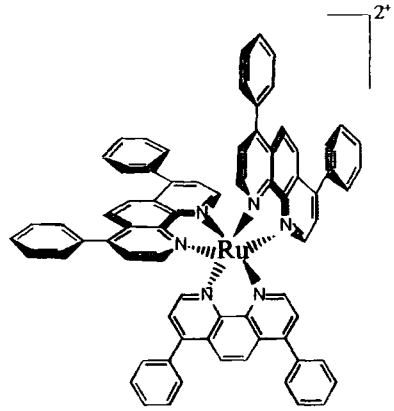

22

Figure 1.19: Structure of tris(4,7-diphenyl-1,10-phenanthroline)-Ru(II) complex $[Ru(Ph_2phen)_3]^{2+}$ **22**.

Human skin absorbs yellow (580 nm) and blue light. Red light of 600nm can penetrate slightly. Beyond 600nm the skin is relatively translucent to red light.[84] Os(II) complexes analogous to the Ru(II) complexes can be excited by red diode lasers at 635 nm, 650 nm and 670 nm,[83] as they have large molar extinction coefficients (1000's) in

the 600 to 670 nm region. They also emit into the near IR (700 to 720 nm) and exhibit oxygen quenching behaviour that is independent of excitation wavelengths corresponding to the diode lasers. Another advantage the Os(II) have over the Ru(II) species is their complexes are more photostable due to the larger energy gap between the emissive level and photolabile upper dd states. However due to the heavy atom effect their radiative rate constants are approximately equal or higher compared to those of the Ru(II) series. As a direct result, they have inherently shorter lifetimes (several 100 ns in deoxygenated solution) and lower quantum yields. Hence although the Os(II) transition metal complexes are not as sensitive to oxygen quenching as the Ru(II) complexes, they still have potential as optical oxygen sensors. An example of a red absorbing optical sensor for transcutaneous oxygen sensing *in vivo* that is not coupled to an optical fibre has been described by *Bambot et al.*[84] The sensing species Os(2,2',2''-terpyridine)$_2^{2+}$ **23** was immobilised in the biocompatible polymer silicone. With its strong absorbance in the red and emission in the far red, using chicken skin the sensor was able to measure oxygen transcutaneously. Measurements were made using either phase modulation fluorimetry or monitoring the fluorescent emission intensity, although the latter was unstable due to variation in the complex concentration as a direct result of leaching and bleaching effects. Intensity measurements were also affected by variations in the thickness of the chicken skin, unlike the phase angle measurements that remained unchanged. In general the Os(II) complex lost partial oxygen quenching sensitivity following immobilisation in the polymer, however reliable measurements could still be made using phase modulation. This example of an optical oxygen sensor highlights the exciting possibilities and potential when the right combination of sensing species, polymer matrix and optical technique are used.

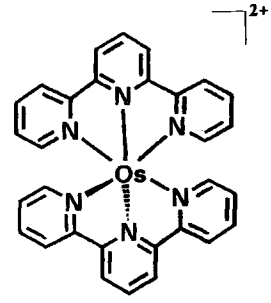

23

Figure 1.20: Os(2,2',2''-terpyridine)$_2^{2+}$ **23**.

1.5.4 Oxygen Sensitive Metalloporphyrins.

Alternative and more sensitive optical sensors have been dominated by systems incorporating platinum metal (Pd, Pt) porphyrins as the sensing species.[74,77,85,86,87] These species absorb and emit in the visible region of the spectrum (~540 nm and 655 nm, respectively), and display strong room temperature phosphorescence and high quantum yields. Also, because these porphyrins don't tend to fluoresce, the problems associated with short-lived background fluorescence are reduced. Compared to the Ru(II) diimine complexes the platinum and palladium porphyrins have longer excited state lifetimes (10's of ms for Pt based complexes and 100's of μs for Pd based complexes). *Yukaka Amao et al*[85] have recently incorporated the commercially available platinum and palladium octaethylporphyrins (PtOEP) **24**, (PdOEP) **25** into poly(isobutylmethacrylate-co-trifluoroethylmethacrylate) thin films. All films were highly sensitive towards the measurement of oxygen in the gas phase.

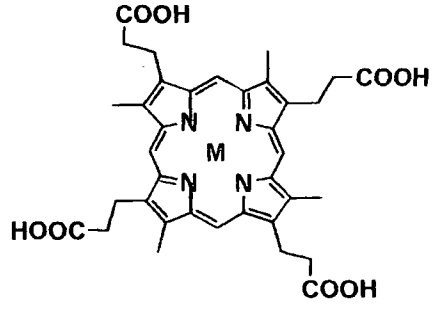

24 M = Pt

25 M = Pd

Figure 1.21: Structures of platinum and palladium octaethylporphyrins (PtOEP) **24**, (PdOEP) **25**.

1.5.5 Lanthanides as Oxygen Sensing Probes.

In recent years a number of reports have appeared of lanthanide complexes that show a dependence of their metal-based emission and luminescent lifetimes to the presence of molecular oxygen. This dependence is not through interaction of molecular oxygen with the lanthanide ion; the line-like emission following direct excitation is independent of oxygen, but simply reflects the quenching of the triplet state of the antenna chromophore following indirect excitation. Calix[4]arenes complexed to Eu^{3+} and Tb^{3+}

ions have been shown to display intensity based oxygen sensitivity,[88] and there have been numerous examples of oxygen dependent metal based emission and luminescent lifetimes of Tb^{3+} complexes based on substituted cyclen (12-N_4)-tri-phosphinates, tetra-amides and mono-amide tricarboxylates.[89,90,33] Recently a series of near-IR luminescent Ln (Yb^{3+}, Nd^{3+}, Er^{3+}) complexes incorporating the organic dyes fluorescein and eosin as the sensitising chromophores have been described with oxygen dependent photophysical properties.[32] All displayed oxygen sensitive luminescent yields, with the Yb^{3+} complex showing the greatest sensitivity due to slow energy transfer from both eosin and fluorescein to Yb^{3+}, which has only one excited state involved in the energy transfer process. A related Gd^{3+} bound fluorexon complex displayed generation of singlet oxygen following the quenching of the Gd^{3+} induced fluorexon triplet state by triplet oxygen. So far the only examples of optical sensing thin films incorporating lanthanide complexes are those decribed by *Amao et al.* Following immobilisation in poly-(styrene-co-2,2,2- TFEM), a series of thin films doped with a Eu^{3+} complex,[91,92] incorporating ((1,10-phenanthroline)tris(thenoyltrifluoroacetonato)) [$Eu(tta)_3phen$] **26**, tris(thenoyltrifluoroacetonato) dihydrate ([$Eu(tta)_3$].$2H_2O$) **27**, tris(1,1,1-trifluoro-5,5-dimethyl-2,4-hexanedionato) dihydrate ([$Eu(pta)_3$].$2H_2O$) **28** or tris(1,1,1,2,2,3,3-heptafluoro-7,7-dimethyl-4,6-octanedionato) dihydrate ([$Eu(fod)_3$].$2H_2O$) **29**, displayed linear Stern-Volmer plots showing modest sensitivity towards the sensing of oxygen in the gas phase. An alumina film doped with tris(acetylacetonato)1,10-phenanthroline Tb^{3+} [$Tb(acac)_3phen$] **30** used to sense oxygen in the gas phase displayed a curved Stern-Volmer plot that is characteristic of multi-site quenching.[93]

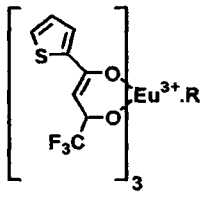

26 [Eu(tta)$_3$phen], R = 1,10-phenanthroline

27 ([Eu(tta)$_3$].2H$_2$0), R = (H$_2$0)$_2$

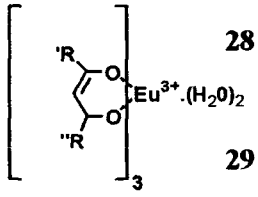

28 ([Eu(pta)$_3$].2H$_2$0), 'R = C(CH$_3$)$_3$ "R = CF$_3$

29 ([Eu(fod)$_3$].2H$_2$0), 'R = C(CH$_3$)$_3$ "R = CF$_2$CF$_2$CF$_3$

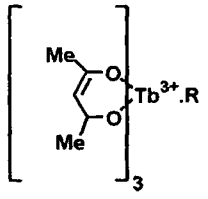

30 [Tb(acac)$_3$phen], R = 1,10-phenanthroline

Figure 1.22: Structure of lanthanide complexes **26-30**.

1.5.6 Sol-Gel Dissolved Oxygen Sensors.

The development of sol-gel optical sensors for the measurement of DO has been dominated by *MacCraith et al.*[44,94,95,96,97] Their most recent publication[41] reports a DO sensor designed primarily for waste water monitoring. The sensing probe uses phase fluorometry to monitor the oxygen quenched luminescence of the Ru(II) complex **22** that is immobilised in the sol-gel sensing film. The sensor exhibits excellent signal to noise ratio, is fully reversible and has a limit of detection of typically 6 ppb. Both temperature and pressure correction parameters have been included in the calibration protocol.

1.6 References for Chapter 1.

[1] Cottrall R. W., *Chemical Sensors.* Oxford University Press.
[2] Ross J., *Science.* **156**, 1378, 1967.
[3] Moody G. J., Oke R.B., Thomas J. D. R., *Analyst.* **95**, 910, 1970.
[4] Bailey P. L., *Analysis with Ion-Selective Electrodes.* 2nd Edn., Heyden and Son Ltd, London, 1980.
[5] Smith E. B., *Basic Chemical Thermodynamics.* 4th Edn. Oxford University Press Inc., New York. 1990.
[6] Crow D. R., *Principles and Applications of Electrochemistry.* 4th Edn, Blackie Academic and Professional, Glasgow, 1994.
[7] Hamann C. H., Hamnett A., Vielstich W., *Electrochemistry.* Wiley-VCH, Germany, 1998.
[8] Barriada J. L., Brandariz I., Kataky R., Covington A. K., Sastre de Vicente M. E., *J. Chem. Eng. Data.* **46**, 1292, 2001.
[9] Bakker.E., *Electroanalysis.*, **9**, 7, 1997.
[10] Pungor.E., *Electroanalysis.*, **8**, 348, 1996.
[11] Bakker E., Menruva R. K., Pretsch E., Meyerhoff M. E., *Anal. Chem.* **66**, 3021, 1994.
[12] Bakker E., Buhlmann P., Pretsch E., *Chem. Rev.* **97**, 3083, 1997.
[13] Bakker E., Trends in Analytical Chemistry. **16**, 252, 1997.
[14] Umezawa Y., Umezawa K., Sato H., *Pure and Applied Chemistry.* **67**, 507, 1995.
[15] Bakker E., *J. Electrochem. Soc.*, **143**, 1996.
[16] Horvai G., *Trends in Analytical Chemistry.* **16**, 260, 1997.
[17] Bakker E., Pretsch E., Buhlmann P., *Anal. Chem.* **72**, 1127, 2000.
[18] Johnston B., *Ph.D. Thesis.* Durham. 1998.
[19] Gadzeko V. P.Y., Christian G. D., *Analytical Chimica Acta.* **164**, 279, 1984.
[20] Craggs A., Moody G. J., Thomas J. D. R., *J. Chem. Ed.* **51**, 542, 1974.
[21] van den Berg A., van der Wal P. D., Skowronska-Ptasinska M., Sudholter E. J. R., Reinhoudt D. N., *Anal. Chem.* **59**, 2827, 1987.
[22] Fiedler U., *Anal. Chim. Acta.* **89**, 111, 1977.
[23] Iglehart M. L., Buck R. P., *Anal. Chem.* **60**, 290, 1988.
[24] Buhlmann P., Amemiya S., Yajima S., Umezawa Y., *Anal. Chem.* **70**, 4291, 1998.
[25] Lindlar E., Graf E., Niegreisz Z., Toth K., Pungor E., *Anal. Chem.* **60**, 295, 1988.
[26] Bakker E., Willer M., Lerchi M., Seiler K., Pretsch E., *Anal. Chem.* **66**, 516, 1994.
[27] Wayne C. E., Wayne R. P., *Oxford University Press.* 1996.
[28] Lakowicz J. R., *Principles of Fluorescence Spectroscopy.* 2nd Edn., Kluwer Academic/Plenum Publishers, New York 1999.
[29] Sabbatini N., Guardigli M., Lehn J-M., *Coord. Chem. Rev.* **123**, 201, 1993.
[30] Bruce J.I., Lowe P.M., Parker P., in *The Chemistry of Contrast Agents in Medicinal Magnetic Resonance Imaging.* Merbach A. E., Toth E., (Ed.). Chapter 11. John Wiley and Sons, Ltd. England. 2001.
[31] Parker D., Williams J. A. G., *J. Chem. Soc., Dalton Trans.*, 3613, 1996.
[32] Werts M. H. V., *Ph.D. Thesis.* Amsterdam. 2000.
[33] Parker D., *Coordination Chemistry Reviews.* **205**, 109, 2000.
[34] Abusaleh A., Meares C. F., *Photochemistry and Photobiology.* **39**, 763, 1984.
[35] Clarkson I., *Ph.D. Thesis.* Durham. 1999.
[36] Buhlmann P., Pretsch E., Bakker E., *Chem. Rev.* **98**, 1593, 1998.
[37] Lin J., *Trends in Analytical Chemistry.*, **19**, 541, 2000.

[38] Brinker C. J., Scherer G. W., *Sol-gel Science: The Physics and Chemistry of Sol-Gel Processing.* Academic Press. California. 1990.
[39] Wang J., *Analytica. Chimica Acta.* **399**, 21, 1999.
[40] Brinker C. J., Hurd A. J., Schunk P. R., Frye G. C., Ashley C. S., *Journal of Non-Crystalline Solids.* **147-148**, 424, 1992.
[41] MacCraith B. D., Ruddy V., Potter C., Kelly B., McGilp J. F., *Electronics Letters.* **27**, 1247, 1991.
[42] McDonagh C., Kolle C., McEvoy A. K., Dowling D. L., Cafolla A. A., Cullen S. J., MacCraith B. D., *Sensors and Actuators B.* **74**, 124, 2001.
[43] Brinkler C. J., *Journal of Non-Crystalline Solids.* **100**, 31, 1988.
[44] McDonagh C., MacCraith B. D., McEvoy A. K., *Anal. Chem.* **70**, 45, 1998.
[45] McDonagh C., Sheridan F., Butler T., MacCraith B. D., *Journal of Non-Crystalline Solids.* **194**, 72, 1996.
[46] Klein L. C., *Sol-gel Technology for Thin Films, Fibres, Preforms, Electronics and Speciality Shapes.* Noyes. Park ridge N.J. 1998.
[47] Shahriari M. R., Ding J. Y., Tong J., Sigel Jr. G. H., *SPIE Vol. 2068* 224.
[48] Malins C., MacCraith B. D., *Analyst.* **123**, 2373, 1998.
[49] Janata J., *Anal. Chem.* **59**, 1351, 1987.
[50] Leiner M. J. P., Hartmann P., *Sensors and Actuators B.* **11**, 281, 1993.
[51] Mathieu C., *Ph.D. Thesis.* Durham. 2001.
[52] Grant S., Bettencourt K., Krulevitch P., Hamilton J., Glass R., *Sensors and Actuators B.* **72**, 174, 2001.
[53] Grant S., Glass R. S., *Sensors and Actuators B.* **45**, 35, 1997.
[54] Bishop M. L., Duben-Engelkirk J. L., Fody E. P., (Eds) in *Clinical Chemistry: Principles, Procedures, Correlations.* 2nd Edn., Lippincott J. B., Philadelphia, USA, 1992.
[55] Baker M. E. J., Narayanaswamy R., *Sensors and Actuators B.* **29**, 368, 1995.
[56] Lobnik A., Oehme I., Murkovic I., Wolfbeis O. S., *Analytica Chimica Acta.* **367**, 159, 1998.
[57] Chan C-M., Fung C-S., Wong K-Y., Lo W., *Analyst,* **123,** 1843, 1998.
[58] Price J. M., Xu W., Demas J. N., DeGraff B. A., *Anal. Chem.* **70**, 265, 1998.
[59] Su M., Liu Y., M Huimin., M Quanli., Wang Z., Yang J., Wang M., *Chem. Commun.*, 960, 2001.
[60] Brasselet S., Moerner W. E., *Single Mol.* **1**, 17, 2000.
[61] Jin W. J., Costa-Fernandez J. M., Sanz-Medel A., *Analytica Chimica Acta.* **431**, 1, 2001.
[62] Kosch U., Klimant I., Werner T., Wolfbeis O. S., *Anal. Chem.* **70**, 3892, 1998.
[63] Kosch U., Klimant I., Wolfbeis O.S., *Fresenius J Anal. Chem.* **364**, 48, 1999.
[64] Bambot S. B., Sipior J., Lakowicz J. R., Rao G., *Sensors and Actuators B.* **22**, 181, 1994.
[65] Malins C., Glever H. G., Keyes T. E., Vos J. G., Dressick W. J., MacCraith B. D., *Sensors and Actuators B.* **67**, 89, 2000.
[66] Anderson S., Constable E. C., Seddon K. R., Turp J. E., Baggot J. E., Pilling M. J., *J. Chem. Soc. Dalton Trans.* 2247, 1985.
[67] Lowe M. P., Parker D., *Chem. Commun.*, 707, 2000.
[68] Kessler M. A., *Anal. Chem.* **71**, 1540, 1999.
[69] Lobnik, A., Majcen N., Niederreiter K., Uray G., *Sensors and Actuators B.* **74**, 200, 2001.

[70] deSilva A. P., Gunaratne H. Q. N., Rice T. E., *Angew. Chem. Int. Ed. Engl.* **35**, 2116, 1996.
[71] www.neuroskills.com/index.html?main=tbi/anoxia.shtml
[72] Mackereth F.J.H., Heron J., Talling J. F., in *Water Analysis: Some Revised Methods for Liminologists. Freshwater Biological Association, Ambleside, Uk, Ch. 2. 1978.*
[73] Kroneis H. W., Marsoner H. J., *Sensors and Actuators.* **4**, 587, 1983.
[74] Amao Y., Miyakawa K., Okura I., *J. Mater. Chem.*, **10**, 305, 2000.
[75] Charlesworth J. M., *Sensors and Actuators B.* **22**, 1, 1994.
[76] Demas J. N., DeGraff B. A., *Anal. Chem.* **63**, 829, 1991.
[77] Mills A., Lepre A., *Anal. Chem.* **69**, 4653, 1997.
[78] Ishiji T., Kudo K., Kaneko M., *Sensors and Actuators B.* **22**, 205, 1994.
[79] Sang-Kyung L., Yong B. S., Hyeon-Bong P., Seon H. P., *Chemistry letters.* 310, 2001.
[80] Wolfbeis O. S., Klimant I., Werner T., Huber C., Kosch U., Krause C., Neurauter G., Durkop A., *Sensors and Actuators B.* **51**, 17, 1998.
[81] Singer E., Duveneck G. L., Ehrat M., Widmer H. M., *Sensors and Actuators A.* **41-42**, 542, 1994.
[82] Xu W., McDonough R. C., Langsdorf B., Demas J. N., DeGraff B. A., *Anal. Chem.* **66**, 4133, 1994.
[83] Xu W., Kneas K. A., Demas J. N., DeGraff B. A., *Anal. Chem.* **68**, 2605, 1996.
[84] Bambot S. B., Rao G., Romauld M. M., Carter G. M., Sipior J., Terpetchnig E., *Biosensors and Bioelectronics.* **10**, 643, 1995.
[85] Amao Y., Miyakawa K., Okura I., *Analytica Chimica Acta.* **421**, 167, 2000.
[86] Amao Y., Asai K., Okura I., Shinohara H., Nishide H., *Analyst.* **125**, 1911, 2000.
[87] Mills A., *Platinum Metals Rev.*, **41**, 115, 1997.
[88] Steemers F. J., Verboom W., Reinhoudt D. N., van der Tol E. B., Verhoeven J. W., *J. Am. Chem. Soc.* **117**, 9408, 1995.
[89] Parker D., Senanayake P. K., Williams J. A. G., *J. Chem. Soc., Perkin Trans. 2*, 2129, 1998.
[90] Beeby A., Parker D., Williams J. A. G., *J. Chem. Soc., Perkin Trans. 2.*, 1565, 1996.
[91] Amao Y., Okura I., Miyashita T., *Chemistry Letters.* 934, 2000.
[92] Amao Y., Okura I., Miyashita T., *Bull. Chem. Soc. Jpn.*, **73**, 2663, 2000.
[93] Amao Y., Okura I., Miyashita T., *Chemistry Letters.* 1286, 2000.
[94] McEvoy A. K., McDonagh C. M., MacCraith B. D., *Analyst.* **121**, 785, 1996.
[95] McDonagh C. M., Sheilds A. M., McEvoy A. K., MacCraith B. D., Gouin J. F., *Journal of Sol-Gel Science and Technology.* **13**, 207, 1998.
[96] McEvoy A. K., McDonagh C. M., MacCraith B. D., *SPIE Vol. 2508.* 190,1995.
[97] O'Keeffe G., MacCraith B. D., McEvoy A. K., McDonagh C. M., McGilp J. F., *Sensors and Actuators B.* **29**, 226, 1995.

Chapter 2

Ia/IIa Metal Cation Ionophores Based on Neutral Carrier Ligands.

This chapter describes the potentiometric detection of group Ia and IIa metal cations using a novel series of oxa-diisobutylamide ionophores based on cis-cis-1,3,5-cyclo-hexanetriol, which have been compared in standard polyvinyl chloride based ion selective electrodes.

2.1 Biologically Relevant Cations.

The potentiometric determination of the concentration of alkali and alkaline earth metal cations in intracellular and extracellular fluid, is clinically relevant. These ions play significant roles in the regulation of numerous biological processes and the onset of clinical disorders is often associated with hyper or hypo levels of selected ions *in vivo*. The biologically relevant group Ia/IIa metal cations and their adult physiological concentration ranges are shown in Table 2.1.[1]

Concentration /mmol dm^{-3}	**K^+**	**Na^+**	**Ca^{2+}**	**Mg^{2+}**
Extracellular	3.5-5.1	136-146	1.16-1.32	0.7-1.1
Intracellular	~120	~10	<0.005	----

Table 2.1: Adult reference ranges for extracellular and intracellular ion levels.

As the potentiometric determination of these cations is relevant to many clinical applications, it has been the focus of research for many organic and analytical chemists to design and analyze novel selective neutral ionophores that can be incorporated into ISEs.

2.1.1 Potassium Ionophores.

Although K^+ is the dominant intracellular biological cation, physiological functions require the body to maintain a low extracellular concentration. In normal circumstances

only 2% of the total K^+ concentration in the body, is present in the plasma. The potassium ion plays an important role in the regulation of the contraction of the heart. Changes in the concentration of this ion in serum can enhance the risk of cardiac arrhythmia. When K^+ levels in serum increase, the resting potential of the cells decrease and cause the heart rate to slow down. Conversely, a decrease in the K^+ level can lead to a state of hyperpolarization, which diminishes the ability of the muscle fibres to become excited and in extreme cases the heart may cease to contract. Therefore the continuous monitoring of K^+ is desirable in circumstances following surgery, a diabetic coma or shock from burns, each of which can alter the levels of K^+ dramatically[1].

Examples of K^+ ionophores include mono- and bis- crown ethers and valinomycin. The antibiotic valinomycin **31** is commonly used in clinical applications to assess K^+ levels.[2] This biologically active carrier consists of 12 alternating amino acids and hydroxy acids to form a macrocyclic molecule. Its excellent selectivity over Na^+ has been demonstrated in an ISE that was conditioned in K^+ free solutions.[3]

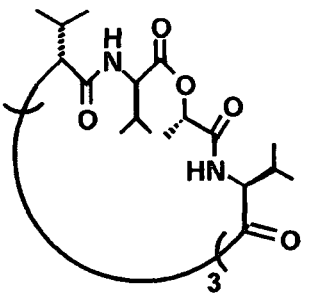

31

$\log K_{K,Na}^{pot} = -4.5$

(SSM, DOS, NaTFPB, Na^+ conditioning)

Figure 2.1: Structure of valinomycin **31**.

Alternative K^+ ionophores are based on mono- or bis-crown ethers. Where the monocrowns (derivatives of 15-crown-5 and 18-crown-6) exhibited poorer selectivity over Na^+ compared to that of **31**, the selectivity displayed by a series of bis-crown ethers **32-35** was more comparable.[3]

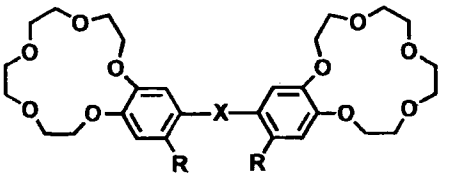

		$\log K_{K,Na}^{pot}$	
32	**X = -$CH_2OCO(CH_2)_5COOCH_2$-, R = H**	**-3.5**	**(FIM, o-NPOE)**
33	**X = -CH_2OCH_2-, R = H**	**-3.6**	**(FIM, DBP)**
34	**X = -$CH(OC_{16}H_{33})CH_2CH_2$-, R = H**	**-3.6**	**(MSM, o-NPOE)**
35	**X = -N=N(O)-, R = H**	**-4.0**	**(SSM, DBP)**

Figure 2.2: Structure of bis-crown ethers **32-35.**

2.1.2 Sodium Ionophores.

High extracellular Na^+ levels require the ionophore to have only a modest selectivity value over K^+, of about $\log K_{Na,K}^{pot} < -0.6$, as the K^+ level in extracellular fluid is significantly lower. Conversely, intracellular measurements are much more demanding as the detection (with less than a 1% error), of Na^+ over K^+ requires a selectivity coefficient of $\log K_{Na,K}^{pot} = -3.5$, due to the high intracellular level of K^+.[4] Synthetic neutral Na^+ selective ionophores have been based on monensin and its derivatives, noncyclic di- and tri-amides, crown ethers and hemispherands.[3]

Calix[4]arenes have generated significant interest as ionophores as they exhibit well-defined cavities and can form inclusion compounds with tailored selectivity depending on the substituents attached to the upper and lower rim.[5] A calix[4]aryl tetraester **36**[6] with *tert*-octyl groups showed pronounced selectivity towards Na^+ over K^+ as did the calix[4]arenecrown-5 derivatives **37**[7] and **38**.[8]

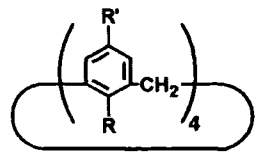

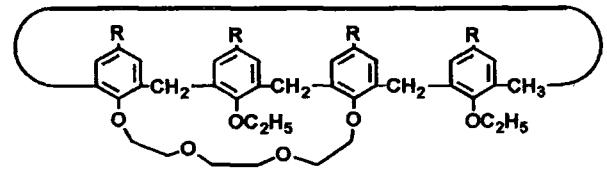

36

R = $OCH_2COOCH_2CH_3$

R' = *tert*-octyl

$logK_{Na,K}^{pot}$ = –3.1 (SSM, FNDPE, KTpClPB)

37 R = H (*partial cone* conformation)

$logK_{Na,K}^{pot}$ = –5.3 (FIM, o-NPOE, KTpClPB)

38 R = $C(CH_3)_3$ (*cone* conformation)

$logK_{Na,K}^{pot}$ = –4.9 (SSM, DOS, KTpClPB, K^+ conditioning)

Figure 2.3: Structure of calixarenes **36-38.**

2.1.3 Lithium Ionophores.

The monitoring of Li^+ levels in patients being treated for manic-depressive psychosis with Li_2CO_3 is desirable as the difference between therapeutic and toxic levels of Li^+ is extremely narrow.[9] The therapeutic range lies between 0.5-1.5 mmol dm^{-3} in whole blood.[10] Below 0.5 mmol dm^{-3} the efficacy of such treatment may be inadequate and levels greater than 1.5 mmol dm^{-3} may be toxic and possibly lethal at concentrations exceeding 5 mmol dm^{-3}. For 'ideal' measurements of Li^+ in blood, a selectivity value of $logK^{pot}_{Li,Na}$ = -4.5 is required.[10,11] However, most synthesized ionophores do not display adequate selectivity for the determination of Li^+ in the presence of Na^+, which represents ~ 90% of all extracellular cations.

Numerous neutral carrier ionophores, which are selective towards Li^+ incorporate either 14-crown-4 frameworks bearing di-amide substitution[9,10,12], or systems incorporating di-carboxamide functionality.[13,14] In the latter class, modest selectivity was displayed by the complex N,-N-dicyclohexyl-N',N'-diisobutyl-cis cyclohexane-1,2-dicarboxamide (ETH1810) **39**.[13]

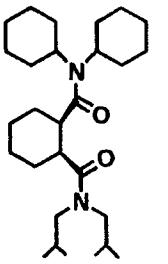

39

$\log K_{Li,Na}^{pot}$ = -2.45

(FIM, o-NPOE, KTpClPB)

Figure 2.4: Structure of N, N-dicyclohexyl-N',N'-diisobutyl-cis cyclohexane-1,2-dicarboxamide (ETH1810) **39**.

Research directed at the enhancement of Li^+ selectivity over Na^+ for 14-crown-4 systems has been explored by *Parker et al.*[9,11,12] Early work reported that pendant CH_2CONR_2 moieties were able to bind to Li^+ in the plane of the ring. Such amide substituents were chosen to enhance the selectivity of the charge dense lithium ion. They were also sufficiently lipophilic to be incorporated into polymeric membranes and their steric bulk was thought to disfavour the formation of a 2:1 complex with the competitive sodium ion. Subsequently the modification of the amide disubstituent from the *n-butyl* **41** to isobutyl **40** analogue displayed enhanced selectivity towards Li^+ over Na^+.

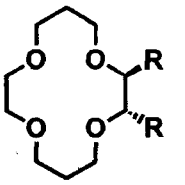

40 R = $[CH_2CON(^iBu)_2]$ $\log K^{pot}_{Li,J}$ = -3.25

41 R = (CH_2CONBu_2) $\log K^{pot}_{Li,J}$ = -2.92

(FIM, o-NPOE, KTpClPB, (150 mmol dm^{-3} Na^+, 4.3mmol dm^{-3} K^+, 1.26mmol dm^{-3} Ca^{2+}

Figure 2.5: Structure of 14-crown-4 systems **40-41.**

Related studies with amide substitution on the central methylene of similar macrocyclic crown ether systems bearing mono and gem-dialkyl substitution, displayed pronounced

Li^+/Na^+ selectivity compared to the other ligating substituents i.e. CH_2OMe, CH_2CONEt_2 or $CH_2OPO\text{-}(OEt)_2$.

2.1.4 Calcium Ionophores.

The first neutral Ca^{2+} selective ionophores were based on non cyclic 3,6-dioxaoctanedioic diamides.[3] A commercial ionophore based on this ligand class is (-)-(R,R)-N,N'-bis[11-(ethoxy-carbonyl)undecyl]-N,N'-4,5-tetramethyl-3,6-dioxaoctanediamide (ETH1001) **42**. The two amide oxygens are essential for Ca^{2+} selectivity where the ester groups are not considered to participate in complexation. Following incorporation in standard ISEs the complex is thought to adopt a 1:2 stoichiometry with Ca^{2+}.

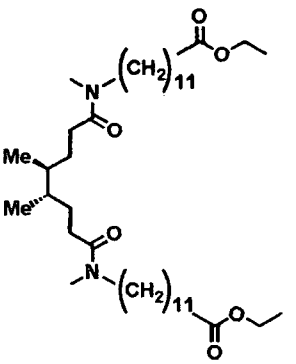

42

	$\log K_{Ca,J}^{pot}$
(SSM, o-NPOE, KTpClPB)	**H^+ -4.4**
	K^+ -3.8
(FIM, o-NPOE, KTpClPB, Ca^{2+} buffer)	**K^+ -6.6**

Figure 2.6: Structure of (-)-(R,R)-N,N'-bis[11-(ethoxy-carbonyl)undecyl]-N,N'-4,5-tetramethyl-3,6-dioxaoctanediamide (ETH1001) **42**.

An alternative commercial Ca^{2+} selective ionophore based on the diamide framework is N,N,N'N'-tetracyclohexyl-3-oxapentanediamide (ETH129) **43**. Despite significant interference from H^+, ETH129 has displayed high selectivity over K^+ and Na^+, where both the ISE inner electrolyte and conditioning solution were 0.01 mol dm^{-3} NaCl.[8] Both ETH129 and ETH1001 are considered suitable for clinical applications, whilst ETH129 is considered the ionophore of choice for intracellular measurements.

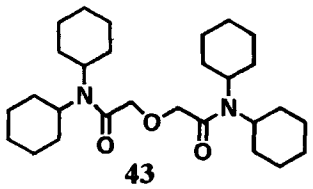

43

	$\log K_{Ca,J}^{pot}$
(SSM, o-NPOE, KTpClPB)	**H^+ -1.6**
	K^+ -4.0
(FIM, o-NPOE, KTpClPB, Ca^{2+} buffer)	**K^+ -8.0**
(SSM, o-NPOE, KTpClPB, Na^+ conditioning)	**K^+ -10.1**

Figure 2.7: Structure of N,N,N'N'-tetracyclohexyl-3-oxapentanediamide (ETH129) **43**.

2.1.5 Magnesium Ionophores.

Magnesium is a vital nutrient and its deficiency *in vivo* can have a significant influence on cardiovascular function, diabetes, bone deterioration and renal failure.[15] Alcohol is considered the most prominent Mg^{2+} wasting drug.[16] Its effects are considered to induce hypertension and stroke through the modulation of intracellular free Mg^{2+}. Magnesium ISEs are attractive as they offer a means to measure free Mg^{2+} ions, which is the physiologically active form. One ionophore that displays discrimination of physiological interfering cations against Mg^{2+} is (N,N',N''-imino-di-6,1-hexanediyl)tris(N-heptyl-N-methyl-malonamide), ETH 5282 **44**. This tripodal ligand, incorporating 6 amide groups, displayed the first accurate Mg^{2+} measurement in undiluted blood serum, provided corrections for the interference from Ca^{2+} activity at physiological concentrations, were made.[3,17]

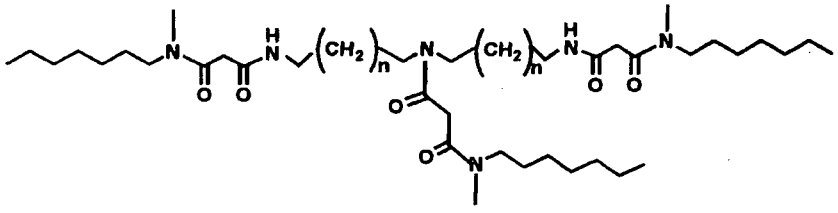

44

$\log K_{Mg,J}^{pot}$ (SSM, o-NPOE, KTpClPB)		
	Ca^{2+}	-0.8
	Na^{+}	-3.9
	K^{+}	-2.4

Figure 2.8: Structure of (N,N',N''-imino-di-6,1-hexanediyl)tris(N-heptyl-N-methyl-malonamide), ETH 5282 **14**.

The greatest challenge with respect to Mg ISEs is the discrimination of Ca^{2+}. Good discrimination of Ca^{2+} was displayed with the crown ether ionophore K22B5 **45**, which incorporated two pendant malonamide side-arms with adamantyl functionality. Despite excellent selectivity over Ca^{2+}, substantial interference from other alkali metal ions was observed.[18]

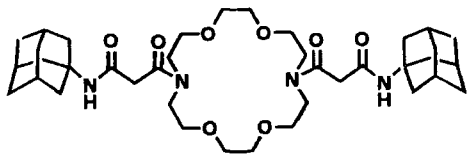

45

$\log K_{Mg,J}^{pot}$ (SSM, o-NPOE, KTpClPB)		
	Ca^{2+}	-2.5
	Na^{+}	-3.2
	K^{+}	-1.5

Figure 2.9: Structure of K22B5 **45**.

2.2 Evaluation of Novel *cis-cis*-1,3,5-cyclohexanetriol Ligands as Potential Ionophores for Ia and IIa Metal Cations.

The behaviour of a series of novel diisobutyl amide ligands based on a *cis-cis* -1,3,5-cyclohexanetriol framework as ionophores for the detection of selected IA/IIA cations was compared in standard PVC–based ISEs. The results were compared with a previously established *n*-butyl amide series **46-48** that was synthesized at Durham University by *Goodall*.[4]

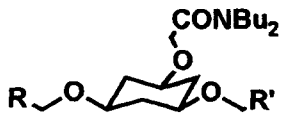

46 R = Pr = R'

47 R = $CONBu_2$, R' = Pr

48 R = $CONBu_2$ = R'

Figure 2.10: Structure of n-butyl amide series **46-48**.

A summary of the electrode response parameters for ISEs incorporating ligands **46-48** is shown in Table 2.2.[19]

Calibration				**Selectivity: pK_{ij}^{pot} (FIM, *j* = *0.1 mol dm^{-3}*)**				
Ligand	Primary ion	Slope/ mV	Detection limit	Na^+	K^+	Mg^{2+}	Ca^{2+}	Li^+
Mono-amide **46**	Na^+	60.0	$10^{-4.8}$	-	0.6	1.3	0.8	0.1
	Li^+	56.0	$10^{-5.1}$	0.7	1.2	2.1	1.3	-
Di-amide **47**	Na^+	57.2	$10^{-4.8}$	-	1.7	1.9	0.5	0
	Li^+	57.0	$10^{-5.6}$	2.2	3.8	3.6	2.1	-
	Ca^{2+}	27.4	$10^{-5.2}$	0.6	3.6	4.2	-	-0.9
Tri-amide **48**	Na^+	55.5	$10^{-5.9}$	-	3.1	2.7	0.8	0.1
	Li^+	58.4	$10^{-5.8}$	0.8	3.4	3.2	1.3	-
	Ca^{2+}	27.7	$10^{-6.6}$	-0.6	3.9	4.0	-	-0.9

Table 2.2: Electrode response parameters and selectivity coefficients for ISEs based on ligands **46-48** (310 K, o-NPOE, NaTFPB).

Marked selectivity was displayed for Li^+ over Na^+ by **47.** The measured value of $10^{2.2}$ was significantly high for a non-macrocyclic ionophore. Excellent selectivity was also displayed by the ISE incorporating **48** and o-NPOE as the plasticizer, in which a reported value of $10^{3.1}$ was displayed for Na^+ selectivity over K^+.

2.2.1 Ionophore Design.

Alkali and alkaline earth metal cations are classified as hard Lewis acids and interact preferably with hard Lewis bases such as oxygen atoms. For ions of relatively high charge density e.g. Li^+, hard σ donors with large dipole moments such as amide carbonyl oxygens are preferred.[20] Tertiary amides can also be rendered sufficiently lipophilic to avoid leaching from the polymeric membrane into the aqueous phase. Characteristics of the biologically relevant alkali and alkaline earth metal cations are shown in Table 2.3.[17]

Features	K^+	Na^+	Ca^{2+}	Mg^{2+}	Li^+
Ionic radius/pm	138	102	100	72	76
Co-ordination number	6-8	6	6-8	6	4-6
Preferred donor atom type	ether O, ester CO	ether O, amide CO	N, amide CO	O, N, $O=P(O)_3^-$	P=O, amide CO

Table 2.3: The physicochemical characteristics of the 5 biologically relevantalkali-alkaline earth metal cations.

Ionophore design was based on the *cis-cis*-1,3,5-cyclohexanetriol system. Ligands incorporating this framework predominantly adopt a chair conformation with the pendant substituents in equatorial positions. Inter-conversion to a pseudo-adamantyl 'array' is promoted on complexation to the cations.

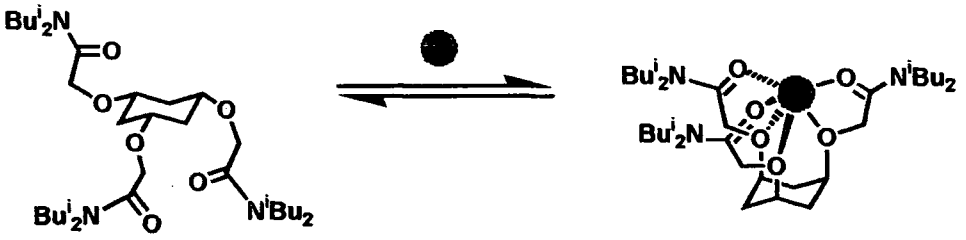

Figure 2.11: Interconversion of chair conformation to a pseudo-adamantyl 'array'.

The length of the side chains was chosen to optimise oxygen-cation interactions. The ether oxygens not only served as complexation sites, but also introduced flexibility into the substituents, allowing them to move rapidly between axial and equatorial positions and therefore display rapid kinetics of complexation, which is vital for quick transportation of the cation if Nernstian behaviour is to be obeyed. Substitution of the

amide nitrogens with diisobutyl groups was chosen to enhance the lipophilicity of the ligands. Incorporating these structural considerations into the tripodal framework, mono-, di- and tri- substituted diisobutyl amide ligands, **49-51** respectively, were synthesized at Durham University by Dr. Ofer Reany to give ligands with possible coordination numbers of 4, 5 and 6 respectively, assuming a 1:1 cation:ionophore stoichiometry.

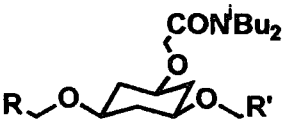

49 R=H=R'

50 R=CON^{i}Bu$_2$;R'=H

51 R=CON^{i}Bu$_2$=R'

Figure 2.12: Structure of diisobutyl amide series **49-51**.

2.3 Electrode Response Studies.

The behaviour of ligands **49-51** as potential ionophores for the detection of selected IA/IIA cations was compared in standard PVC based membrane ISEs. The effect of the choice of plasticizer on the electrode response was also studied. Details concerning membrane fabrication and potentiometric methods for electrode calibration and selectivity measurements are given in Sections 5.1.1-5.1.5 respectively.

2.3.1 Detection of Potassium.

The response of ionophores **49-51** towards the detection of K^+, incorporating either o-NPOE or DOS as the plasticizer, is shown in Figure 2.13.

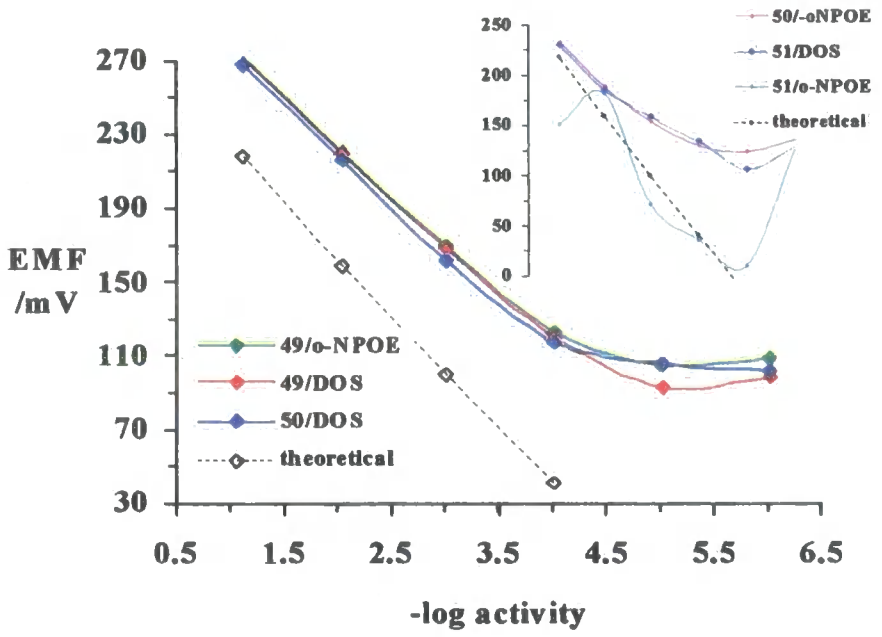

Figure 2.13: The detection of K^+ using substituted cyclohexyl amide ionophores incorporated in o-NPOE or DOS plastisized PVC membrane ISEs (298 K, KTpClPB). (*inset*;non-Nernstian behaviour).

Membranes incorporating **49** with either o-NPOE or DOS plasticizer, and **50** with DOS plasticizer displayed a reasonable response towards the detection of K^+. Slope values and detection limits are given in Table 2.4.

Ligand/plasticizer	Slope/mV	Detection Limits
49 /o-NPOE	52.2	$10^{-4.5}$
49 /DOS	52.3	$10^{-4.6}$
50 /DOS	52.3	$10^{-4.2}$

Table 2.4: Slopes and detection limits in K^+ analysis for membranes incorporating **49** with either o-NPOE or DOS plasticizer, and **50** with DOS plasticizer.

Accordingly, the slopes values were slightly sub-Nernstian. On increasing the amide substitution a significant deviation from Nernstian behaviour was observed (Figure 2.13:*inset*). These results could be attributed to the fact that K^+ does not favour amide oxygens as potential coordination sites, but has a preference for either ether oxygens or hydroxyl oxygens. In previous studies concerning the trioxa-cyclohexane based ligands

using IR spectroscopy, no amide carbonyl ligation was observed for the K^+ complexes of the di-**47** and tri-**48** oxaamide n-butyl derivatives.[21]

2.3.2 Detection of Sodium.

Electrodes examined comparatively towards the detection of Na^+ showed no improvement in the electrode response. For the detection of Na^+ it was apparent that the response was being governed mainly by the choice of plasticizer, and not by the choice of ligand. Improved electrode responses for the detection of Na^+ were observed for membranes incorporating DOS plasticizer (Figure 2.14) even although they displayed sub-Nernstian slopes and very modest detection limits, as shown in Table 2.5.

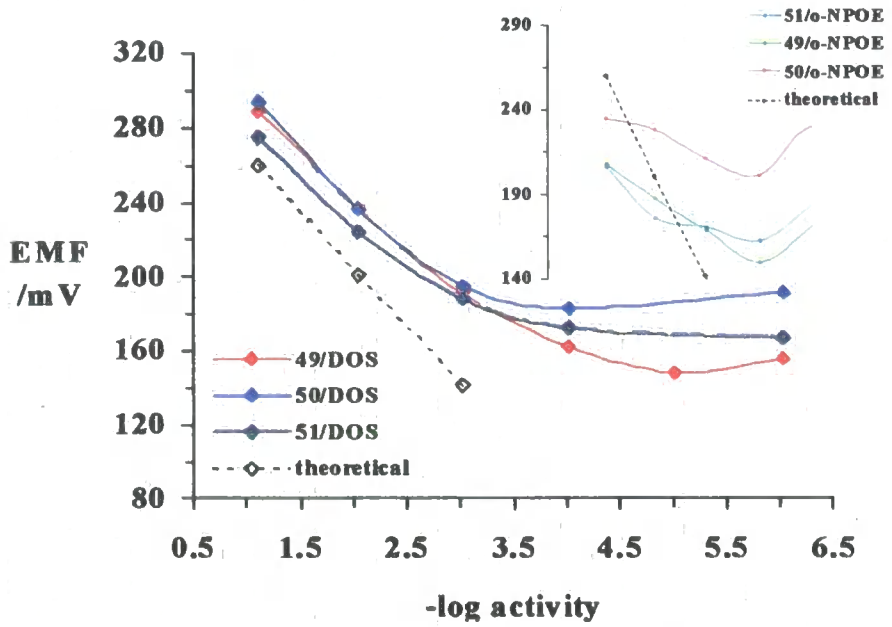

Figure 2.14: The detection of Na^+ using substituted cyclohexyl amide ionophores incorporated in o-NPOE or DOS plasticized PVC membrane ISEs (298 K, KTpClPB). (*inset*;non-Nernstian behaviour).

Ligand/plasticizer	Slope/mV	Detection Limits
49 /DOS	51.2	$10^{-3.7}$
50 /DOS	51.9	$10^{-3.0}$
51 /DOS	45.5	$10^{-3.0}$

Table 2.5: Slopes and detection limits in Na^+ analysis for membranes incorporating **49**, **50**, **51** and DOS plasticizer.

Such a result is hardly surprising as it has been reported that neutral ionophores tend to form complexes with monovalent rather than divalent cations when the dielectric constant (ε_r) of the surrounding medium is low, and especially when $\varepsilon_r < 10$.[22] The choice of plasticizer and the proportion of PVC:plasticizer governs the ε_r of the PVC based membrane. Generally, the plasticizer accounts for ~60-70% w/w of the membrane. Hence the ε_r value of such membranes should be similar to that of the pure liquid plasticizer. This has been observed in previous reports where an ε_r-value of 4.8 was observed for a (PVC 33%) – DOS membrane compared to a value of 4.2 for liquid DOS, where the slight increase in the value for the membrane was attributed to the movement of C-Cl bonds in the presence of an electric field.[23] Therefore DOS is the preferred plasticizer for alkali cation-selective membranes, where a plasticizer of higher ε_r such as o-NPOE, should be used in membranes for alkaline-earth cation selective applications.

2.3.3 Detection of Lithium.

For the detection of Li^+, only the response of the ISE incorporating **50** was investigated to allow comparison with the previous di-oxa-amide *n*-butyl anologue **47**, which behaved as an excellent ionophore for Li^+, and displayed a marked selectivity value of $10^{2.2}$ for Li^+ over Na^+. The response of the ISE incorporating **50**, which is shown in Figure 2.15, exhibited a significant deviation from Nernstian behaviour with a slope factor of 34 mV being observed. Such deviation may be due to the ligand binding too strongly to Li^+, which could impede rapid transport of Li^+ at the interfacial region of the membrane and thus prevent chemical equilibrium from being properly established.

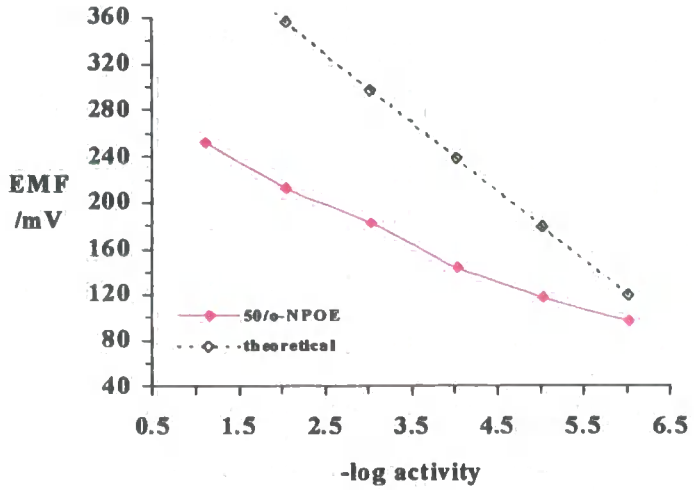

Figure 2.15: The detection of Li^+ using **50** incorporated in an o-NPOE plasticized PVC membrane ISE (298 K, KTpClPB).

2.3.4 Detection of Magnesium.

For the detection of Mg^{2+} only ISEs incorporating **50** displayed reasonable behaviour, with super-Nernstian slopes being observed at higher activities (Figure 2.16).

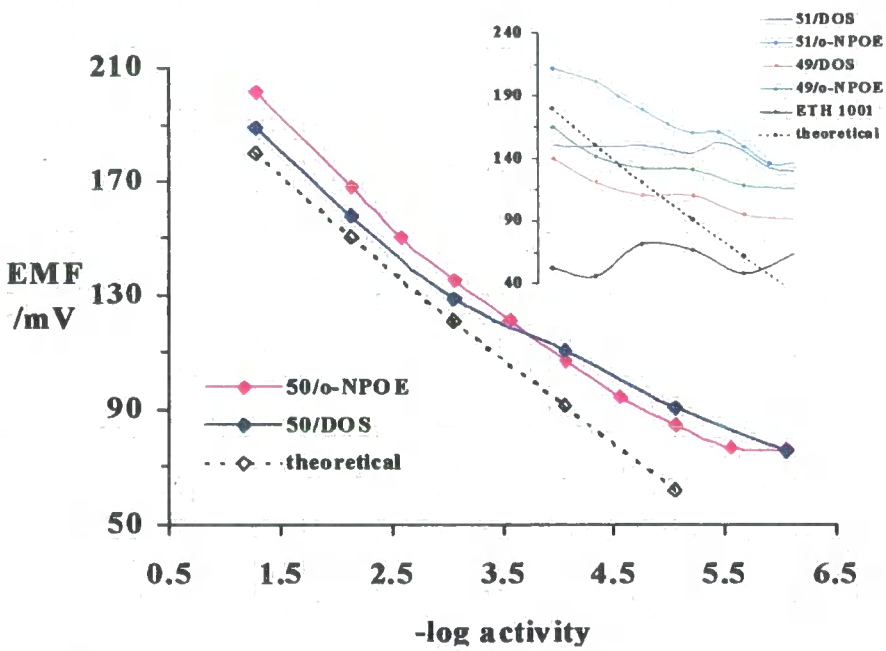

Figure 2.16: The detection of Mg^{2+} using substituted cyclohexyl amide ionophores incorporated in o-NPOE or DOS plasticized PVC membrane ISE (298 K, KTpClPB). (*inset*;non-Nernstian behaviour).

The detection limit for the membrane incorporating the o-NPOE plasticizer was significantly better than that containing DOS, as observed in Table 2.6. Again this trend may be attributed to the biased selectivity of the plasticizer o-NPOE towards the detection of alkaline earth metals, compared to that of DOS, due to the relative dielectric constants of each material.

Ligand/plasticizer	Slope/mV	Detection Limits
50 /o-NPOE	37.7	$10^{5.0}$
50 /DOS	33.9 changing to 17.6	$10^{3.1}$

Table 2.6: Slope factors and detection limits for membranes incorporating **50** with either o-NPOE or DOS plasticizer.

2.3.5 Detection of Calcium.

An excellent response towards the detection of Ca^{2+} was observed with the diamide ionophore **50** (Figure 2.17). Comparison with an ISE incorporating the commercially available Ca^{2+} selective ETH1001 ionophore **42**, revealed similar behaviour with respect to detection limits and Nernstian slopes.

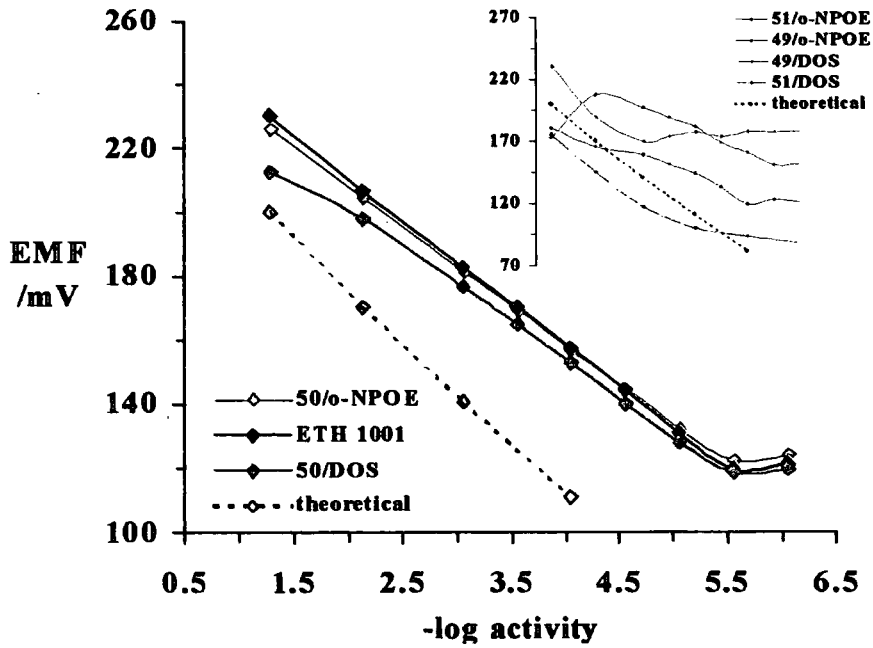

Figure 2.17: The detection of Ca^{2+} using substituted cyclohexyl amide ionophores incorporated in o-NPOE or DOS plasticized PVC membrane ISE (298 K, KTpClPB). (*inset*;non-Nernstian behaviour).

As Ca^{2+} prefers a co-ordination sphere of at least 6 and preferably 8 sites, such a response may indicate a 2:1 ionophore-cation stoichiometry. Further evidence for the formation of a relatively stable ($4.5 \leq \log K \leq 5.5$) 2:1 ionophore **50**–Ca^{2+} complex was provided by ^1H NMR titration data.[24] Again, the membrane incorporating the relatively polar plasticizer o-NPOE displayed a slightly improved response compared to that for the DOS based membrane, due to the divalent cation selectivity and transport being favoured by the relative permittivity of the o-NPOE based membrane. The slopes and detection limits for the membranes incorporating **50** and ETH1001 **42** are shown in Table 2.7.

Ligand/plasticizer	Slope /mV	Detection Limits
50 /o-NPOE	24.6	$10^{-5.8}$
50 /DOS	24.4	$10^{-5.7}$
42 /o-NPOE	25.6	$10^{-5.8}$

Table 2.7: Slopes and detection limits in Ca^{2+} analysis for membranes incorporating **50** with either o-NPOE or DOS plasticizer, and ETH1001 **42** with o-NPOE plasticizer.

Sub-Nernstian behaviour was observed with the ionophores **49** and **51** respectively (Figure 2.17:*inset*). The non-linear response displayed by ionophore **49** may be attributed to insufficient binding of the complex with Ca^{2+} due to its low number of co-ordination sites, which is not favoured by the metal. Contrasting results were observed for ionophore **51**. With this ligand a modest detection limit of approximate 10^{-3} was observed for the membrane incorporating the DOS plasticizer. On changing to o-NPOE plasticizer the detection limit increased to approximately 10^{-5}. This again highlights the preference of plasticizers with higher dielectric constants for divalent cations. The sub-Nernstian response of the triamide ionophore **51** suggested that this ionophore may be binding too strongly to Ca^{2+}. This could result in slow decomplexation kinetics that would prevent rapid transport of the ion from occurring at the interfacial region of the membrane. Such behaviour is consistent with the reported stabilities of the *n*-butylamide Ca^{2+} complexes. ^{13}C NMR titration data revealed a marked difference in the binding strength of the 1:1 Ca^{2+} complex of the trioxa-amide ($10^{>5.5}$) compared with the dioxa-amide ($10^{3.6}$).[21] Donnan failure can occur in cases where the ionophore binds too strongly to the primary ion. At high concentrations typical of 10^{-2} mol dm^{-3} co-extraction of the primary ion electrolyte into the membrane can influence the EMF of

the ISE i.e the membrane permselectivity breaks down and the ISE begins to respond to anions. Such behaviour has been observed in Ca^{2+} ISEs incorporating o-NPOE as plasticizer,[25] and may be responsible for the deviation from linearity observed in the response of **51**/o-NPOE in the concentration range above 10^{-2} mol dm^{-3}. Other possible explanations that may account for the sub-Nernstian response of ionphore **51** include (i) the complexation with Ca^{2+} is too sterically demanding, (ii) the lipophilicity of the ionophore is too high. Such phenomena could impose severe limitations on the rapid transport kinetics from occurring at the membrane interface.

2.4 Selectivity.

The selectivity of the Ca^{2+} ISE incorporating the diamide ionophore **50** was determined using the Fixed Interference Method (FIM) as described in Section 5.1.4. The FIM method was chosen so a direct comparison could be made between the previous *n*-butyl and the novel diisobutyl series. Also, the electrode slopes for ionophore **50** were close to Nernstian for most of the measured ions, thus indicating reversible binding behaviour, which is a necessary condition for the determination of true selectivity coefficients. Compared to selectivity data for the ISE incorporating the di-*n*-butylamide **47**,[21] the diisobutyl analogue displayed a significantly different pattern of selectivity coefficients for Ca^{2+} as primary ion, as depicted in Figure 2.18.

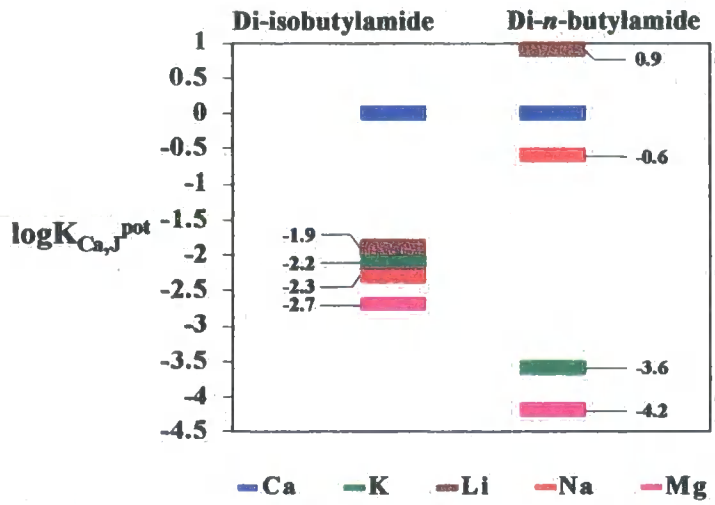

Figure 2.18: Comparison of the selectivity coefficients for Ca^{2+} ISE's incorporating the diisobutylamide ionophore **50** and the di-*n*-butylamide ionophore **47**, (298 K, FIM: 0.1 mol dm^{-3} JCl, where J = interfering ion).

Where the di-*n*-butylamide ionophore **47** displayed marked selectivity for Ca^{2+} over K^+ and Mg^{2+} of $10^{-3.6}$ and $10^{-4.2}$, it displayed poor selectivity over Na^+ and Li^+ of $10^{-0.6}$ and $10^{0.9}$ respectively. Conversely, the diisobutyl analogue exhibited enhanced selectivity over Na^+ and Li^+ of $10^{-2.3}$ and $10^{-2.7}$, but less good discrimination over K^+ and Mg^{2+} of $10^{-2.2}$ and $10^{-2.7}$ respectively. The trend in ion selectivity displayed by the diisobutyl analogue and deduced from the electrode response studies showed a relatively similar trend in selectivity when compared with data observed from related electrospray mass spectroscopic studies in which the binding preference of the ligand was observed to follow the order of $Li^+ > Na^+ > K^+$.[24]

The response of the Ca^{2+} ISE incorporating the diamide ionophore **50** and o-NPOE plasticizer was measured in the presence of a simulated extracellular background of interfering ions using the technique of Constant Volume Dilution (Section 5.1.5). Given that the free extracellular Ca^{2+} concentration range is typically between 1.16 and 1.32 mmol dm^{-3}, the electrode displayed a linear response towards Ca^{2+} over this activity range, with a nearly Nernstian slope of 25 mV per activity decade, as shown in Figure 2.19.

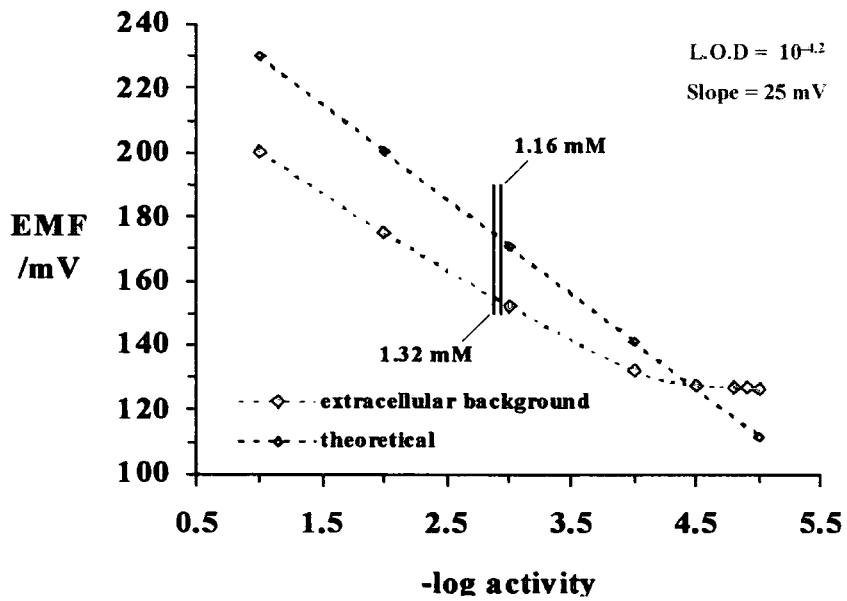

Figure 2.19: Response curve for Ca^{2+} obtained with the ISE incorporating ionophore **50** and o-NPOE, in the presence of interfering ions of similar concentration to those found in extracellular fluids, (140 mmol dm^{-3} Na^+, 4.3 mmol dm^{-3} K^+, 0.9 mmol dm^{-3} Mg^{2+}), 298 K.

2.5 The Effect of pH on the Ca^{2+} ISE.

In the blood approximately 50% of calcium exists as the free ion, with 45% being bound to proteins such as albumin and the remaining 5% being complexed to several biological anions such as citrate. Therefore, the concentration of ionised Ca^{2+} in the plasma predominantly depends on the amount of protein present and the pH of the sample.[1,26] One of the predominant buffer systems of the blood plasma is the bicarbonate–carbonic acid system.[1]

$$\underset{\text{Gas}}{CO_2} \rightleftharpoons \underset{\text{dissolved in plasma}}{CO_2 + H_2O} \rightleftharpoons \underset{\text{Carbonic acid}}{H_2CO_3} \overset{pK_a\ 6.1}{\rightleftharpoons} \underset{\text{Bicarbonate}}{HCO_3^- + H^+}$$

Figure 2.20: Bicarbonate – carbonic acid buffer system.

Consequently a loss of CO_2 from the blood sample will result in a pH change with a consequent change in the proportion of Ca^{2+} unbound. For a high discrimination against H^+ interference, the ionophore should ideally not incorporate functional groups that can be easily protonated. Hence the more acidic the ionophore, the better the immunity from H^+ interference. Hydrogen ion interference can be expressed either as a constant of selectivity or an operative pH range.[3] Accordingly, the effect of proton interference on the response of the Ca^{2+} ISE was assessed.

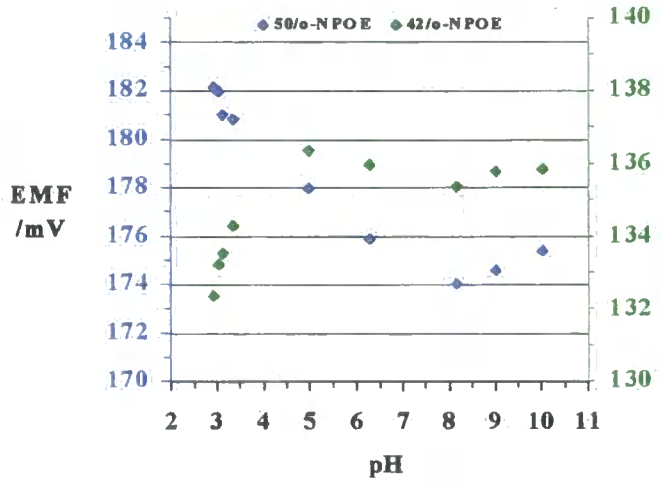

Figure 2.21: pH effect on ISE's incorporating **50** and ETH1001 **42** and o-NPOE plasticizer (298 K).

As observed in Figure 2.21 the ISE incorporating the diamide ionophore **50** did suffer some degree of H^+ interference. In going from pH 8 to pH 3, there was a steady increase in the EMF, which can be associated with H^+ interference. The deviation in EMF was 4 mV for the clinically relevant pH range of 5–8. This is a significant deviation when compared to the response for the ionophore ETH1001 **42**. In this case a deviation of 1.7 mV was observed between the pH range of 5-8.

2.6 Lowering Detection Limits.

The lower limit of detection of ionophore based polymeric ISEs usually fall within the activity range of 10^{-4} mol dm^{-3} to 10^{-6} mol dm^{-3}, except when the activities of the primary ion have been adjusted using ion metal buffers.[27,28] Lately there has been a significant interest concerning the chemistry that governs the lower limit of detection of such ISEs. Indeed related thin film optical sensors that incorporate the respective selective chemical ionophore have been known to display noticeable lower detection limits than their potentiometric counterparts. The most conspicuous difference in the make-up of these optical sensors was the lack of the inner electrolyte or inner filling solution. This observation coupled with the fact that lower values were observed when metal ion buffers were used supported the hypothesis that primary ions, originating from the IFS and leaching out from the sensor membrane into the sample solution, were dictating the lower limit of the measuring range. However, as a lower measuring range was not observed in solid contact electrodes that are also free of a IFS, the transport of primary ions across the membrane, and originating from the IFS is not considered to be the sole determining factor.[29]

Traditionally, the concentration of the IFS is ~ 10^{-3} mol dm^{-3}. Such high concentrations can cause co-extraction of the electrolyte into the membrane by the ionophore at the membrane/IFS interface. This generates a concentration gradient and flux of the electrolyte from the IFS, across the membrane and into the sample 'local' to the membrane/sample interface. The maximum gradient and flux is considered achieved when all the ionophore molecules are complexed at the membrane/IFS boundary. Since ISEs are responsive to phase boundary activities, it can be expected that the ISE will become insensitive to any changes in the primary ion activity, if the concentrations of

the primary ions being released from the membrane exceeds the concentration of primary ions in the dilute sample bulk.[29]

Recently detection limits ranging from approximately the nanomolar to picomolar range have been achieved when buffering the primary ion activity in the inner filling solution using an ion buffer.[28,30,31,32] In conjunction with the ion buffer a high concentration of interfering ion must also be present in the IFS. These interfering ions exchange with the primary ions at the membrane /IFS interface and induce a flux that prevents the primary ions leaching out the membrane and into the sample solution, thus enhancing the detection limit. The basic theory concerning such advances focuses on the elimination of the co-extraction and ion-exchange processes that influences the limit of detection. A schematic representation[33] of the influence that these processes have on the detection limits of ISEs in dilute samples is given in Figure 2.22.

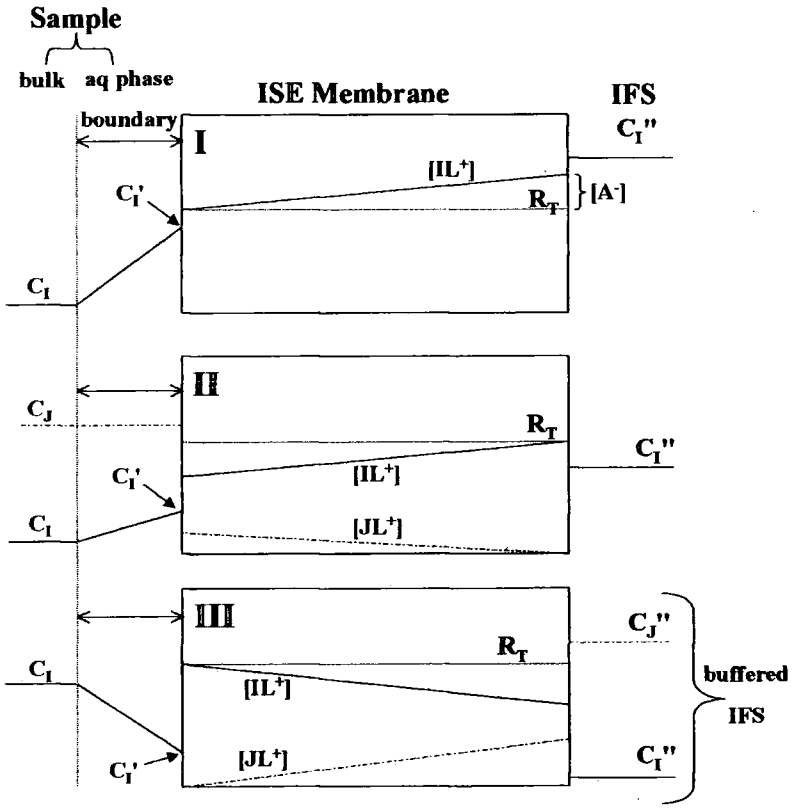

Figure 2.22: Schematic representation of the processes that can influence the lower limit of detection of ISEs incorporating an ionophore. (C_I = primary ion concentration, C_J = interfering ion concentration, $[IL^+]$ = primary ion-ionophore complex concentration, $[JL^+]$ = interfering ion-ionophore complex concentration, R_T = total concentration of lipophilic anions, ' donates the sample phase boundary, " donates the IFS phase boundary).

Such observations can be interpreted in terms of ion-exchange processes and their associated steady-state ion fluxes generated under zero current conditions. The assumptions made to define this theory are given elsewhere.[33] In box I, the primary ion electrolyte is co-extracted from the IFS and transported down the concentration gradient where it leaches into the dilute sample. Here the limit of detection is governed by the concentration of the primary ion at the aqueous phase boundary, which may be greater than the dilute sample bulk concentration due to this leaching process. The exchange of primary ions by interfering ions can also induce concentration gradients and ion fluxes, even when the co-extraction of the electrolyte from the IFS is minimal, as shown in box II. In box III the concentration of primary ions in the IFS has been reduced significantly, as would be the case where a metal ion buffer was used. A high concentration of interfering ion is also present. In reducing the concentration of the primary ion in the IFS, the flux of primary ions across the membrane and towards the sample phase as shown in box I is eliminated. Instead a flux of primary ions originating now in the sample is induced towards the IFS. The high interfering ion activity is required to maintain its ionic gradient and exchange with the primary ions at the IFS side of the membrane. Through eliminating or reversing the effects depicted in boxes I and II, a lower limit of detection is obtained.

Accordingly, this theory was applied to ISEs incorporating the diamide ionophore **50** in a o-NPOE plasticized membrane, and the o-NPOE membrane incorporating ionophore **42**. Details of the experimental procedure including the composition of the Ca^{2+} IFS metal buffer is described in Section 5.1.7. Responses for the three ISEs are shown in Figure 2.23.

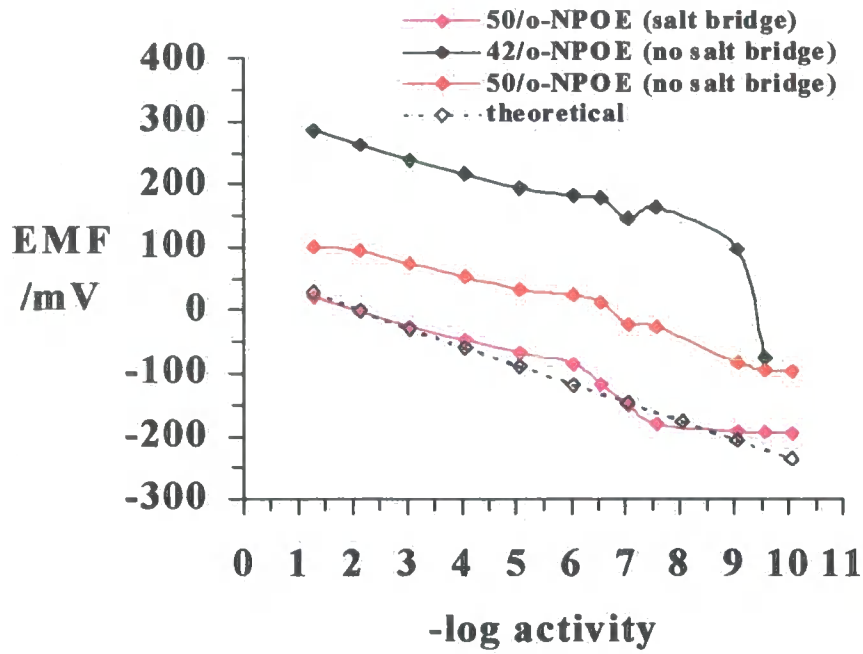

Figure 2.23: Response of three Ca^{2+} ISEs incorporating either **50**, or ETH1001 **42** (298 K).

Although a decrease in the lower detection limit was displayed by all three ISEs, the actual values were difficult to obtain according to existing IUPAC recommendations.[34] This is because the composition of the IFS influences the profile of the response function as well as the lower limit of detection. Throughout the measured activity range, the slope of the response was initially sub-Nernstian, then changed to super-Nernstian at more dilute activities (10^{-6}–10^{-8}). For the ISE (with 1 mol dm^{-3} KCl salt bridge) incorporating **50**/o-NPOE, this super-Nernstian response corresponds to a 100 mV change through this physiologically important range i.e. the concentration of intracellular Ca^{2+} is < $5x10^{-6}$ mol dm^{-3}. Conventionally, a Nernstian response is only displayed by ISEs when the composition of the membrane remains approximately stable to changes in the sample concentration.[35] However,the enhancement of lower limits of detection exploits ionic changes within the membrane. Sub-Nernstian behaviour has been observed in ISEs where the IFS was modified using metal ion buffers to reduce the detection limits.[31] The super-Nernstian behaviour is generated by changes in the ionic fluxes across the membrane, at dilute sample activities. Where the concentration of primary ions in the IFS is too low the depletion of primary ions from the sample solution into the membrane can be induced. This can result in a high ionic flux of primary ions towards the IFS, being generated within the membrane. Consequently a

super-Nernstian slope is observed at these critical dilute sample activities and therefore prevents the determination of detection limits at such low sample activities.[36] To neutralize this ion depletion and limit the associated ionic flux in the membrane, a decrease in the thickness of the aqueous Nernstian diffusion layer by means of vigorous stirring of the sample solution, or by using a flow-cell may be beneficial. Alternatively, lowering the concentration of ionic sites or increasing the thickness and/or viscosity of the membrane may be advantageous.[32]

2.7 Conclusion.

Electrode response studies using the PVC based membranes ISEs incorporating the substituted cis-cis-1,3,5-cyclohexanetriol ligands **49–51**, have demonstrated that they are poor ionophores for the detection of alkali and alkaline earth metals, with the exception of **50**, which displayed an excellent response towards Ca^{2+} in terms of the detection limit and slope factor.

On comparing these results with the oxa-amide *n*-butyl series, striking differences concerning trends in selectivity were observed, as were the overall response of the series of ligands towards the detection of the relevant cations. The major differences between the two cyclohexyl-amide series is the nature of the amide substitution being either n-butyl or isobutyl, in which the latter is more lipophilic and more sterically demanding. In previous work by *Gehrig et al,*[37] it was shown that 3,6-dioxaoctanediamide ionophores **52-54**, of extremely high lipophilicity can induce kinetic limitations in terms of ion transfer between the aqueous and membrane phase, which is reflected in the EMF of the ISE. Although, the ionophores studied by *Gehrig* differed extensively in the length of the amide N-alkyl chains, whereas the differences between amide substitution for the two related cyclohexyl series were by comparison less severe, it highlights another possible reason for non-Nernstian behavour - kinetic limitation of ion transport due to ligands of high lipophilicity.

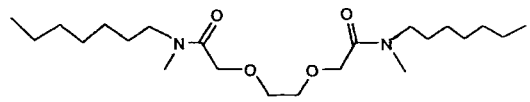

52

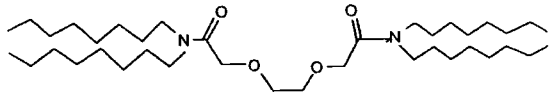

53

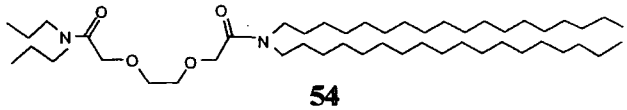

54

Figure 2.24: Structures of the series 3,6-dioxaoctanediamide ionophores **52-54** studied by *Gehrig*.

2.8 References for Chapter 2.

[1] Bishop M. L., Duben-Engelkirk J. L., Fody E. P., (Eds) in *Clinical Chemistry: Principles, Procedures, Correlations.* 2nd Edn., Lippincott J. B., Philadelphia, USA, 1992.

[2] Cattrall R. W., in *Chemical Sensors.* Oxford University Press, 1997.

[3] Buhlmann P., Pretsch E., Bakker E., *Chem. Rev.* **98**, 1593, 1998.

[4] Goodall M., *Ph.D. Thesis.* Durham. 1996.

[5] Diamond D., Nolan K., *Anal. Chem.* **73**, 22A, 2001.

[6] Sakaki T., Harada T., Deng G., Kawabata H., Kawahara Y., Shinkai S., *J. Inclusion Phenom. Mol. Recognit. Chem.* **14**, 285, 1992.

[7] Yamamoto H., Shinkai S., *Chem. Lett.* 1115, 1994.

[8] Bakker E., *Anal. Chem.* **69**, 1061, 1997.

[9] Kataky R., Nicholson P. E., Parker D., Covington A. K., *Analyst.* **116**, 135, 1991.

[10] Christian G. D., *Journal of Pharmaceutical and Biomedical Analysis.* **14**, 899, 1996.

[11] Kataky R., Nicholson P. E., Parker D., *J. Chem. Soc., Perkin Trans. 2,* 321, 1990.

[12] Faulkner S., Kataky R., Parker D., Teasdale A., *J. Chem. Soc., Perkin Trans. 2,* 1761, 1995.

[13] Metzger E., Ammann D., Asper R., Simon W., *Anal. Chem.* **58**, 132, 1986.

[14] Gadzekpo V. P. Y., Hungerford J. M., Kadry A. M., Ibrahim Y. A., Xie R. Y., Christian G. D., *Anal. Chem,* **58**, 1948, 1986.

[15] http://vm.cfsan.fda.gov/~frf/forum96/littlef.htm

[16] http://www.execpc.com/~cc/abstract.html

[17] Spichiger-Keller U. E., in *Chemical Sensors and Biosensors for Medical and Biological Applications.,* Weinheim, Wiley-VCH, Ch. 5. 1998.

[18] Suzuki K., Watanabe K., Matsumoto Y., Kobayashi M., Sato S., Siswanta D., Hisamoto H., *Anal. Chem.* **67**, 324, 1995.

[19] Goodall M., Kelly P. M., Parker D., Gloe K., Stephan H., *J. Chem. Soc., Perkin Trans. 2,* 59, 1997.

[20] Parker D., *Education in Chemistry.* 104, July 1998.

[21] Goodall M., Kelly P. M., Parker D., Gloe K., Stephan H., *J. Chem. Soc., Perkin Trans. 2,* 59,1997.

[22] Fiedler U., *Anal. Chim. Acta* **89**, 111, 1977.

[23] Armstrong R. D., Horvai G., *Electrochimica Acta* **35**, 1, 1990.

[24] Reany O., Blair S., Kataky R., Parker D., *J. Chem. Soc., Perkin Trans. 2,* 623, 2000.

[25] Bakker E., Buhlmann P., Pretsch E., *Chem. Rev.* **97**, 3083, 1997.

[26] *Methodology and Clinical Applications of ISE.* **9**, Proceedings of an International Symposium on the Measurement of Blood Electrolytes.

[27] Bailey P. L., *Analysis with Ion Selective Electrodes.* 2nd Edn., Heyden and Son Ltd. London, 1980.

[28] Sokalski T., Ceresa A., Zwickl T., Pretsch E., *J. Am. Chem. Soc.,* **119**, 11347, 1997.

[29] Mathison S., Bakker E., *Anal. Chem.* **70**, 303, 1998.

[30] Schefer E., Ammann D., Pretsch E., Oesch U., Simon W., *Anal. Chem.* **58**, 2282, 1986.

[31] Sokalski T., Ceresa A., Fibbioli M., Zwickl T., Bakker E., Pretsch E., *Anal. Chem.* **71**, 1210, 1999.

[32] Ceresa A., Sokalski T., Pretsch E., *Journal of Electroanalytical Chemistry.* **501**, 70, 2001.

[33] Sokalski T., Zwickl T., Bakker E., Pretsch E., *Anal. Chem.* **71**, 1204, 1999.

[34] Buck R. P., Lindner E., *Pure Appl. Chem.* **66**, 2527, 1994.
[35] Bakker E., Meyerhoff M. E., *Anal. Chim. Acta.* **416**, 121, 2000.
[36] Gyurcsanyi R. E., Pergel E., Nagy R., Kapai I., Thi-Thu-Lan B., Toth K., *Anal. Chem.* **73**, 2104, 2001.
[37] Gehrig P., Morf W. E., Pretsch E., Welit M., Simon W., *Helv. Chim. Acta* **73**, 203, 1990.

Chapter 3

Sol-Gel Immobilised Lanthanide Complexes for Optical pH Sensing.

This chapter discusses the characterisation of the metal-based emission of europium and terbium complexes in sol-gel films for the purpose of optical pH sensing.

3.1 Introduction.

Two series of complexes are discussed in this chapter. They are grouped according to the nature of the sensitising chromophore. The first series constitutes substituted cyclen (12-N_4)-systems with tetra-amide or mono-amide tricarboxylate frameworks that incorporate a phenanthridine chromophore. The second series is based on para substituted aryl sulfonamide pendant groups that have been attached to a cyclen (12-N_4)-system with mono-amide tricarboxylate substitution. All complexes were synthesised in Durham. The former series was synthesised by Dr. Celine E Mathieu and Dr. Kanthi Senanayake, and the latter by Dr. Mark Lowe.

3.2 Photophysics of pH Responsive Lanthanide Complexes.

The photophysical characteristics of the lanthanide complexes that are discussed in this thesis may be described in terms of the photophysical process outlined in Figure 3.1.

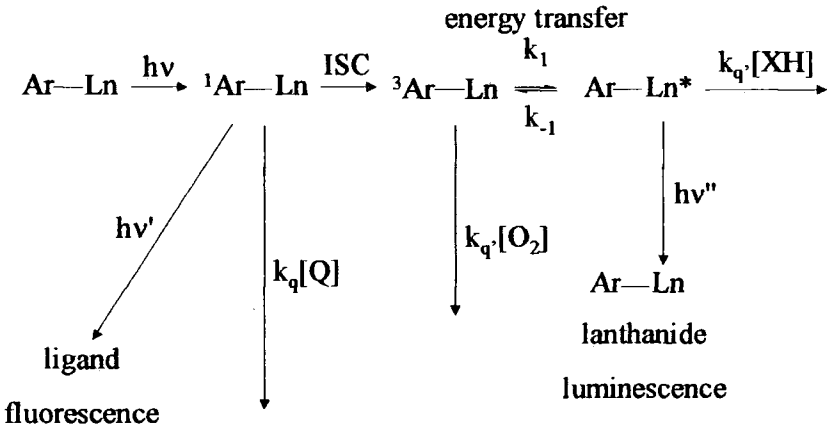

Figure 3.1: Photophysical scheme for responsive lanthanide complexes.

Considering the excited states of the lanthanide complexes only, protonation can modulate their luminescence in three ways. Protonation may reduce the energy of singlet and triplet states of the chromophore and can affect the rate of ISC from the excited singlet state to the excited triplet state. The Eu^{3+} ion can quench the fluorescence of proximate electron rich aryl singlet excited states via a photoinduced electron transfer process. Protonation has been shown to reduce this form of quenching.[1] The efficiency of intramolecular energy transfer to the emissive state of the lanthanide can also be affected following protonation as can the rate of thermally activated back energy transfer to the triplet state, which is commonly observed when the metal is Tb^{3+}. The emissive state of the lanthanide ion itself can also be quenched by processes that are pH dependent. In systems where the chelating ligand does not saturate the coordination number of the metal, then changes in pH can modulate the local coordination environment by controlling the metal ion hydration state. This in turn perturbs the extent of vibrational quenching of the emissive state via energy matched OH oscillators. Such processes have been reported for a range of lanthanide complexes in homogeneous solution.[2] This chapter is concerned with investigating the effect that sol-gel immobilisation has on the response of the pH dependent lanthanide luminescence. At the time of writing this thesis, this piece of work describes the first examples of sol-gel immobilised emissive lanthanide complexes where the pH dependent metal-based luminescence is reported from single component systems.

3.3 Lanthanide Complexes Incorporating a Phenanthridine Chromophore.

Lanthanide complexes based on a 1,4,7,10-tetraazacyclododecane (cyclen) framework substituted with mono-amide tri-carboxylate groups **55-56**, or tetra-amide derivatives **57** and incorporating either a 6-butyl or unsubstituted phenanthridine chromophore, are shown in Figure 3.2. Each complex has displayed a well-defined pH dependent behaviour in homogenous solution.[1,2,3,4]

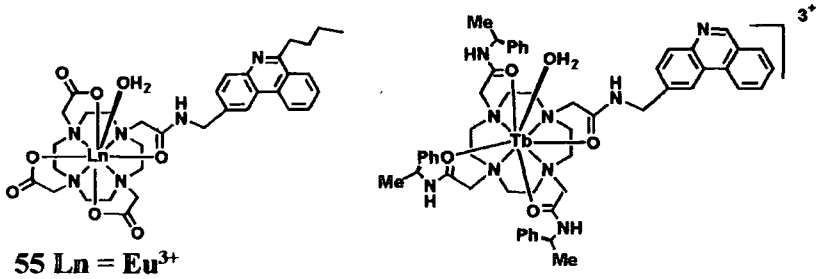

55 Ln = Eu^{3+}

56 Ln = Tb^{3+}

57

Figure 3.2: pH responsive lanthanide complexes **55-57** incorporating a phenanthridine chromophore.

The phenanthridine chromophore can be excited at wavelengths greater than 350 nm. This is an attractive feature as it reduces background autofluorescence from excited biological matrices and also allows the possibility of coupling the sensing species with optical waveguides. Changes in pH modulate the absorbance and fluorescent properties of phenanthridine. The butyl group at the 6-position enhances the protonation constant of the phenanthridine nitrogen, through a positive inductive effect. Singlet and triplet excited state energies and apparent protonation constants for phenanthradine, 6 butyl phenanthradine, **55** and **57** are given in Table 1.[5]

Compound or complex	E singlet cm^{-1}		E triplet cm^{-1}		$pK_a S_0$ (±0.1)	$pK_a S_1$ (±0.1)
	neutral	acidic	neutral	acidic		
phenanthridine	28200	26300	22000	21300	3.4	3.6
6-butyl-phen*	28600	26600	21600	21000	4.6	5
55	28800	27300	21700	21100	5.4	5.6
57	28700	27000	22000	21300	3.3	3.4

pK_a values determined in 0.1 mol dm^{-3} NMe_4NO_3 or *0.1 mol dm^{-3} NMe_4NO_3 in 5:1, v/v MeOH/H_2O observing changes in λ_{abs} = 365 nm or λ_{em} = 405 nm.

Table 1: Apparent protonation constants and singlet and triplet energies.

The effect of pH on the absorption spectrum of **55** in homogeneous solution is shown in Figure 3.3.

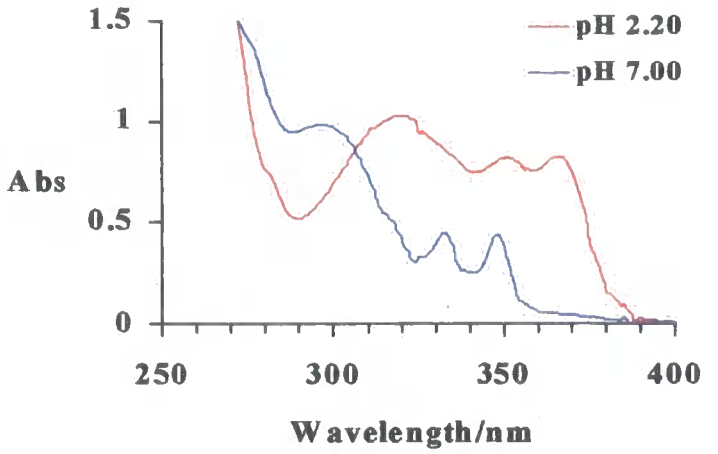

Figure 3.3: UV-vis absorbance spectrum of **55** in homogeneous solution. Solution was basified by the addition of 1 mol dm^{-3} NaOH and titrated to acidic pH using small aliquots (typically 0.5 μL) of either 1 mol dm^{-3} or 0.1 mol dm^{-3} HCl, I = 0.1 mol dm^{-3} NaCl, 295 K.

Following protonation of the 6-butylphenanthridine moiety the energy of the singlet state was lowered by 2500 cm^{-1} resulting in noticable hyperchromism and also a bathochromic shift of approximately 30 nm. Therefore the phenanthridinium species can be selectively excited at wavelengths greater than 350 nm i.e. 365 nm, which also corresponds to the wavelength of certain UV-LEDs. Excitation wavelengths that correspond to LEDs are another pre-requisite of optical transducers for the purpose of optical chemical sensing as LEDs are commercially available, cost effective, portable and easily miniaturised.

3.3.1 Sol-Gel Immobilised 6-Butyl-phenanthridine Europium (III) Monoamide Tricarboxylate.

A sol-gel film encapsulating complex **55** was prepared with an R-value of 2 (R = molar ratio of water/silica) according to Section 5.2.3. Following a stabilisation period of 28 days, the film was free from mechanical defects as deduced by inspection with a microscope. Prior to initial characterisation, the film was placed in aliquots of water, over 5 days, to allow any non-immobilised complex to wash out. No apparent leaching was observed when monitoring the fluorescence of the water following excitation at 365 nm. The characteristic europium emission spectrum for the sol-gel film, one month after spin-coating is shown in Figure 3.4.

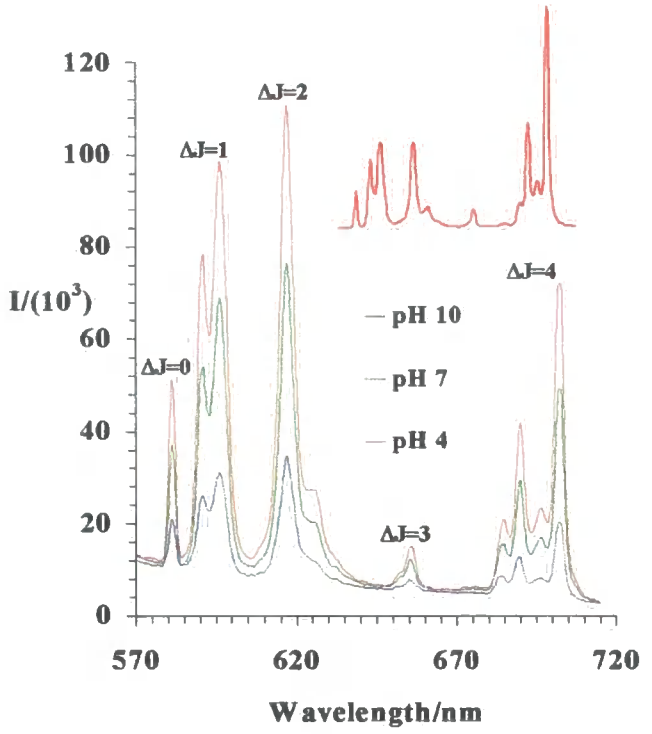

Figure 3.4: pH dependent luminescence of **55** in sol-gel film. λ_{ex} = 365 nm, I = 0.1 mol dm^{-3} NaCl, 295 K, flow-cell A. (*inset;* **55** in solution, pH 4, λ_{ex} = 365 nm, 295 K, I = 0.1 mol dm^{-3} NaCl)

Following excitation at 365 nm the luminescent metal-based emission of the complex was preserved, in that the red europium emission was switched on and there was no change in the spectral shape following protonation. Following changes from pH 4 to pH 10, there was approximately a 3-fold enhancement in intensity. This enhancement relates almost entirely to the pH dependence of the absorption properties of the chromophore and the associated suppression of photoinduced electron transfer from the excited singlet state of the chromophore following protonation, as the phenanthridinium species is less readily oxidised compared to the neutral species. On comparison with the emission spectrum obtained in solution, there is a slight but noticeable difference in the relative intensity of the $\Delta J = 4$ manifold. Characterisation of the film over a period of three months revealed no significant changes in the pH response curve as can be seen in Figure 3.5. The film was stored in dry dark conditions at 295 K, in-between measurements.

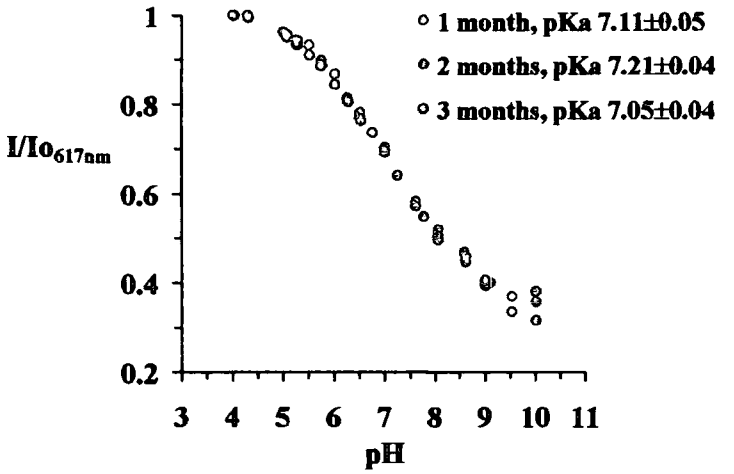

Figure 3.5: Comparison of reproducible pH response profiles for film doped with **55**, λ_{ex} = 365 nm, I = 0.1 mol dm^{-3} NaCl, 295 K, flow-cell A.

Following immobilisation in the ionic sol-gel matrix 90% of the total signal change was observed over 3.5 pH units, with a linear response being observed between pH 5.5 and 8. This extension of the linear range following immobilisation can be attributed to the micro-heterogeneous nature of the sol-gel, which exerts numerous ionic environments on the chromophore. This results in a distribution in the free energy changes associated with the protonation-deprotonation equilibrium and an associated distribution of local pK_a values surrounding an apparent mean.

The intensity data based on experimental measurements were fitted to the equation shown in Appendix I (using a non-linear iterative least squares fitting procedure operating on Excel® software) to calculate the apparent protonation constants of the sol-gel immobilised complex. Four spectra were recorded for each pH value at intervals of approximately 5, 10, 15 and 20 minutes, following the changing of the buffer solution. This was to ensure the signal was stable over time and also to allow the calculation of experimental errors. The error quoted in the apparent pK_a is the standard deviation, based on the 4 data sets. (This error analysis was applied to all sol-gel films discussed in this piece of work).

Compared to homogeneous solution behaviour, the apparent pK_a of complex **55** in the sol-gel matrix was increased by approximately 1.6 pH units. This increase may be

attributed to electronic effects and the enhanced acidity within the sol-gel microenvironment. At neutral and high pH the sol-gel matrix is characterised by deprotonated silanol groups[6] and the shift in acidity constants is therefore influenced by the relative acidity of the microenvironment.

When observing the excitation spectrum of **55** in the sol-gel film there was a slight blue shift in the isosbestic wavelength from 304 nm in solution to 311 nm in the sol-gel matrix. As can be observed in Figure 3.6 the difference in intensity for the respective pH values is almost insignificant. At high pH the spectral band at 365 nm was only slightly less intense compared to the corresponding band at pH 4.5. The difference in excitation intensity for corresponding pH in homogeneous solution was > 20:1.[5] Again, this behaviour can be attributed to the inhomogeneous nature of the matrix and the associated non-specific interaction between the chromophore and the encapsulating matrix.

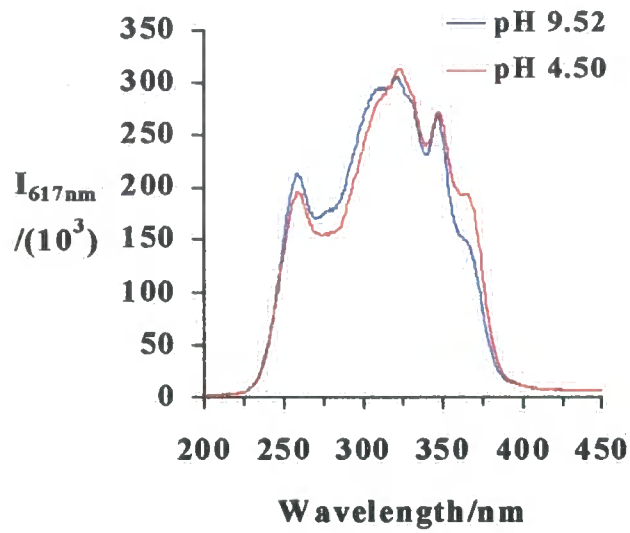

Figure 3.6: Excitation spectra of **55** in sol-gel film. I = 0.1 mol dm^{-3} NaCl, 295 K, flow-cell A.

The reversibility and response time of the thin film is shown in Figure 3.7. In the pH region associated with clinical measurements the sol-gel film was fully reversible with no apparent base-line drifting following changes in pH. The typical response times to obtain 95% of the signal change (t_{95}) between the pH range 5.5-8.5 was observed to be in the order of 80-90 s, which is relatively fast considering it takes 20 s to fill the flow-

cell. Such response times are consistent with reported values for acid catalysed sol-gel pH sensors.[7]

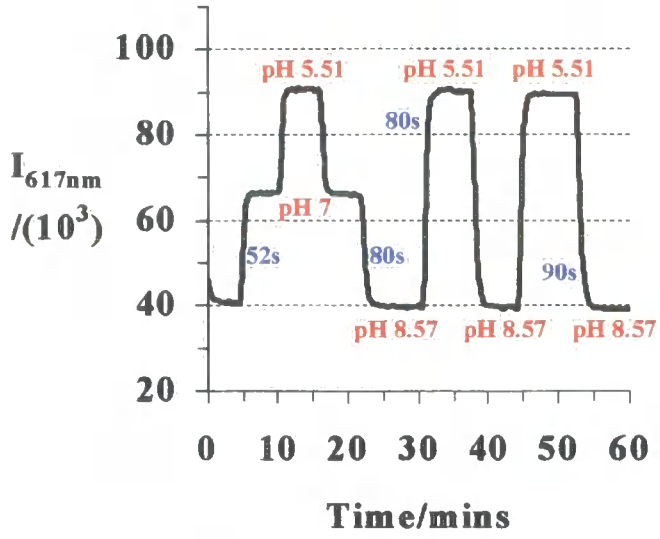

Figure 3.7: Response time and reversibility of **55** in sol-gel matrix. λ_{ex} = 365 nm, I = 0.1 mol dm^{-3} NaCl 298 K, flow-cell A.

3.3.2 Sol-Gel Immobilised 6-Butyl-phenanthidine Terbium Monoamide Tricarboxylate.

The corresponding terbium derivative **56** was doped in two films, with an R-value of 2 or 4 and molar ratios of TMOS:MeOH of 3.3 or 3 respectively. Following the stabilisation period of 28 days, both films displayed a smooth, transparent and defect-free appearance on inspection with a microscope. No apparent leaching of the complex was observed after being placed in water over 24 hours. The metal-based emission of both films mirrored the homogeneous solution behaviour in that in going from low to high pH the green terbium emission was switched on. Enhancements in signal intensity were approximately 40% and 60% for the films prepared with R-values of 4 and 2 respectively. The characteristic Tb^{3+} metal-based emission for the sol-gel film incorporating **56** (R = 4), following changes in pH is shown in Figure 3.8.

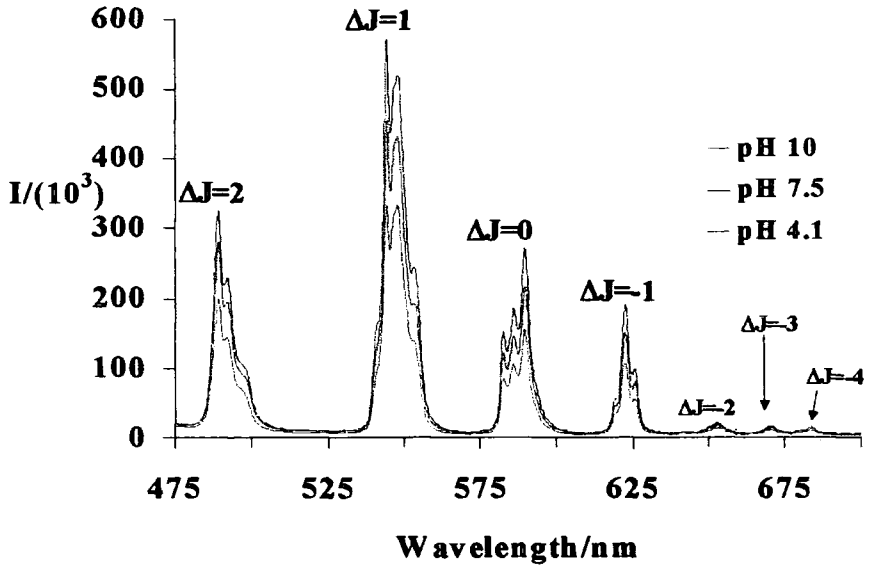

Figure 3.8: pH dependent luminescence of sol-gel film (R = 4) doped with **56**. λ_{ex} = 311 nm, I = 0.1 mol dm^{-3} NaCl, 295 K, flow-cell B.

When comparing Figure 3.8 with Figure 3.4 it is obvious that **56** displays different behaviour to the europium analogue. In the case of **56** a photo-equilibrium exists involving the excited triplet state of the phenanthridinium species and the emissive Tb^{3+} $^5D_4$ level. Under acidic conditions the phenanthridinium triplet is lowered to 600 cm^{-1} above the $^5D_4$ state. Such proximity of the two levels results in the competitive deactivation of the $^5D_4$ level through the process of thermally activated back energy transfer (BET).[1,5] This does not occur in the case of **55**, as the energy gap between the excited triplet state and the phenanthridinium species is ~ 4000 cm^{-1} and hence the energy gap between the emissive level of europium and the triplet state of the phenanthridinium species remains significantly large, preventing thermally activated back energy transfer.

The influence of the R-value on the apparent pKa value of the complex **56** was investigated. On comparing the O/Si ratio, which was varied from 2 to 4, apparent pKa values of 8.11±0.04 and 7.18±0.07 were observed respectively following characterisation 28 days after spin-coating. Lower R-values tend to be associated with incomplete hydrolysis of the TMOS precursor and therefore an increase in the number of silanol groups within the network. As discussed in Section 3.3.1, the enhancement of

immobilised pK_a values is governed by the relative acidity of the surrounding medium, where the most acidic environment results in the greatest enhancement of apparent pK_a.[8] Shifts in the apparent pK_a values for the sol-gel films doped with **56** one month after spin-coating are shown in Figure 3.9.

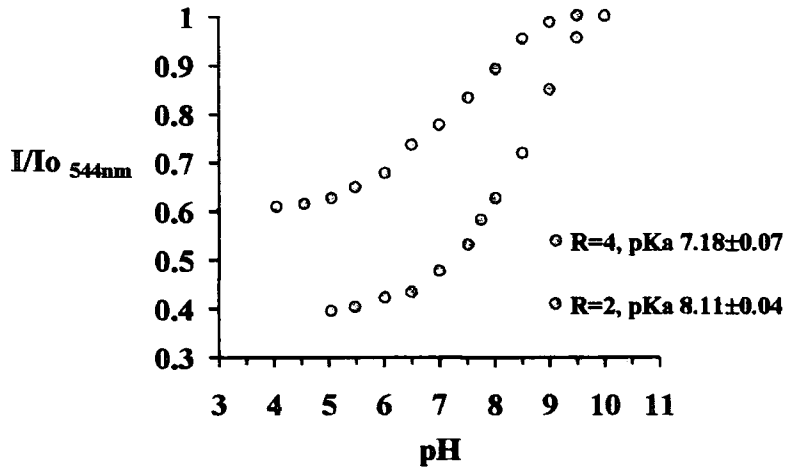

Figure 3.9: Comparison of apparent pK_a values for sol-gel films prepared with R-values of 2 or 4 incorporating **56**, λ_{ex} = 311 nm, I = 0.1 mol dm^{-3} NaCl, 295 K, flow-cell B.

Following changes in pH, 90% of the total signal change was observed over 2.5 and 3.5 pH units for the R = 2 and R = 4 films respectively. A slight increase in the apparent pK_a values were observed (pKa = 8.31±0.05; R = 2, pKa = 7.34±0.06; R = 4) following characterisation at three months after spin-coating. These changes in the apparent pK_a values may be attributed to ongoing structural changes within the sol-gel matrix, and have been reported in cases where the sol-gel films were stored in dry conditions between characterisation.[9]

3.3.3 Sol-Gel Immobilised Butyl-phenanthridine Terbium (III) Tetraamide.

The most direct commonly used optical sensing method is based on intensity changes of the indicator species in response to analyte recognition. This method can often be rather unreliable for a number of reasons. Changes in the local concentration of the indicator probe can occur through leaching from the encapsulating matrix and also there may be photobleaching effects. Such effects coupled with inherent fluctuations in the output

intensity of the spectrofluorimeter lamp source, can manifest in the output signal of the sensing matrix. Frequent sensor calibrations then become compulsory and can be time consuming. Therefore it is important that measurements are made that are independent of the concentration of the sensing complex.

Ratiometric probes change their spectral shape following analyte recognition and allow the concentration of the analyte to be determined from the ratio of intensities measured at either two excitation or emission wavelengths. This is desirable as these ratios are independent of the local concentration of the probe.

One example of ratiometric sensing was shown with complex **57**. Following immobilisation in a sol-gel film (R-value = 4), excitation spectra were observed (Figure 3.10), whose behaviour was more comparable with that displayed in homogeneous solution, compared to the neutral phenanthridine complexes **55-56**. When observing excitation spectra of the immobilised complex at pH 9.4, a small but noticeable band at 370 nm was apparent. This band, which is far less conspicuous than with the neutral complexes i.e. **55** in Figure 3.6, does not exist in the corresponding solution spectra at high pH and therefore can again be attributed to the inherent inhomogeneous nature of the sol-gel matrix.

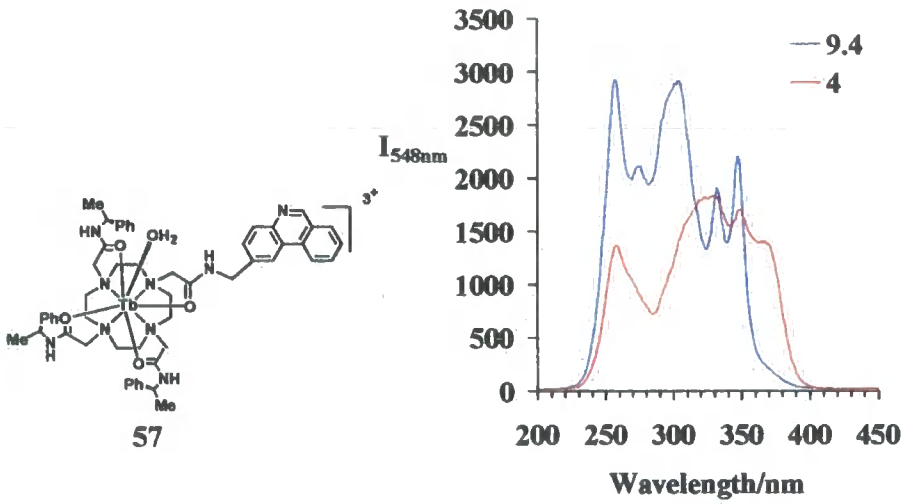

Figure 3.10: Excitation spectra of **57** in sol-gel film (R = 4). I = 0.1 mol dm^{-3} NaCl, 295 K, flow-cell A.

The slight blue shift in the isosbestic wavelength from 304 nm in solution to 311 nm in the sol-gel matrix was again apparent when observing the excitation spectrum of **57**. In plotting the ratio of intensities at the isosbestic wavelength 311 nm to the long tail wavelength 370 nm as a function of pH, an 8-fold enhancement in intensity was observed over the pH range 4 to 8. A 90% change of the total signal was observed over the pH range 6.5-9.5, thus covering the narrow physiological pH range 6.9 to 7.5. This can be observed in Figure 3.11.

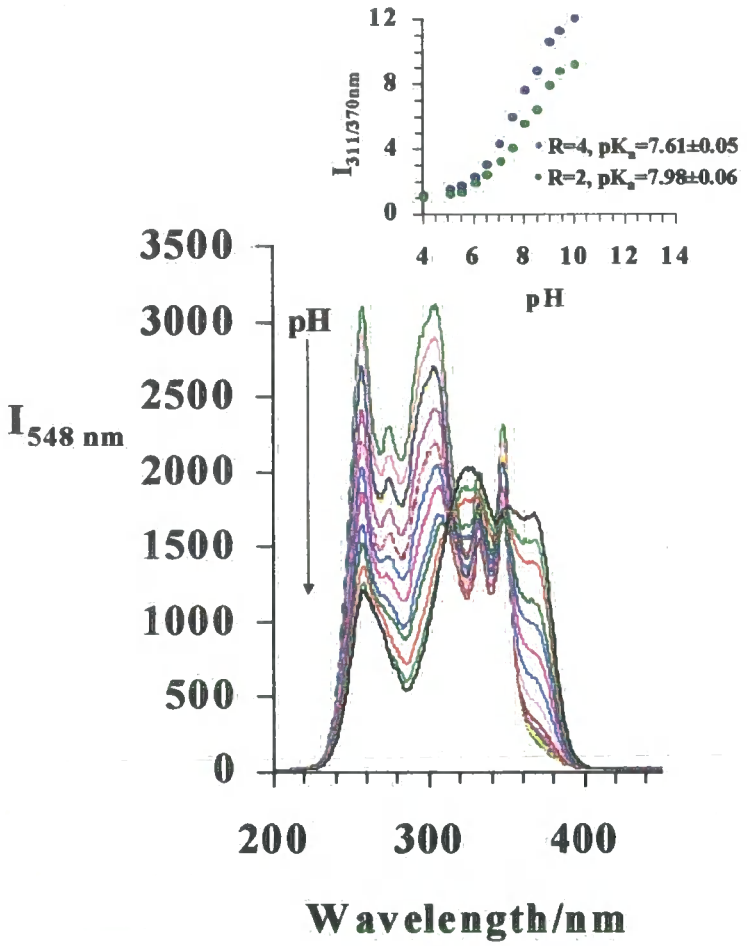

Figure 3.11: pH dependent excitation of **57** in sol-gel film (R = 4). λ_{em} = 548 nm, I = 0.1 mol dm^{-3} NaCl, 295 K, flow-cell B. (*inset:*comparison of the pH modulation of the excitation intensity ratio (λ = 311/λ = 370 nm) for sol-gel films (R-values of 2 or 4) incorporating **57**)

An apparent pK_a value of 7.61±0.05 was observed when monitoring the intensity ratio of λ = 311/λ = 370 nm for the R = 4 film (Figure 3.11;*inset*) This value is greater by approximately 1.9 pH units than the value in homogeneous solution. On comparison

with a sol-gel film incorporating **57**, and prepared with an R-value of 2, an apparent pK_a of 7.94±0.04 was observed when monitoring the same excitation wavelength intensity ratio ($\lambda = 311/\lambda = 370$ nm). As discussed in Sections 2.3.1 and 2.3.2, enhancements in the immobilised pKa values, when compared to the homogeneous solution value, are governed by the increase of the relative acidity of the sol-gel matrix, which can be influenced by the R-value of the film.

3.4 Terbium (III) Complexes Incorporating an Aryl Sulfonamide Chromophore.

pH responsive lanthanide complexes that incorporate a pendant arylsulfonamide chromophore with para-substituition of the aryl group are shown in Figure 3.12.

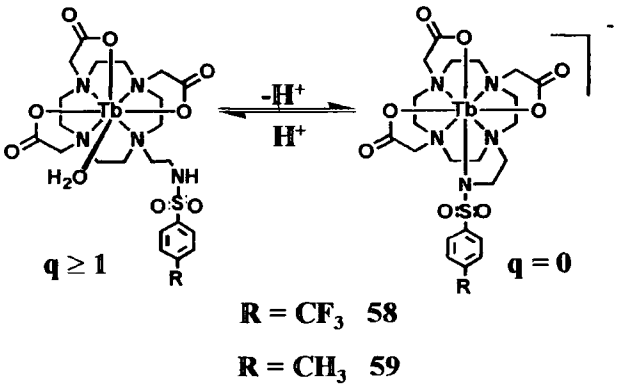

Figure 3.12: pH responsive lanthanide complexes incorporating an arylsulfonamide chromophore. (q = number of metal-bound H_2O molecules).

3.4.1 General Behaviour.

In homogeneous solution, variations in the pH gave rise to a switching behaviour of the hydration state of the metal associated with the on/off ligation of the sulfonamide group. The predominant enhancement in intensity in going from low to high pH occurs through the deprotonation of the arylsulfonamide group and the subsequent coordination of N to the metal centre. The direct coordination of the sulfonamide nitrogen brings the aryl chromophore closer to the Tb^{3+} ion, enhancing the rate of the intramolecular energy transfer process. Simultaneously, but to a lesser extent, the hydration state of the

terbium metal switches from an aqua species to a non-hydrated form. This reduces the associated vibrational quenching of the metal excited state via vibrational energy transfer to higher harmonics of energy matched OH oscillators.[10]

In homogeneous solution apparent protonation constants of 5.44±0.04 and 6.29±0.02 were calculated for **58** and **59** respectively. The value of these constants is determined by the electron withdrawing/donating inductive effect of the para-substituent of the aryl group. The pH dependent solution behaviour for each complex is shown in Figure 3.13.

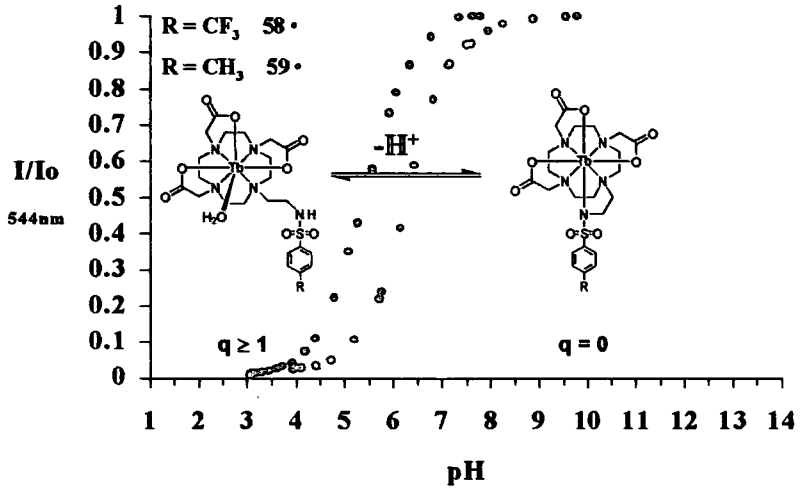

Figure 3.13: pH dependent luminescence of **58** • and **59** ◦ in solution. I = 0.1 mol dm^{-3} NaCl, λ_{ex} 265nm, 295 K.

3.4.2 Sol-Gel Immobilised Terbium (III) 1-[2'-(4-Trifluoromethylphenylsulfonylamino)ethyl]-4,7,10-tris(carboxymethyl)-1,4,7,10-tetraazacyclododecane.

Unlike the phenanthridine complexes those incorporating sulfonamide linkages are relatively acid sensitive. Therefore, they would probably not be so resistant to the harsh acidic conditions used to prepare the sol-gel films incorporating the **55-57** complexes. These conditions were required to fabricate sol-gels with small pore diameters to physically entrap the complexes within the silica cage-like structure. Despite efforts to prepare films incorporating **59**, using 0.01 mol dm^{-3} HCl as the catalyst, prolonged ageing times of 10 and 24 hours, and in some cases heating the sol to promote

polymerisation prior to spin-coating, the resultant thin films were prone to cracking, showed significant leaching of the complex and irreproducible pH dependent behaviour. Therefore thin films incorporating **58** and **59** were prepared with R-values of 3 or 4 using 0.04 mol dm^{-3} HCl as the catalyst and were doped with significantly higher concentrations (15 mmol dm^{-3}) of the sensing complex in order to obtain a relatively good signal. Following a stabilisation period, the film doped with **58** showed significant leaching over a period of one week, whereas the film incorporating **59** showed apparent leaching over two days only. This behaviour is not surprising as the latter film was prepared with an R-value of 4, aged for 7 hours prior to spin-coating and was subsequently left to stabilise for 28 days prior to characterisation compared to values of 3, 2 and 14 respectively for the film incorporating **58**. The poor conditions that were used for film **58** can simply be attributed to the fact that it was the first film prepared, and hence conditions such as the adequate ageing of the sol prior to spin-coating, coupled with significant stabilisation periods had not yet been optimised. Leaching effects for the sol-gel film incorporating **58** are shown in Figure 3.14.

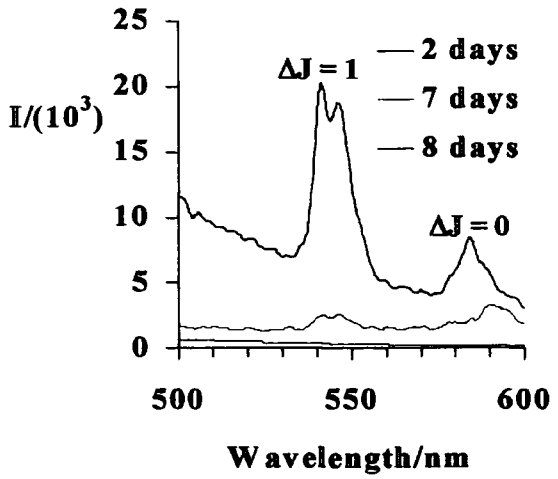

Figure 3.14: Evidence of leaching of the complex **58** from the sol-gel matrix over a period of one week λ_{ex} = 265nm, Ex and Em slits = 2.5 nm, 295 K.

Following immobilisation of **58** the sensing matrix exhibited a rather modest 30% enhancement in intensity in going from pH 4 to 10, of which 90 % of the total signal change covered the pH range 5.2 to 7.6. Such a reduction in the sensitivity of the species towards variation in pH when encapsulated in the sol-gel matrix may indicate

poor intramolecular dynamics of the complex following entrapment in the small pores of the silica network. Response times (t_{95}) obtained using alternating buffers of pH 5.56 and pH 7.75 were of the order of 120 s and 105 s on going from low to high then high to low pH respectively. The response showed marginal baseline drift and hysteresis on going from low to high pH. Such effects again may be attributed to sluggish complexation kinetics of the pendant arylsulfonamide group, or more likely leaching of the complex from the sol-gel film.

The apparent pK_a of the immobilised complex **58** was determined to be 6.47±0.05 following a stabilisation period of 14 days. This value was approximately 0.9 pH units greater than the protonation constant reported in homogeneous solution in the presence of a similar ionic strength (I = 0.1 mol dm^{-3} NaCl). Over time the protonation constant was found to shift slightly following characterisation at intervals of 2.5 and 4.5 months respectively. This observation may be consistent with structural changes occurring within the matrix as a consequence of the relatively short ageing period of the sol and subsequent short stabilisation period following spin-coating.[9] The pH dependent response curve for **58** is shown in Figure 3.15.

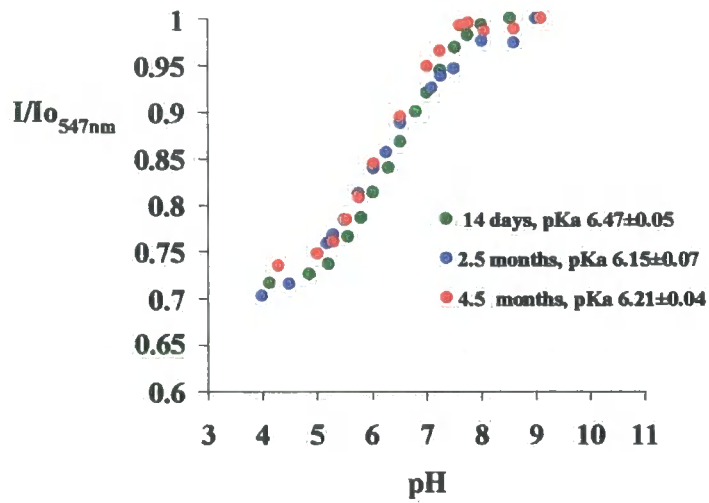

Figure 3.15: Comparison of pH response of sol-gel film incorporating **58** over time. λ_{ex} 265 nm, I = 0.1 mol dm^{-3} NaCl, 295 K, flow-cell B,

The effect of ionic strength on the apparent pK_a, and of anionic interferences on the spectral response of the complex **58** in the sol-gel film was briefly investigated

following the stabilisation period of 14 days. (Figure 3.16). The pH response using a series of buffers prepared with an ionic strength of 20 mmol dm^{-3} NaCl showed an apparent pK_a of 6.75±0.06. This slight shift is thought to be consistent with the reduced stabilisation of the negative charge of the bound form at the lower ionic strength.

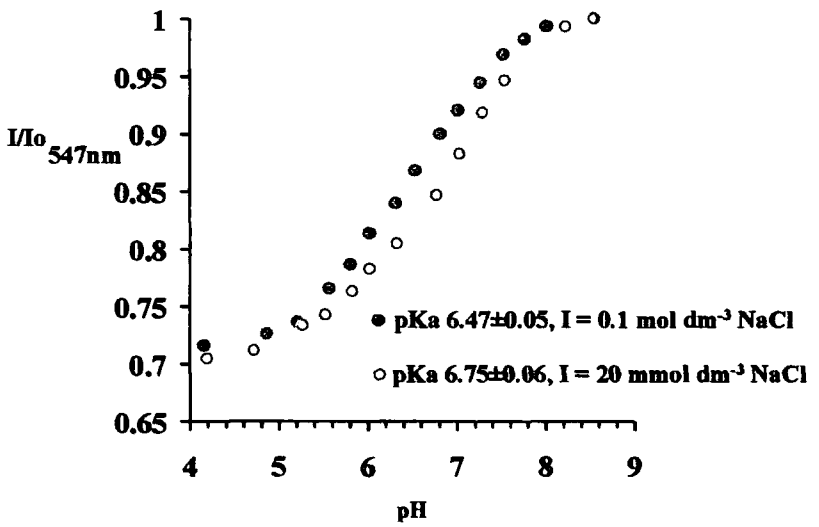

Figure 3.16: Influence of ionic strength on the apparent protonation constant for **58** in a sol-gel film. λ_{ex} = 265 nm, 295 K, flow-cell A.

Potential interfering species such as the biologically relevant anions; HCO_3^-, HPO_4^{2-}, lactate and citrate, can competitively bind to the metal ion and alter the metal based emission. To investigate whether such anionic interferents were able to permeate the sol-gel matrix and coordinate to the coodinatively 'unsaturated' terbium metal centre, the spectral response was compared in alternating backgrounds at pH 7.4 containing either 0.1 mol dm^{-3} NaCl or a simulated anionic clinical background. No significant changes in the intensity of the spectral response was observed with respect to all electrolytes present, indicating the absence of anionic binding to the terbium metal centre. At pH values greater than that of the isoelectric point of the silanol groups (~ pH 2–4 depending on the extent of polymerisation), the matrix is densely packed with negatively charged deprotonated silanol groups. Therefore electronic repulsion coupled with any steric hindrance that may be associated with the bulkiness of the anions and the small pore size of the sol-gel, may prevent the anions entering the porous network.

The effects of the presence of anionic interfering species can be observed in Figure 3.17.

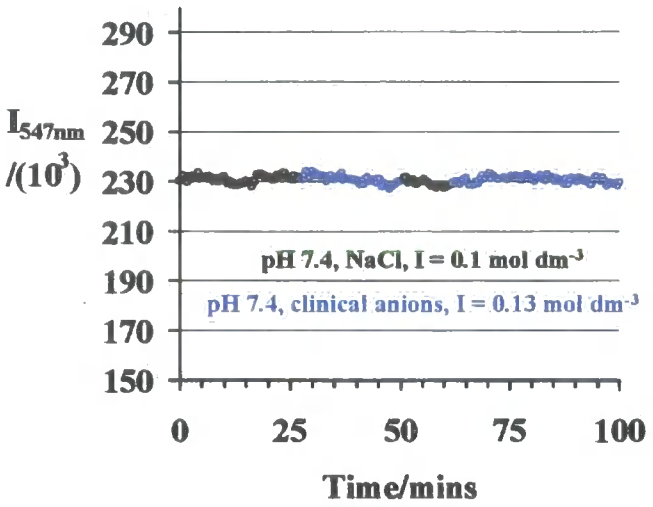

Figure 3.17: Influence of clinical anions (30 mmol dm^{-3} $NaHCO_3$, 2.3 mmol dm^{-3} Na lactate, 0.9 mmol dm^{-3} NaH_2PO_4, 0.123 mmol dm^{-3} Na citrate, 0.1 mol dm^{-3} NaCl) on the spectral intensity for **58** in a sol-gel film. λ_{ex} = 265 nm, 295 K, flow-cell A.

3.4.3 Sol-Gel Immobilised Terbium (III) 1-[2'-(4-Methylphenylsulfonylamino)ethyl]-4,7,10-tris(carboxymethyl)-1,4,7,10-tetraazacyclododecane.

A second example of a ratiometric sensing film was observed following immobilisation of the para-methyl arylsulfonamide analogue **59**. Changes in the spectral shape of the hypersensitive $\Delta J = 1$ band centred around 540–550 nm accompanied changes in the pH. From plotting the ratio of intensities of the two components of $\Delta J = 1$ transition as a function of pH (Figure 3.18), an approximate 20% signal change was observed over the pH range 5 to 7.5. The apparent pK_a value was found to be 7.03±0.08, allowing the working range of the sensing matrix to coincide with the physiological pH range.

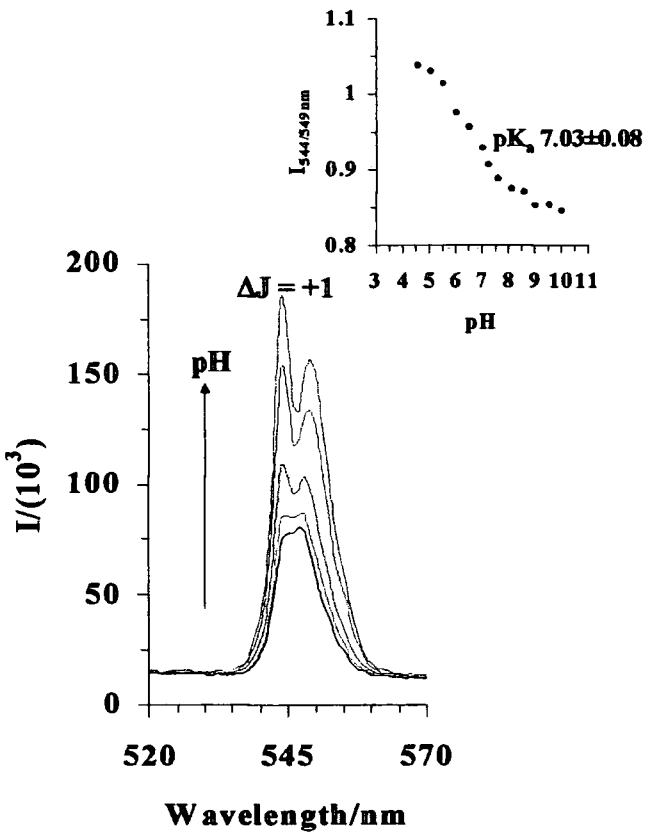

Figure 3.18: Expansion of ΔJ = 1 band for **59** in sol-gel film, and plot of intensity ratio ($I_{544/549\,nm}$) of the two ΔJ = 1 components as a function of pH, λ_{ex} 265 nm, I = 0.1 mol dm^{-3} NaCl, 298 K, flow-cell B.

Alternatively, an approximate 100% change in emission intensity was observed when monitoring the pH dependent intensity changes at 544 nm only (Figure 3.19). In this case 90% of the total signal change covered approximately 3.5 pH units. An apparent pK_a of 7.46±0.09 was observed one month following spin-coating. This value decreased slightly over a further two-month period. This may again be consistent with ongoing structural changes occurring within the matrix during this period. Again, all pK_a values were enhanced following immobilisation in the sol-gel media approximately 0.7-1 pH units, compared to homogeneous solution studies.

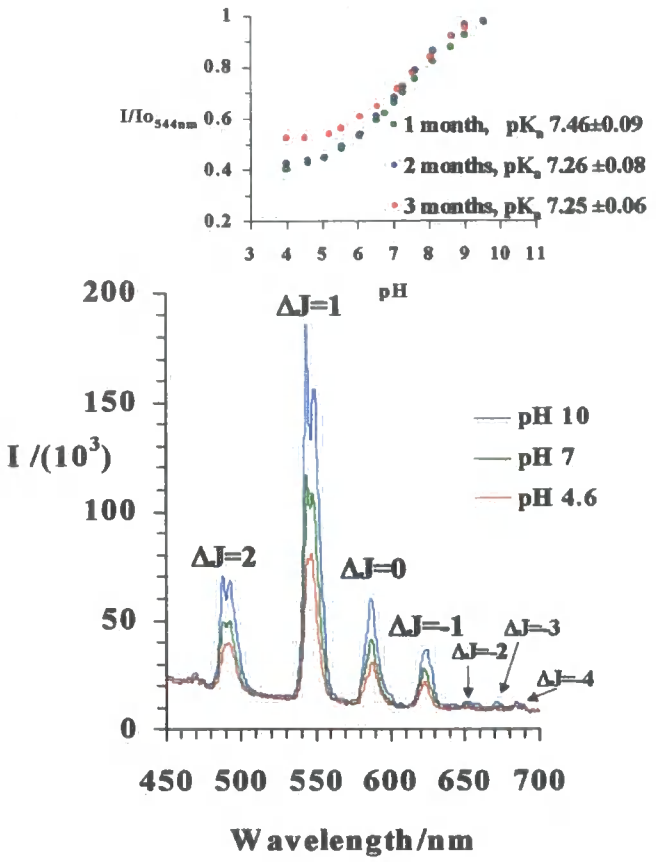

Figure 3.19: pH dependent luminescence of **59** in a sol-gel film. λ_{ex} = 265 nm, I = 0.1 mol dm^{-3} NaCl, 295 K, flow-cell B. (*inset;* pH response curve)

The sol-gel film encapsulating **59** was fully reversible to changes in pH that covered the quasi-linear working range (pH 5.52 to 8.62). Response times in this pH region were relatively fast and of the order of 100–110 s.

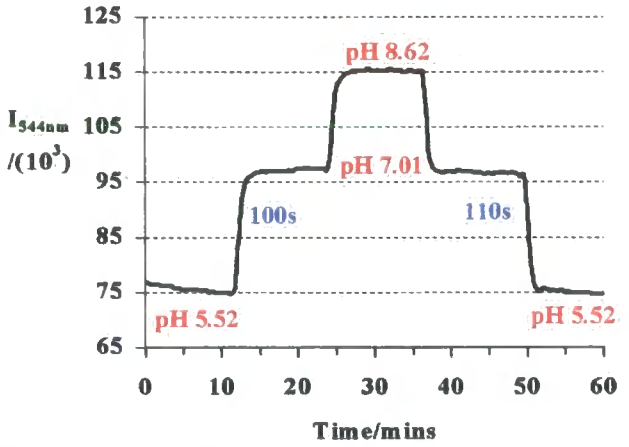

Figure 1: Response time and reversibility of **59** in a sol-gel matrix, λ_{ex} 265 nm, I = 0.1 mol dm^{-3} NaCl, 298 K, flow-cell A.

3.4.4 Sol-Gel Immobilised Europium (III) 1-[2'-(6-Cyanophenanthridinyl-2-sulfonylamino)ethyl]-4,7,10-tris(carboxymethyl)-1,4,7,10-tetraazacyclodecane.

The alternative chromophore, 6-cyanophenanthridine, was incorporated into an identical system in which the pH dependent europium metal-based emission was directly related to the enhanced intramolecular energy transfer from the N-bound sulfonamide form and the associated displacement of ligated water from the metal centre. The solution behaviour of **60** has been documented.[5]

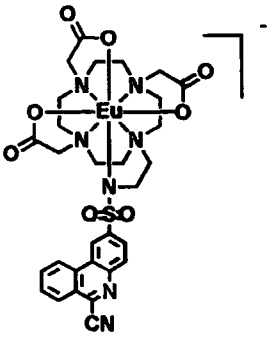

60

Figure 3.20: pH responsive fluorescent Eu^{3+} complex **60** incorporating the 6-cyanophenanthridinyl-2- sulfonylamino chromophore.

Compared to the previously discussed terbium analogues, substitution of the arylsulfonamide chromophore for the 6-cyanophenanthridinyl-2- sulfonylamino group allowed longer excitation wavelengths to be used. Following immobilisation in the sol-gel, (R = 4), the excitation spectra showed an 80% enhancement in intensity in going from pH 4 to 10 (Figure 3.21).

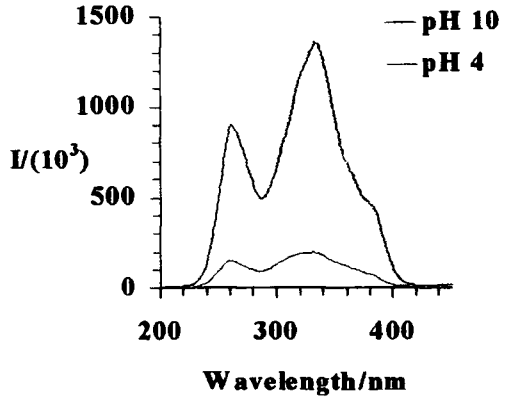

Figure 3.21: Excitation spectra of **60** in sol-gel matrix. λ_{em} = 615 nm, I = 0.1 mol dm^{-3} NaCl, 298 K, flow-cell B.

Similar intensity-based changes were observed in the pH dependent metal based emission spectra shown in Figure 3.22.

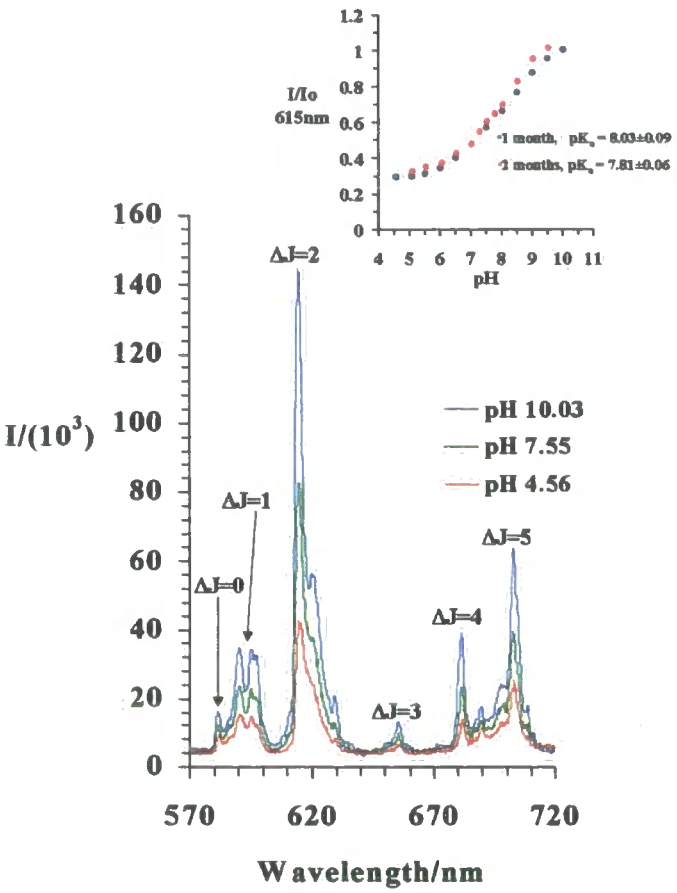

Figure 3.22: pH dependent luminescence of **60** in a sol-gel film. λ_{ex} 330 nm, I = 0.1 mol dm^{-3} NaCl, 295 K, flow-cell B. (*inset*:pH response curves • 1 month, • 2 months)

When plotting the emission of the hypersensitive ΔJ = 2 transition as a function of pH (Figure 3.22:*inset*), 90% of the total signal change occurred between pH 6 and 9 and an apparent pK$_a$ of 8.03±0.09 was observed following characterisation 1 month after spin-coating. This was ~ 2 pH units greater to that calculated in homogeneous solution of a similar ionic strength. This apparent pK$_a$ value was found to be relatively stable (pK$_a$ = 7.81±0.06) following characterisation at a two-month period after spin-coating.

The response of the film incorporating **60** was fully reversible between pH 6.5 and 8, with response times (t_{95}) typical of 100 s being observed. However, the film displayed

significant drifting if subjected to pH > 9 for an extended period of time. This effect could be attributed to basic hydrolysis of the 6-cyano group to the corresponding amide.

3.5 Conclusion.

A series of luminescent europium and terbium complexes have been immobilised in acid catalysed sol-gel films. Characterisation of these immobilised complexes as chemical transducers for the purpose of optical pH sensing, focused on the comparison of their pH-dependent luminescent behaviour to previous studies in homogenous solution. The sensing films were also characterised in terms of stability, response times, reversible sensing behaviour and reproducibility of the pH response following storage over significant periods of time. Examples of intensity and ratiometric sensing films have been defined.

All sol-gel films displayed well-defined pH-dependent luminescent behaviour. Their response times were of about 100 s, which is comparable to reported response times for pH sensing acid catalysed sol-gel films. The sensing films appeared to be relatively robust in terms of photobleaching and complex leaching effects. Enhanced apparent protonation constants of the complexes were observed following sol-gel immobilisation, when compared with values reported for homogeneous solution studies. This effect is thought to be due to the enhanced local acidity of the sol-gel medium, which can be influenced by the R-value of the film,

3.6 References for Chapter 3.

[1] Clarkson I. M., Beeby A., Bruce J. I., Govenlock L. J., Lowe M. P., Mathieu C. E., Parker D., Senanayake K., *New J. Chem.*, **24**, 377, 2000.
[2] Parker D., *Coordination Chemistry Reviews.* **205**, 109, 2000.
[3] Parker D., Senanayake P. K., Williams J. A. G., *J. Chem. Soc., Perkin Trans. 2*, 2129, 1998.
[4] Mathieu C., *Ph.D. Thesis.* Durham. 2001.
[5] Blair S., Lowe M. P., Mathieu C. E., Parker D., Senanayake P. K., Kataky R., *Inorganic Chemistry.* Accepted for publication, 2001.
[6] Malins C., Glever H. G., Keyes T. E., Vos J. G., Dressick W. J., MacCraith B. D., *Sensors and Actuators B.* **67**, 89, 2000.
[7] Lobnik A., Majcen N., Niederreiter K., Uray G., *Sensors and Actuators B.* **74**, 200, 2001.
[8] Baker M. E. J., Narayanaswamy R., *Sensors and Actuators B.* **29**, 368, 1995.
[9] Lobnik a., Oehme I., Murkovic I., Wolfbeis O. S., *Anal. Chim. Acta* **367**, 159, 1998.
[10] Lowe M. P., Parker D., *Chem. Commun.*, 707, 2000.

Chapter 4

Sol-Gel Immobilised Lanthanide Complexes for Optical Dissolved Oxygen Sensing.

This chapter discusses the characterisation of the metal-emission and intensity decay profiles of terbium complexes in sol-gel films for the purpose of optical dissolved oxygen sensing.

4.1 Quenching.

Fluorescence quenching concerns molecular processes that diminish the intensity of an emitting species. Such processes include excited state reactions, molecular rearrangements, energy transfer, dynamic (collisional) and static quenching. For collisional quenching to occur, the quenching species must diffuse to the fluorophore and make molecular contact during the lifetime of the excited state of the fluorophore.[1]

4.2 Quenching by Molecular Oxygen.

Molecular oxygen is an ubiquitous collisional quencher. This diatomic molecule possess a triplet ground state termed $^3\Sigma$ and two low lying singlet states termed $^1\Delta$ and $^1\Sigma$, of which the former possesses the lower energy. $^3O_2$ can quench both S_1 and T_1 states of organic fluorophores via chemical or physical processes such as electron transfer or energy transfer respectively.[2]

$$\textbf{Fluorophore}^* + {}^3O_2\,(^3\Sigma) \longrightarrow \textbf{Fluorophore} + {}^1O_2\,(^1\Delta)$$

Figure 4.1: Schematic representation of triplet oxygen quenching of an excited organic fluorophore to generate singlet oxygen.

4.3 The Stern-Volmer Equation and Deviations.

Quenching is described by the Stern-Volmer equation. In homogeneous media each luminescent species usually experiences the same microenvironment on an average time scale.[3] This generally results in single-component exponential decay behaviour, where the intensity and lifetime forms of the Stern-Volmer equation[4] are represented by Equations 4.1-4.3.

$$\frac{\tau_o}{\tau} = 1 + K_{sv}[Q] \qquad \textbf{Equ 4.1}$$

$$K_{sv} = k_2 \tau_o \qquad \textbf{Equ 4.2}$$

$$\frac{I_o}{I} = 1 + (K_{sv} + K_{eq})[Q] + K_{eq} K_{sv} [Q]^2 \qquad \textbf{Equ 4.3}$$

τ lifetime of luminescent species.

I intensity of luminescent species.

K_{sv} Stern-Volmer constant.

Q concentration of quencher.

k_2 bimolecular quenching constant.

K_{eq} association constant for binding of quencher to luminescence species.

o denotes the absence of quencher.

The efficacy of the quencher or the accessibility of the fluorophore to the quencher is revealed by k_2. This bimolecular quenching constant can in turn be explained in terms of the solubility coefficient (α) and diffusion coefficient (D) of the quencher in the environment of the fluorophore, i.e. $k_2 = \alpha D$. Equation 4.3, considers the possibility of both dynamic and static *(formation of a non luminescent complex)* quenching. Quenching data is usually presented as plots of I_o / I or τ_o / τ vs. [Q] where the ratio of both the intensities and lifetimes of the luminescent species in the absence/presence of Q are expected to be linearly dependent on the concentration of Q with an intercept of 1 on the y-axis and a slope equal to K_{SV}. The Stern-Volmer constant is quoted in the form of $K_{SV}^{-1} = Q$, where Q is the concentration of the quencher required to quench 50 % of the intensity I_o. Where plots of I_o / I or τ_o / τ vs [Q] are linear then the quenching process

is considered purely collisional i.e. $K_{eq} = 0$ in Equation 4.3. Conversely if the plot of I_o/I lies above τ_o/τ, then static quenching is thought to be a contributing factor. Linear Stern-Volmer plots are also indicative of a single luminescent species with complete accessibility to the quencher.[1]

In cases where quenching occurs in a solid matrix, the severe micro-heterogeneity that is commonly associated with sol-gel films often results in non-linear intensity Stern-Volmer plots. The observed, characteristic downward curvature is the result of numerous quenching microenvironments being experienced by the entrapped luminescent species.[1,5,6,7] Luminescent lifetime decays often display multi-exponential behaviour as a result of such micro-heterogeneous systems. In these circumstances the simple homogeneous model is inadequate and analysis using Equation 4.1 and 4.3 is prohibited.[6] Therefore, the lack of comprehensive information concerning the micro-heterogeneity precludes the true determination of quenching mechanisms for entrapped luminescent species and consequently makes it extremely difficult to fit quenching data reliably to verifiable models that bear chemical significance to reality.

4.4 Oxygen Sensitive Terbium Complexes.

The Tb^{3+} complexes **61-62,** have been shown to respond to changes in dissolved oxygen concentration. They are based on substituted cyclen (12-N_4)-systems with tetra-amide or mono-amide triphosphinate frameworks that incorporate an N-methylated phenanthridine chromophore. Both complexes were synthesised at Durham University by Dr. Kanthi Senanayake and Dr. Gareth Williams.

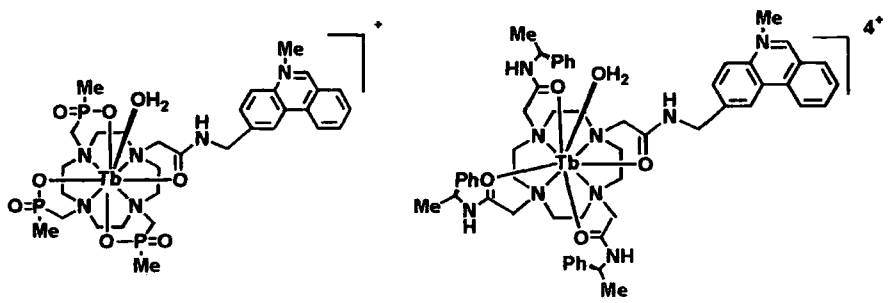

61 **62**

Figure 4.2: Structure of oxygen responsive Tb^{3+} complexes **61-62.**

The metal-based emission of the Tb^{3+} complexes **61-62** as a function of molecular oxygen (pO_2), has been previously investigated in homogeneous solution.[8,9] Linear Stern-Volmer plots were observed for both complexes, and changes in the Tb^{3+} emission lifetime in the presence and absence of oxygen were observed. Both complexes displayed immunity towards variations in pH in the range 2-9. Stern-Volmer constants and lifetimes are shown in Table 4.1.

Compound	K_{SV}^{-1}/Torr *	τ/ms (no O_2) **	τ/ms (O_2) **
61	45	0.83	0.1
62	58	0.94	0.09

* λ_{exc} = 370 nm, λ_{em} = 545 nm, I = 0.1 mol dm^{-3} NMe_4ClO_4. ** Measurements made over dissolved oxygen concentration♦ range 0-0.3 mmol dm^{-3}.[10]

Table 4.1: Stern-Volmer constants and lifetimes for oxygen sensitive Tb^{3+} complexes **61-62.**

4.5 Analysis of Lifetime Data for Calibration Purposes.

Lifetime data generated for the oxygen sensitive films incorporating complexes **61** and **62** was treated using the following assumptions to allow the experimental data to be compared among data sets. I would like to acknowledge Dr. Darren Noble, University of Durham for his assistance with the data treatment.

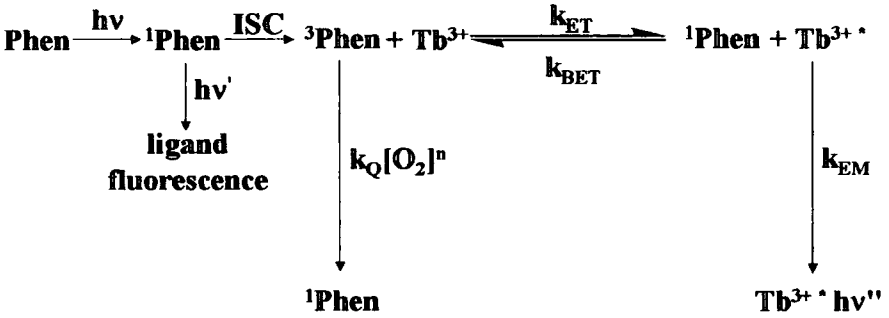

Figure 4.3: Schematic representation of photo-physical system for oxygen responsive Tb^{3+} complexes. (T = triplet state of antenna, k_{ET} = rate of forward energy transfer process, k_{BET} = rate of thermally activated back energy transfer process, k_Q = rate of oxygen quenching process, k_{EM} = rate of emission process, Tb* = $^5D_4$ emissive state of Tb^{3+}).

♦ *Solubility of oxygen in H_2O at 293.15 K and 1 atm (≅ 760 torr):* partial pressure = 705 mm Hg, $[O_2]$ = 8.7 mg dm^{-3} (≅ 0.27 mmol dm^{-3}). *(Solubility of oxygen in H_2O depends upon pressure, temperature and concentration of dissolved electrolytes).*

In an attempt to fit the lifetime intensity data to appropriate kinetic models, it was found that by fitting such data to a first order process no change in the rate with changing oxygen concentration was noted. It was found that the data may be rationalised by making assumptions that k_{BET} is negligible, (i.e. $k_{BET} << k_{EM}$). Therefore, the fraction of ^{3}Phen that was quenched by energy transfer to the $^5D_4$ emissive level of Tb^{3+} could be described by Equation 4.4.

$$\frac{k_{ET}}{\left(k_{ET} + k_Q[O_2]^n\right)} = \frac{I_t}{I_t^O} \qquad \textbf{Equ 4.4}$$

k_{ET} rate of forward energy transfer process.

k_Q rate of quenching process.

I_t intensity at time t.

o denotes in absence of quencher.

The ratio I_t/I^o_t was replaced by R and this was substituted into Equation 4.4, which was rearranged to give Equation 4.5.

$$k_{ET} = R\left(k_{ET} + k_Q[O_2]^n\right) \qquad \textbf{Equ 4.5}$$

Further rearrangements were made to give Equations 4.6 and 4.7:

$$k_{ET}(1-R) = Rk_Q[O_2]^n \qquad \textbf{Equ 4.6}$$

$$\left(\frac{1-R}{R}\right) = \left(\frac{k_Q}{k_{ET}}\right)[O_2]^n \qquad \textbf{Equ 4.7}$$

Taking the logarithm of both sides of Equation 4.7:

$$\log\left(\frac{1-R}{R}\right) = \log\left(\frac{k_Q}{k_{ET}}\right) + n\log[O_2] \qquad \textbf{Equ 4.8}$$

An example of the data analysis is given, for complex **61,** following immobilisation in a sol-gel film based on the raw data generated from lifetime decay measurements in the presence of varying dissolved oxygen concentration

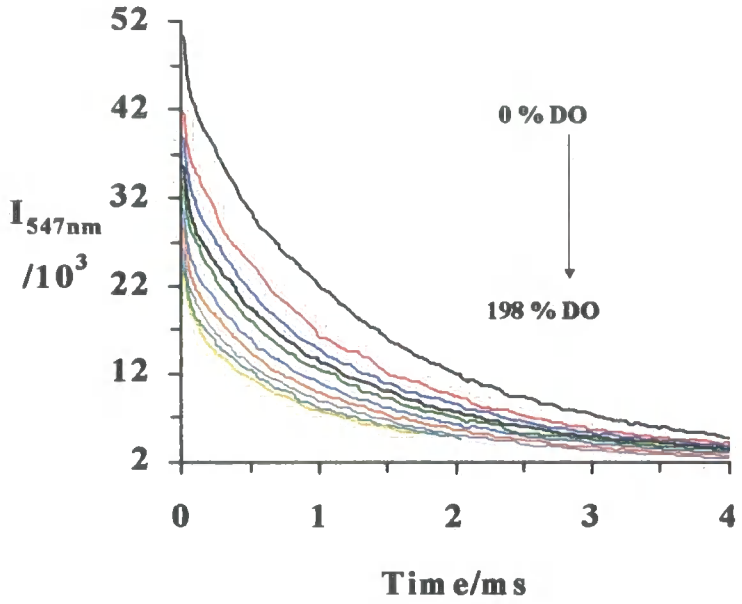

Figure 4.4: Lifetime decay measurements for **61** in sol-gel film (R = 2), illustrating the influence of the % of dissolved oxygen. λ_{ex} = 330 nm, λ_{em} = 547 nm, delay increment = 0.05 ms, 295 K.

The spectral data shown in Figure 4.4, was treated according to Equation 4.8. Plotting $\log\left(\frac{1-R}{R}\right)$ versus $\log[O_2]$, for each time interval gave a straight line of gradient 0.48 (± 0.01). This value varied depending on time t but in a random scattered fashion as observed in Table 4.2. The data highlighted in red was used to determine the mean value.

Data Generated from Double Log plot		
Time/ms	**Gradient**	**Intercept**
0.01	0.45	1.5
0.06	0.48	1.7
0.11	0.49	1.7
0.16	0.5	1.8
0.21	0.5	1.8
0.26	0.49	1.8
0.31	0.47	1.7
0.36	0.48	1.7
0.41	0.49	1.8
0.46	0.48	1.8
0.51	0.48	1.8
0.56	0.49	1.8
0.61	0.48	1.8
0.66	0.47	1.8
0.71	0.47	1.8
$\bar{X}$	0.48	1.77
σ_x	0.01	0.05

Table 4.2: Data generated from 61 in sol-gel film. (log(1-R)/R) vs log[O_2] was plotted for each time delay increment).

The apparent order in [O_2] was found to be 0.5, (n=0.5). Therefore by plotting $\left(\frac{1-R}{R}\right)$ versus $\sqrt{O_2}$, a linear dependence in oxygen quenching was displayed and the sensitivity of the film was denoted by the gradient. Figure 4.5 depicts such a plot, in which the % of dissolved oxygen has been expressed as concentration (mmol dm^{-3}) based on the assumption that the solubility of oxygen in distilled water at 760 mm Hg, 295 K and 100% relative humidity is 0.27 mmol dm^{-3} or 8.74 mg dm^{-3}.[11]

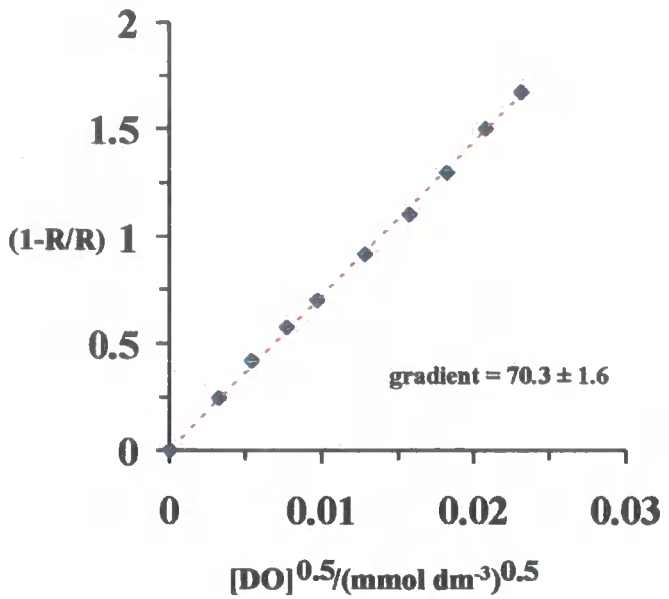

Figure 4.5: Linear dependence in oxygen quenching for **61** in sol-gel film (R = 2) following data analysis. (0.26 ms ≤ t ≥ 0.56 ms), 295 K, λ_{ex} = 330 nm, λ_{em} = 547 nm.

Time/ms	Gradient	Intercept	R^2
0.01	48.58	0.0269	0.9979
0.06	55.74	0.0114	0.9995
0.11	60.09	0.0032	0.9968
0.16	63.36	0.0041	0.9983
0.21	66.39	0.0036	0.9984
0.26	68.45	0.0064	0.9969
0.31	67.85	0.0135	0.998
0.36	69.91	0.002	0.9978
0.41	71.15	0.001	0.9977
0.46	71.07	0.0095	0.9991
0.51	71.65	0.0143	0.9984
0.56	71.64	0.0058	0.9989
0.61	73.86	0.0129	0.9985
0.66	76.62	0.0151	0.9989
0.71	74.12	0.0152	0.9992
$\bar{x}$	70.3	0.008	0.998
σ_x	1.6	0.005	0.001

Table 4.3: Data generated from **61** in sol-gel film. ((1-R)/R) vs $[O_2]^{0.5}$ was plotted for each time delay increment).

These plots were used purely for calibration and comparison purposes between data sets. In terms of a typical collisional quenching mechanism, this observed oxygen dependence does not seem to have a physical reality, at present, and is more likely to be associated with the effective quenching process in the sol-gel film.

4.6 Results and Discussion.

Details of sol-gel film preparation, ageing and stabilisation times as well as the experimental procedures used and instrumental parameter settings are given in Sections 5.27 and 5.28 respectively. It should also be noted that the error in DO measurement when using the DO probe was ± 1 % DO.[12]

4.6.1 Sol-Gel Immobilised N-Methylated Phenanthridine Mono-amide Triphosphinate Terbium (III) Complex.

Following a stabilisation period of 126 days the metal excited state lifetime decay and metal-based emission of the thin film (R = 2) incorporating complex **61** was measured as a function of oxygen concentration. Linearisation of the metal lifetime decay data according to Section 4.5 is shown in Figure 4.6.

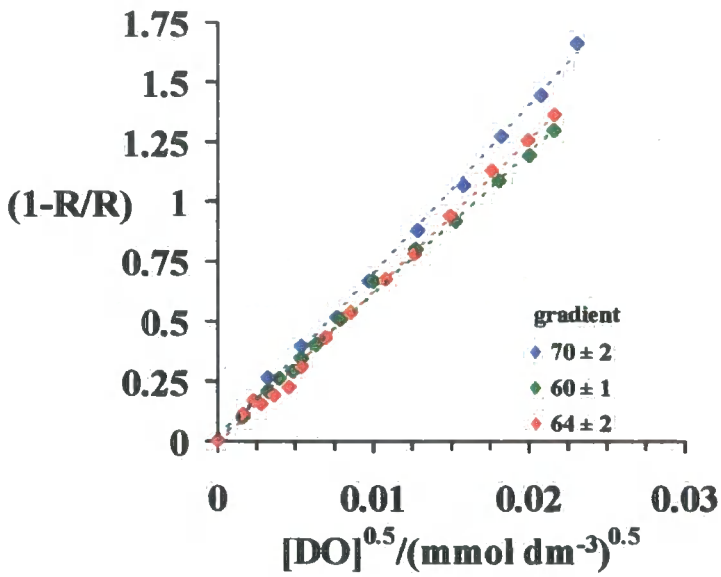

Figure 4.6: Linear dependence in oxygen quenching for **61** in sol-gel film (R = 2) compared over a 5 month period; ♦ March, ♦ April ♦ July, (0.26 ms ≤ t ≥ 0.56 ms), 295 K, λ_{ex} = 330 nm, λ_{em} = 547 nm.

Linearisation of data is desirable as it simplifies calibration and facilitates the comparison of data sets. Good reproducibility and a reasonable stability in its response to DO quenching was displayed by the sol-gel film, as defined by the randomness of the slight variation of the gradients of the calibration plots displayed in Figure 4.6. In general, the sensing film exhibited a modest sensitivity towards oxygen measurement. This modest responsiveness was displayed when observing the Stern-Volmer plot of the metal-based emission data, as shown in Figure 4.7.

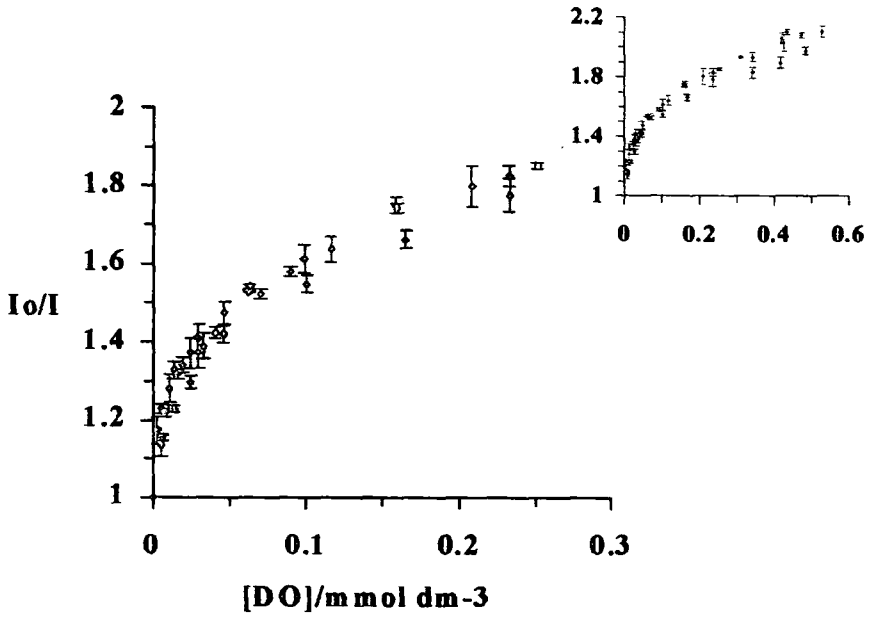

Figure 4.7: Oxygen quenching for **61** in sol-gel film (R = 2) compared over 5 month period; ◇ March, ◇ April ◇ July, 295 K, λ_{ex} 330 nm, λ_{em} 547 nm. (*inset*; Full oxygen range measured).

Curved plots were observed with significant deviation towards the x-axis at low DO oxygen concentrations i.e. < 0.1 mmol dm^{-3} (~ 3.2 ppm). Again the film displayed reasonable reproducibility towards oxygen sensing over the 5 month characterisation period.

4.6.2 Sol-Gel Immobilised N-Methylated Phenanthridine Tetra-amide Terbium (III) Complex.

An enhanced sensitivity was observed following sol-gel immobilisation of the tetra amide complex **62.** This is not surprising as this analogue also displayed enhanced

oxygen sensitivity in homogeneous solution, compared to the triphosphinate derivative **61** (Table 4.1). Linearisation of the lifetime decay data allowed the response of the film to be compared, following characterisation over a 3 month period. The film displayed good sensitivity towards oxygen quenching and excellent reproducibility was observed during this time.

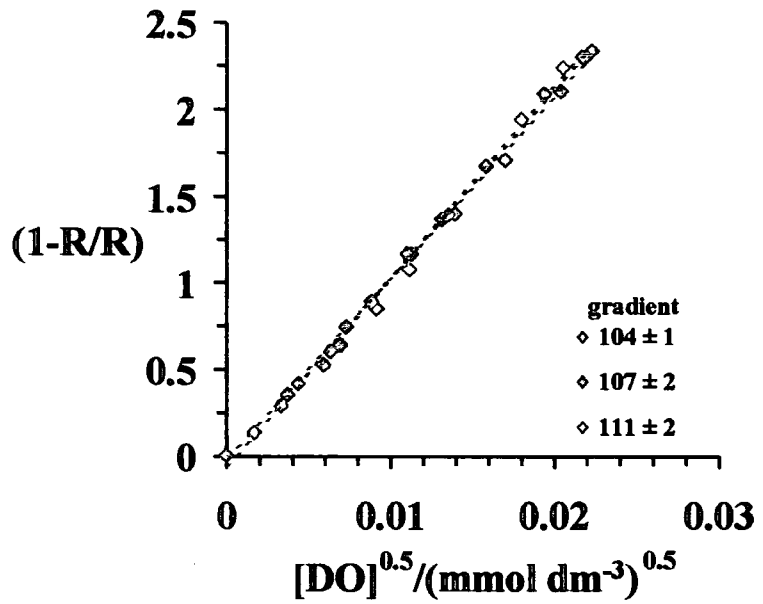

Figure 4.8: Linear dependence in oxygen quenching for **62** in sol-gel film (R = 2) compared over 5 month period; ◇ March, ◇ April ◇ July, (0.41 ms ≤ t ≥ 0.71 ms), 295 K, λ_{ex} = 330 nm, λ_{em} = 547 nm.

When observing the corresponding plots of the metal-based emission as a function of DO (Figure 4.9), this film displayed pronounced sensitivity at low DO concentrations i.e. ≤ 0.1 mmol dm^{-3} DO or ≤ 3.2 ppm, where the film's response was linear. At higher concentrations the response was less steep and curved.

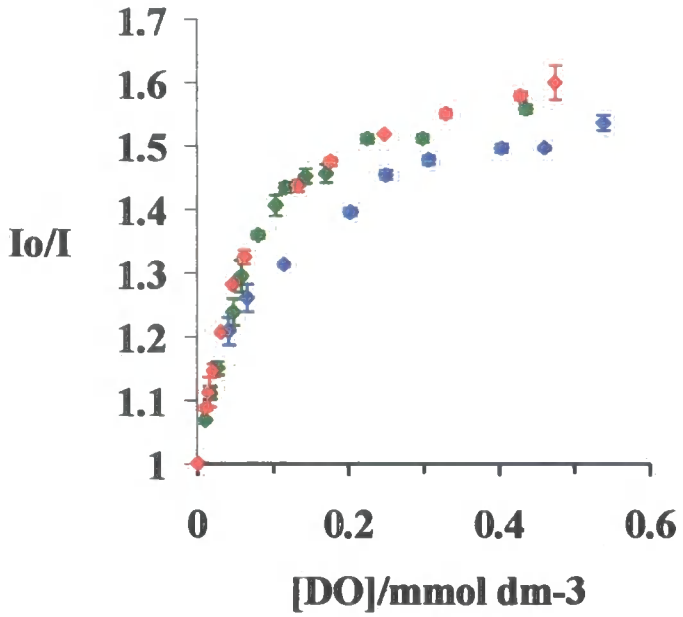

Figure 4.9: Oxygen quenching for 62 in sol-gel film (R = 2) compared over 3 month period; ♦ February, ♦ March ♦ April, 295 K, λ_{ex} 330 nm, λ_{em} 547 nm.

Enhanced oxygen sensitivity in sol-gel films prepared with low R-values has been reported by *McDonagh et al*,[7] for both gas and aqueous phase sensing. Comparing films prepared with an R-value of 2 or 4, enhanced quenching was observed at low oxygen concentrations with the R = 2 film, whereas an increasing linearity of response was found with the higher R-value. Indeed, a similar trend in quenching response and R-value tailoring was observed by comparing the R = 2 film encapsulating **62** (Figure 4.9), with one doped with the same sensing complex and prepared with an R-value of 4 (Figure 4.10).

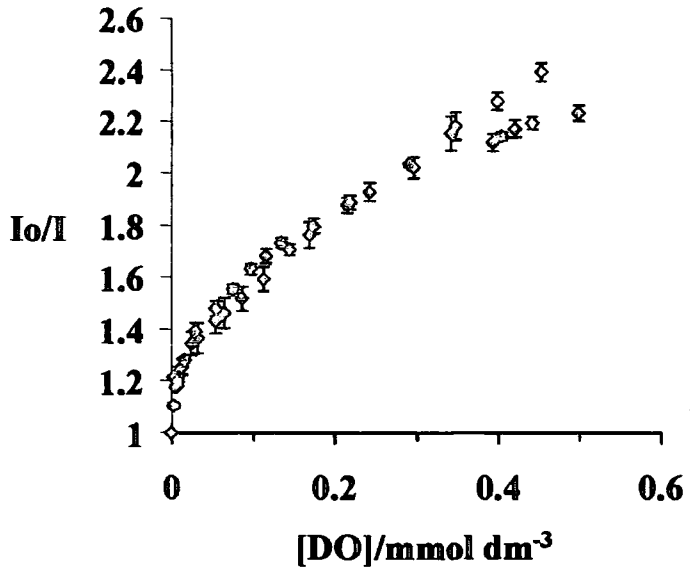

Figure 4.10: Oxygen quenching for **62** in sol-gel film (R = 4) compared over a 2 month period; ◊ May, ◊ July, 295 K, λ_{ex} 330 nm, λ_{em} 547 nm.

A gradual linear response across the oxygen concentration range was observed when the R-value was 4. This behaviour can be tentatively attributed to a reduced oxygen diffusion coefficient that is associated with the smaller average pore size for R = 4 compared to R = 2 films. Despite the slight deviation from linearity at high oxygen concentration observed for the May response; which can be associated with the difficulty in controlling high DO concentrations during the time of measurement, the response was fairly reproducible following characterisation over a 2 month period. This reproducibility was also displayed by the corresponding lifetime experiments. Following treatment of the lifetime-decay data, enhanced sensitivity towards DO quenching was observed for the R = 4 sol-gel film (Figure 4.11) incorporating the cationic complex **62**, when compared to the previous films (R = 2, **62** and R = 2, **61**). This is most simply observed in the gradient.

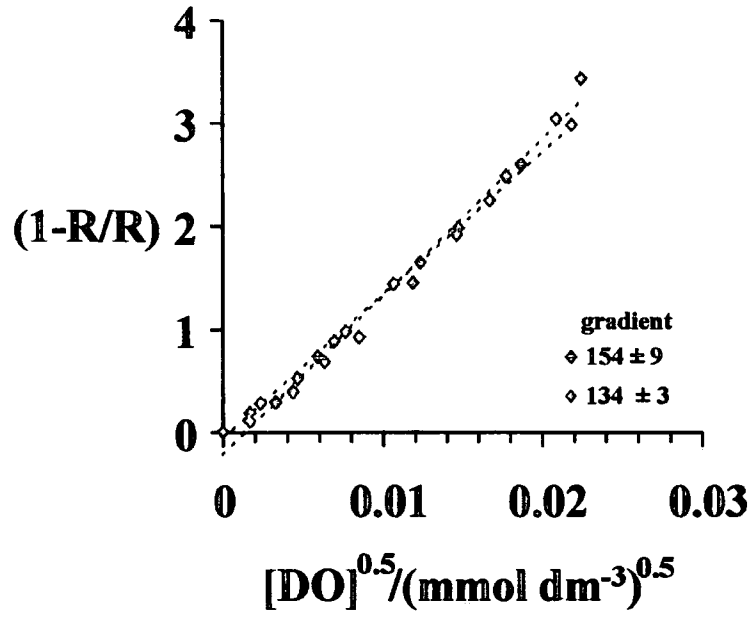

Figure 4.11: Linear dependence in oxygen quenching for **62** in sol-gel film (R = 4) compared over a 2 month period; ◇ May, ◇ July, (0.62 ms ≤ t ≥ 1.03 ms), 295 K, λ_{ex} = 330 nm, λ_{em} = 547 nm.

4.7 Conclusion.

Initial investigations concerning the fabrication and characterisation of sol-gel immobilised oxygen responsive Tb^{3+} complexes have been discussed. Despite the inherent complex decay kinetics of the terbium species, and the complexity associated with site heterogeneity, an adequate data treatment of the lifetime-decay curves has been found that allows a reasonable comparison amongst data sets for the same and different films. The sol-gel film prepared with an R-value of 4 and incorporating the tetra amide analogue **62** displayed superior sensitivity towards oxygen quenching at oxygen concentrations that can be detrimental to aquatic habitats, ie. ≤ 0.1 mmol dm^{-3} (3.2 ppm). All films showed good reproducibility over significant lengths of time.

The complexity associated with matrix heterogeneity was also apparent in intensity quenching data. In the literature a simple 2-site model has commonly been adopted for fitting purposes in treating the data associated with collisional quenching systems[5,3,13,14,15]. This model assumes that two populations of the emitting species exist in different environments within the matrix and the populations have different

accessibility to molecular oxygen. However a reasonable fit using this model does not mean it is physically correct, especially given the complexity of related lifetime decay data associated with heterogeneous media. If indeed the 2-site model is correct, then the lifetime contributions should 'correlate' with the parameters derived from intensity quenching data.[16] Significantly more complex models have also been reported for fitting lifetime and/or intensity Stern-Volmer plots and are based on the Gaussian 2-component model[6,17] and/or the log-Gaussian model,[17] in which the theory focuses on the assumption that there is a Gaussian distribution in K_{sv} resulting from a Gaussian distribution of microenvironments surrounding the lumiphore. However, whether they report chemical significance or are yet another fitting method remains controversial. For this reason such models including the simple 2-site model were not used in this study, and hence no parameters were generated from the respective calibration data.

However, observations concerning the relationship between the quenching response and the R-value of the films (encapsulating **62**) showed some similarity with the literature: pronounced sensitivity was observed at low oxygen concentrations with the R = 2 film. Conversely, a gradual linear response covering a wide oxygen range was apparent with the R = 4 film.

The nature of the experimental set-up, coupled with the difficulties encountered in maintaining high DO concentrations prevented reliable measurements concerning the response time and reversibility of the film. However, during the course of experiments focusing on the measurement of metal-based emission, all films showed reversible behaviour when the concentration of DO was returned to zero, except following subjection to significantly high concentrations i.e. >160 % DO. A more elaborate experimental set-up would be required to measure the response times of the films.

4.8 References for Chapter 4.

[1] Lakowicz J. R., *Principles of Fluorescence Spectroscopy.* 2nd Edn., Kluwer Academic/Plenum Publishers, New York, 1999.

[2] Turro N. J., *Modern Molecular Photochemistry.* University Science Books, California, 1991.

[3] Hartmann P., Leiner M. J. P., Lippitsch M. E., *Sensors and Actuators B.* **29**, 251, 1995.

[4] Sacksteder L., Demas J. N., DeGraff B. A., *Anal. Chem.* **65**, 3480, 1993.

[5] Xu W., Kneas K. A., Demas J. N., DeGraff B. A., *Anal. Chem.* **68**, 2605, 1996.

[6] Demas J. N., DeGraff B. A., *Sensors and Actuators B.* **11**, 35, 1993.

[7] McDonagh C., MacCraith B. D., McEvoy A. K., *Anal. Chem.* **70**, 45, 1998.

[8] Parker D., Senanayake P. K., Williams J. A. G., *J. Chem. Soc., Perkin Trans. 2,* 2129, 1998.

[9] Parker D., Williams J. A G., *Chem. Commun.*, 245, 1998.

[10] Parker D., *Coord. Chem. Revs.* **205**, 109, 2000.

[11] Mackereth, F. J. H., Heron, J., Talling, J. F., in *Water Analysis: Some Revised Methods for Liminologists.* Freshwater biological Association, Ambleside, UK, 1978, ch.2, pp. 29.

[12] Model 9150 Waterproof Dissolved Oxygen Meter Operating Manual. *Spectronic Analytical Instruments,* Leeds.

[13] Charlesworth J. M., *Sensors and Actuators B.* **22**, 1, 1994.

[14] Hendrick F., Donckt E. V., *Sensors and Actuators B.* **61**, 218, 1999.

[15] Carraway E. R., Demas J. N., DeGraff B. A., *Langmuir.* **7**, 2991, 1991.

[16] Carraway E. R., Demas J.N., DeGraff B.A., Bacon J. R., *Anal. Chem.* **63**, 337, 1991.

[17] Mills A., *Sensors and Actuators B.* **51**, 69, 1998.

Chapter 5

Experimental.

This chapter describes the experimental procedures and instrumental parameters used throughout this work. Brief descriptions of experimental techniques are also described.

5.1 Experimental for Chapter 2, Potentiometric Sensing.

5.1.1 Preparation of PVC Based Membranes.

The membrane components; poly(vinyl chloride) (PVC, high molecular weight), 2-nitrophenyl octyl ether (o-NPOE), bis(2-ethylhexyl)sebacate (DOS), and potassium tetrakis(4-chlorophenyl)borate (KTpClPB) were supplied by Fluka and are shown in Figure 5.1. The PVC based membrane incorporating ETH1001 **42** and o-NPOE, had previously been fabricated at Durham.

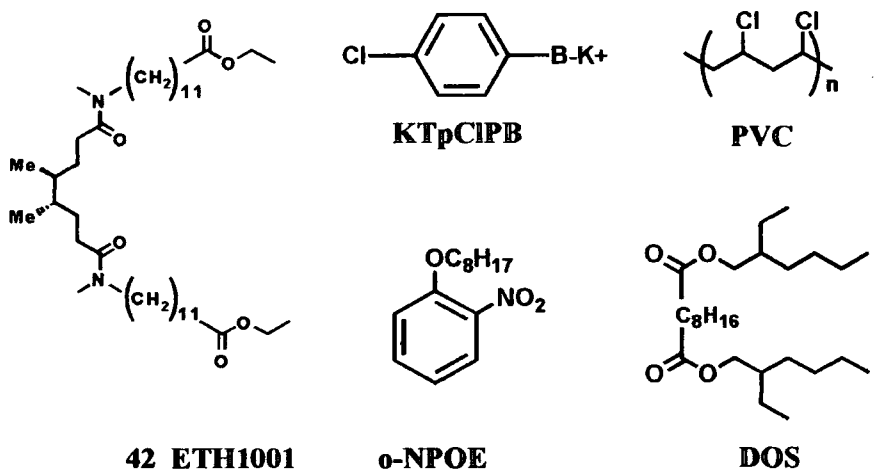

Figure 5.1: Membrane components.

Master membranes of approximately 200 μm thickness were prepared according to the composition,[1] 1.3% w/w ionophore, 65.6% w/w plasticizer, 32.8% w/w PVC and 0.5% w/w KTpClPB. For each ionophore two membranes were cast containing either DOS or o-NPOE plasticizer respectively. The membrane components were dissolved in 1.5 mL of freshly distilled tetrahydrofuran. The solution was then cast in a glass ring (37 mm

internal diameter) that was fixed on a glass plate. Slow evaporation was achieved by weighing down a sheet of glass on top of the ring.

5.1.2 Preparation of Ion Selective Electrodes (ISEs).

All ISEs except those used to lower the limits of detection in Section 2.6, were prepared as follows. Discs, 7 mm in diameter, were cut from the master membranes and mounted in standard electrode bodies supplied by Fluka. The inner electrolyte comprised of a 10^{-3} mol dm^{-3} solution of the relevant metal chloride salt. The electrodes were immersed over 24 h in a 10^{-2} mol dm^{-3} solution of the metal chloride salt for pre-conditioning prior to use. A schematic representation of a typical ISE is shown in Figure 5.2.

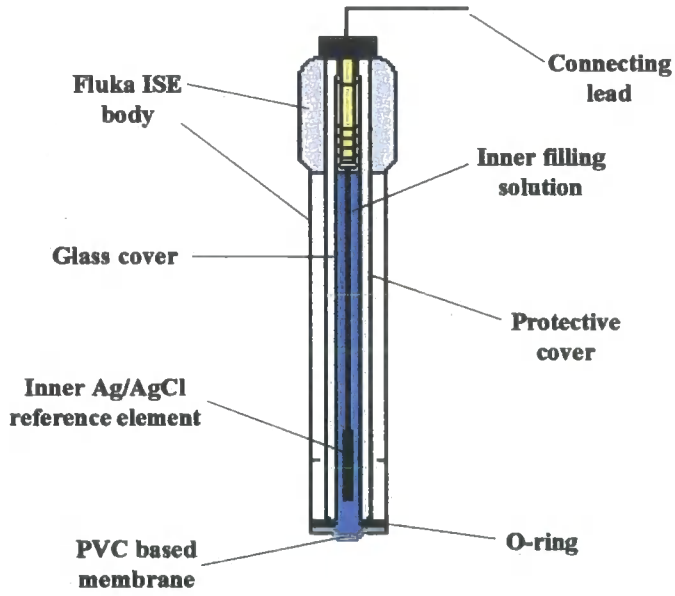

Figure 5.2: Schematic representation of a typical ISE.

5.1.3 Electrode Calibration.

Electrode calibration was performed at 298 K using a thermostatted cell. Calibration solutions of the metal chloride salt were prepared by serial dilution at decade intervals of concentration in the range of 10^{-1} to 10^{-3} mol dm^{-3}, and half-decade intervals of concentration in the range of 10^{-3} to 10^{-6} mol dm^{-3}. A series of calibrations were performed for each ISE in alternating ascending order (10^{-1} to 10^{-6} mol dm^{-3}, then the

reverse). Prior to immersion in each solution, the ISEs were rinsed with distilled water. EMF measurements were recorded on a Molspin Ltd 4 input voltmeter that was connected to a computer. All measurements were made against a double junction type Ag/AgCl external reference electrode. Activity coefficients were calculated using the reference Gamphi database.

5.1.4 Fixed Interference Method (FIM).

Selectivity coefficients, K_{ij}^{pot}, where i represents the primary ion and j the interfereing ion, were determined according to the Fixed Interference Method (FIM).[2] Measurements were recorded at 298 K using a thermostatted cell that incorporated an ISE and a double junction type Ag/AgCl external reference electrode. The response of the electrode was measured in a background of constant interfering ion (c_j = 0.1 mol dm^{-3}), while the concentration of the primary ion c_i was varied using the technique of constant volume dilution. A calibration plot of EMF vs. $-\log c_i$ in the presence of c_j (Figure 5.3) was then treated according to the following methodology to obtain K_{ij}^{pot}.

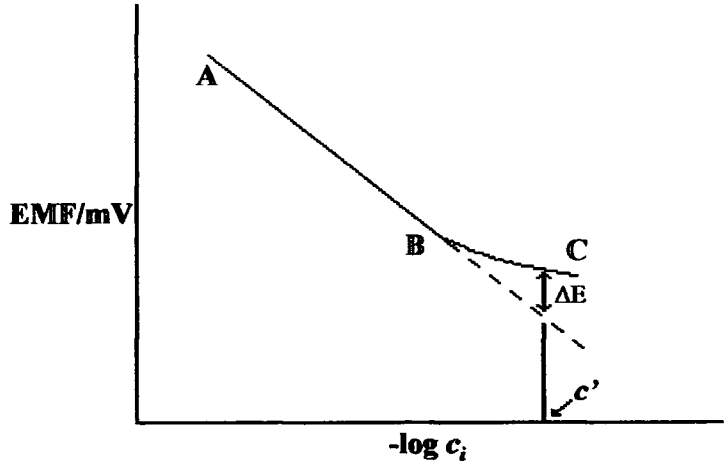

Figure 5.3: Calibration Plot of EMF vs. $-\log c_i$.

In mixed ion solutions the response of an ISE is not exclusive to one ion. At high concentrations of c_i the electrode, if behaving ideally should exhibit a Nernstian response (region AB) that is described by,

$$EMF_i = EMF^O + \frac{2.303RT}{z_i F}\log c_i \qquad \textbf{Equ 5.1}$$

At low concentrations (region BC) the presence of an interfering ion, c_j, can influence the response of the electrode. For c_i in the presence of c_j the electrode response is,

$$EMF' = EMF^O + \frac{2.303RT}{z_i F}\log\left(c_i + K_{ij}^{pot} c_j^{z_i/z_j}\right) \qquad \textbf{Equ 5.2}$$

At point c' where $c_i = c' = K_{ij}^{pot} c_j^{z_i/z_j}$, the difference in potential, ΔE, between the primary ion solution and the mixed ion solution, each with primary ion concentration, c', is:

$$\Delta E = EMF'-EMF_i = \frac{2.303RT}{z_i F}\log 2 \approx \frac{18.5}{z_i} mV \qquad \textbf{Equ 5.3}$$

When the experimental line BC deviates from the extrapolation of AB by $18.5/z_i$ mV at 298 K, the concentration of c_i' can be determined and then substituted into Equation 5.4, hence,

$$K_{ij}^{pot} = \frac{c_i'}{c_j^{z_i/z_j}} \qquad \textbf{Equ 5.4}$$

5.1.5 Constant Volume Dilution (CVD).

This technique was developed by *Horvai et al*[3] in 1975 for the purpose of electrode calibration and to determine electrode parameters such as selectivity. Compared to the SSM, the analysis time for electrode calibration using CVD is longer (typically 25 mins), and the slope factor determined for electrodes tend to be higher when compared with values obtained using the SSM. This can be attributed to the memory or hysteresis effect following contact between the membrane and ions in solution. Despite this

drawback, CVD is considered a superior technique to the SSM as it allows the performance of the electrode to be monitored in 'real world' environments such as those containing interfering ions.

A fixed volume of stirred solution containing both the primary ion, *i*, and interfering ion, *j*, (c_i = 0.1 mol dm^{-3} and c_j = 0.1 mol dm^{-3}), was continually diluted by a solution of the interfering ion (c_j = 0.1 mol dm^{-3}). Where the response of the Ca^{2+} ISE (**50/o**-NPOE, Section 2.4) was measured in the presence of a simulated extracellular backgroung of interfering ions, then c_j represents 140 mmol dm^{-3} Na^+, 4.3 mmol dm^{-3} K^+ and 0.9 mmol dm^{-3} Mg^{2+}. If the electrode responds in a Nernstian fashion, then the measured potential difference EMF, is proportional to logc_i (concentration in mol dm^{-3}), as long as the activity coefficient remains constant. The electrode will then produce a linear response of EMF versus time (t), and the relationship between the concentration and time can be derived as follows.

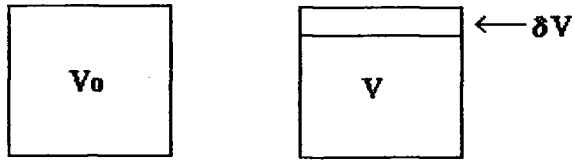

After a given time interval, volume δV is replaced with solution not containing the primary ion. The new concentration of the primary ion c_i', is given by Equation 5.5.

$$c_i' = \frac{c_i V}{Vo} = \frac{c_i (Vo - \delta V)}{Vo} \qquad \textbf{Equ 5.5}$$

Rearranging and substituting $\delta c_i = c_i' - c_i$ gives

$$\frac{\delta c_i}{c_i} = -\frac{\delta V}{V} \qquad \textbf{Equ 5.6}$$

If the dilution is continuous then $\delta V \longrightarrow dV$,

$$\frac{dc_i}{c_i} = \frac{dV}{V} \qquad \textbf{Equ 5.7}$$

If the flowrate is ω (m^3s^{-1}), then dV = ωdt. Substituting into Equation 5.7 and integrating gives,

$$\int_{c_{io}}^{c_i} \frac{dc_i}{c_i} = -\int_{o}^{t} \frac{\omega dt}{V_o} = \ln c_{io} - \frac{\omega t}{V_o} \qquad \textbf{Equ 5.8}$$

where c_{io} is the initial concentration of primary ion.

c_i is the concentration of primary ion at time t.

The graphs that are produced in the form of EMF versus t can be converted to the form of EMF versus $-logc_i$ using the following conversion,

$$-\log c_i = -\log c_{io} + \log\left(e^{-\omega t/V_o}\right) \qquad \textbf{Equ 5.9}$$

The constant volume dilution system is shown in Figure 5.4. A stable reading was obtained with the solution containing the primary ion before dilution commenced. The solution was drawn through the constant volume cell and past the frit of the T-junction reference electrode vessel and on to waste using a peristaltic pump (Gilson). The flowrate was measured by timing the filling of a 10 ml volumetric flask. This flowrate was used to calculate the volume of the constant volume cell by measuring the time required to fill it. The EMF response was measured on a Keithley 197 digital voltmeter (DVM) interfaced to a buffer amplifier and a Linseis chart recorder that gave a trace in the x-direction proportional to time, and in the y-direction proportional to EMF. Typical chart speed settings used were 200 mm hr^{-1} and the full scale deflection in the y-direction was 100 mV. All measurements were performed at 298 K using a thermostatted cell.

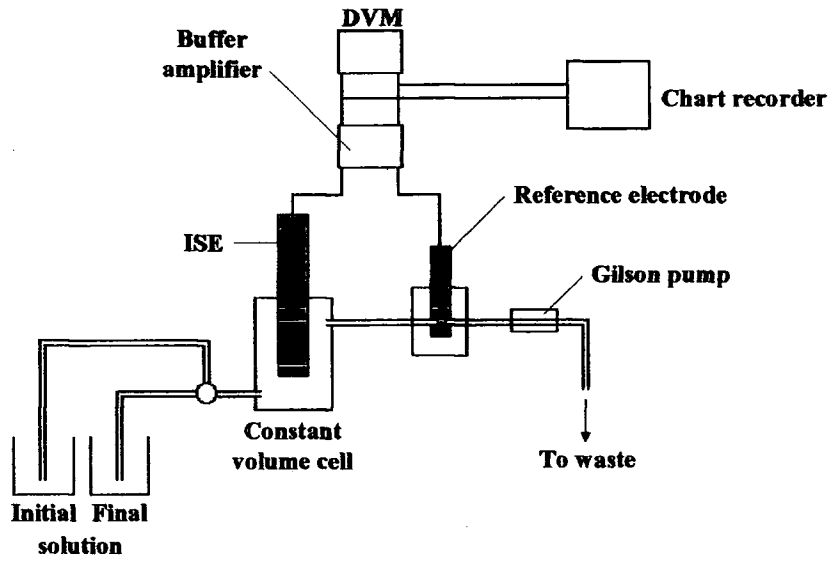

Figure 5.4: Experimental system for Constant Volume Dilution.

5.1.6 pH Measurement of Ca^{2+} ISEs.

The test solution composed of 10^{-3} mol dm^{-3} $CaCl_2$ and 10^{-1} mol dm^{-3} KCl, to maintain constant activity coefficients of the components. The initial pH of the solution was set to pH 3 following the addition of HCl. The pH was altered by adding small aliquots of either 0.1 or 1 mol dm^{-3} KOH. The temperature was maintained at 298 K using a thermostatted cell. A buffer amplifier interfaced to a Thurlby Thandler 1705 multimeter recorded the EMF. All measurements were made against a double junction type Ag/AgCl external reference electrode. The pH was recorded simultaneously using a combined glass electrode which was connected to a Molspin pH meter. The glass electrode was calibrated with pH 4, 7 and 10 reference buffer solutions that were purchased from Sigma.

5.1.7 Lowering the Detection Limits of Calcium ISEs.

Typical and modified ISEs incorporating a Ca^{2+} buffer solution were prepared and their ability to detect submicromolar concentrations of Ca^{2+} was investigated. The composition of the Ca^{2+} buffer[4] is shown in Table 5.1.

Components	Amount in 0.1 dm^3	Molarity/mol dm^{-3}
HEPES[a]	0.2383 g	9.9×10^{-3}
EGTA[b]	0.3804 g	10^{-2}
$CaCl_2$ hydrate	0.0557 g	5×10^{-3}
KOH (1M)	4.895 ml	4.9×10^{-2}
KCl (2M)	3.801 ml	7.6×10^{-2}
pH	9.25	
pCa^{2+}	≅10	

[a]HEPES: 4-(2-hydroxyethyl)piperazine-1-ethane-2-sulfonic acid. [b]EGTA: ethylene bis oxyethylenenitrilotetraacetic acid.

Table 5.1: Composition of Ca^{2+} buffer solution.

The PVC based membranes containing o-NPOE plasticizer and either the diisobutyl diamide ionophore **50** or ETH1001 **42**, were incorporated into ISE bodies to investigate their limits of detection for calcium. Discs, 7 mm in diameter, were cut from the master membranes and mounted in standard electrode bodies supplied by Fluka. The Ca^{2+} buffer solution described in Table 5.1 was the inner filling electrolyte that was in contact with the inner reference element (Ag/AgCl). In addition, a third ISE was prepared that incorporated the o-NPOE/**50** membrane. A voltammetric (Ag/AgCl in 3 mol dm^{-3} KCl) aqueous reference electrode supplied by Bioanalytical Systems Inc (reference number MF-2052), was used as the inner reference element. This was in contact with the Ca^{2+} buffer inner electrolyte solution through a 1 mol dm^{-3} KCl salt bridge. This modified ISE is shown in Figure 5.5. All ISEs were conditioned in 10^{-3} mol dm^{-3} $CaCl_2$ solution for two days.

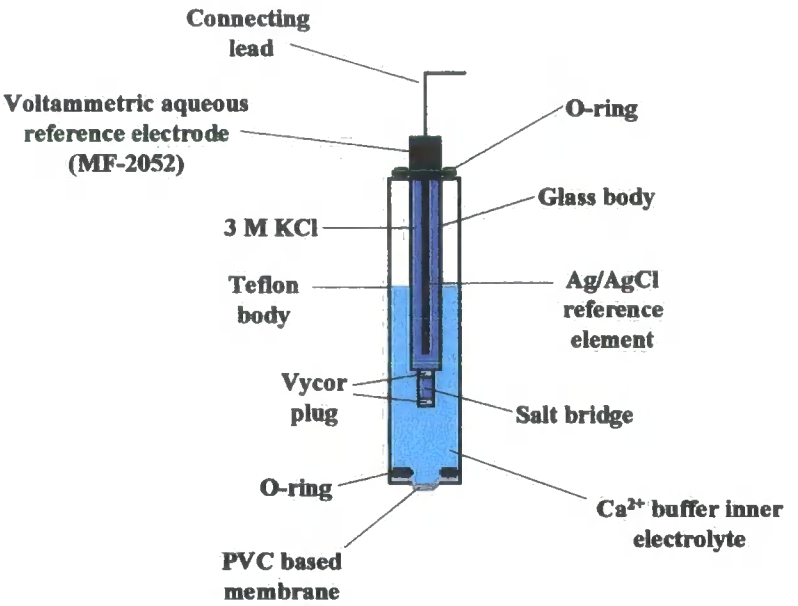

Figure 5.5: Schematic representation of a modified ISE incorporating a voltammetric (Ag/AgCl) aqueous reference electrode.

A buffer amplifier interfaced to a Keithley 197 digital voltmeter recorded EMF measurements. All readings were made against a double junction type Ag/AgCl reference electrode. EMF measurements were taken in serial diluted stock solutions of 10^{-1} mol dm^{-3} $CaCl_2$ from higher to lower concentrations. Prior to immersion in each solution, the ISEs were rinsed with distilled water. End potentials were taken when the drift in EMF was < 0.5 mV min^{-1} (approximately 20 minutes for concentrations down to 10^{-5} mol dm^{-3} $CaCl_2$, and approx. 40-50 minutes for lower concentrations). All measurements were recorded at 298 K using a thermostatted cell.

5.2 Experimental for Chapters 3-4, Optical pH and Dissolved Oxygen sensing.

5.2.1 General Instrumentation for Optical Sensing.

UV-visible absorbance spectra were recorded on a Pharmacia Biotech Ultrospec 4000 spectrometer operating with Swift II software. Luminescence measurements were performed on an Instrument SA Fluorolog 3-11 equipped with a SPX 1934D3 phosphorimeter. Corrected spectra were recorded to compensate for the wavelength-dependent efficiency of the instrument. Excitation and emission wavelengths were selected using single grating monochromators and the intensity was measured using a

Hamamatsu R928 photomultiplier tube. Spectral artifacts such as second order transmission and scattered excitation light were removed by using appropriate cut-off filters, although the latter could be observed in certain cases where flow-cell A (Section 5.2.2) was used, and required a double emission diffraction grating to remove it from the emission optics.

5.2.2 Flow Cells for Characterising Sol-Gel Films.

To characterize and allow the reversibility of the sensing films to be assesed, flow cells were designed that could be housed in the sample chambers of the fluorimeter. For Flow cell A (Figure 5.6), fluorescence was observed from the face of the sample that was illuminated with the excitation radiation. This geometrical set-up is often preferred where solid samples, thin films and optically thick samples such as whole blood are being investigated[5]. Illumination of the cell was at an angle of 35° to the excitation beam. This angle of incidence was chosen to reduce the amount of incident light that was reflected off the face and into the emission optics.[6]

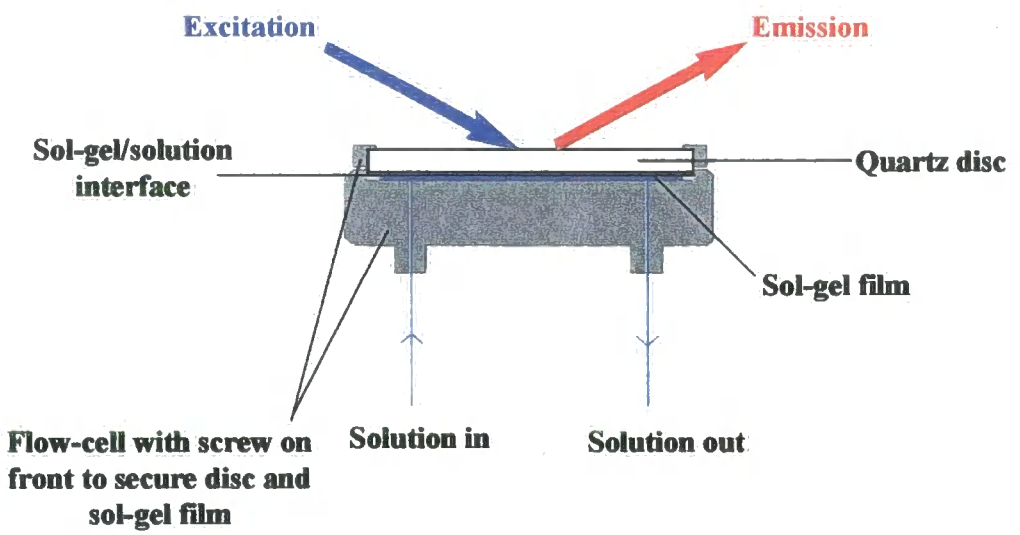

Figure 5.6: Schematic representation of flow-cell A showing front face excitation and emission of a sol-gel film.

The optimized flow cell B (Figure 5.7) used observation at 90° to a centrally illuminated film. This geometrical set-up exploited the anisotropic nature of fluorescence emission

and used internal reflection to capture and guide the emitted luminescence towards the detector. Details of similar cell designs can be viewed elsewhere.[7,8,9]

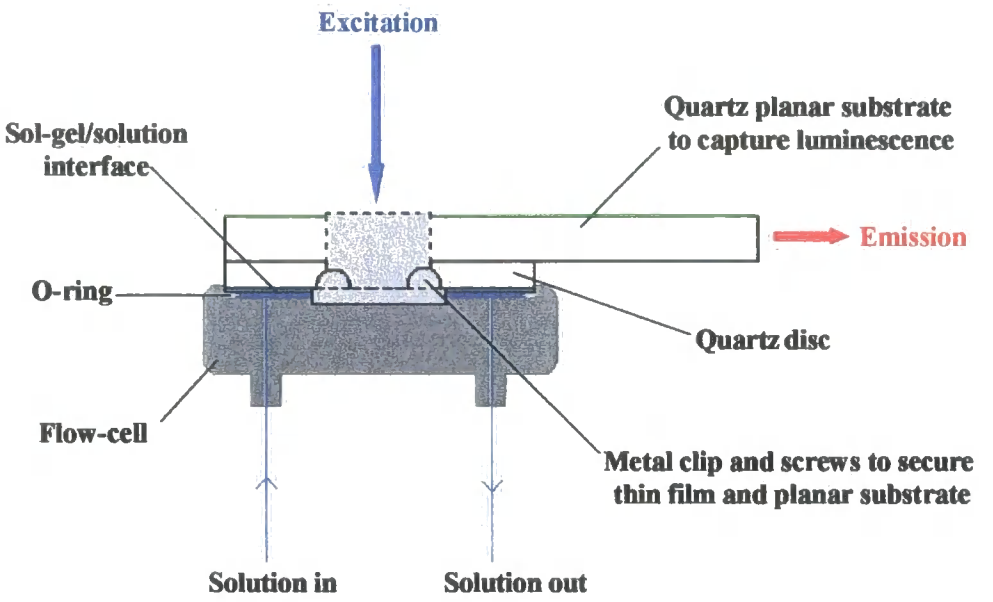

Figure 5.7: Schematic representation of flow-cell B showing right angle observation of a centrally illuminated sol-gel film.

When crossing an interface into a medium of a higher refractive index, light will bend towards the normal. Conversely, light travelling across an interface from a higher to lower refractive index will bend away from the normal. At some angle, known as the critical angle θ_c, light travelling from a medium with higher refractive index into a medium with lower refractive index will be refracted at 90° along the interface. If the angle of incidence at the interface is greater than the critical angle, then the light experiences total internal reflection instead of refraction.[10] A schematic representation of total internal reflection is shown in Figure 5.8.

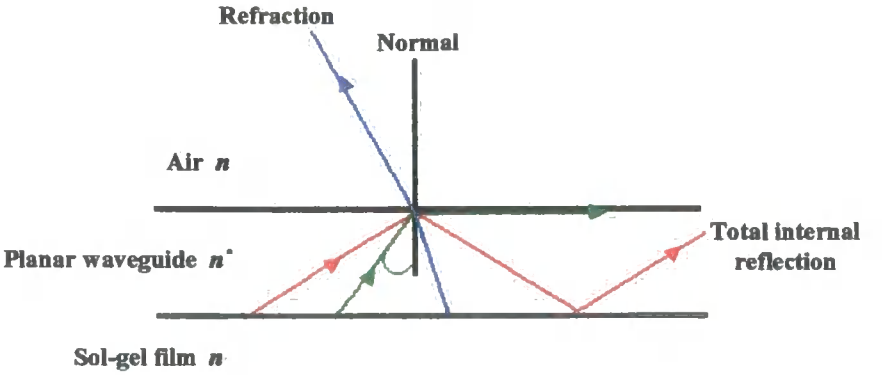

$$\sin\theta_c = \frac{n}{n^*} \quad n^* > n$$

Figure 5.8: Schematic representation of total internal reflection.

Compared to the 'face-on' observation set up of flow-cell A, the use of the quartz planar substrate in flow-cell B, to act as a waveguide coupled to right angle observation, led to a 10-fold enhancement of measured signal intensity. Flow-cell B was therefore used when recording luminescence intensity decay measurements. Emission slits as narrow as 1 nm was used with flow-cell B allowing good spectral resolution to be achieved without compromising adequate signal intensity.

5.2.3 Preparation of Sol-Gel Films For Optical pH Sensing.

The silicon alkoxide precursor tetramethoxysilane (TMOS) was purchased from Aldrich and the polished quartz discs (25 mm diameter, 2 mm thickness) were purchased from Multilab, Newcastle upon-Tyne, UK. Water and H_2O refer to high purity water with conductivity $\leq$ 0.4 μScm^{-1}, obtained from the PURITE^{TM} purification system. The standard film fabrication process involved mixing TMOS (100 µl) with methanol and acidified water (using HCl as catalyst). The molar ratio of water to silicon alkoxide (R) was either 2, 3 or 4, and the methanol to TMOS molar ratio was varied between 2 and 4.5. After stirring for 40 minutes at 295 K the appropriate lanthanide complex was added and the solution was stirred for between 1-6 hours. This ageing period was to promote hydrolysis and allow condensation in the sol. Typical concentrations used were 15 mmol dm^{-3} for complexes **58** and **59**, 7.5 mmol dm^{-3} for complex **60**, and 5 mmol dm^{-3} for complexes **55**, **56** and **57**. Thin films were cast by dropping 100 µl of

the sol solution onto one side of a rotating quartz disc. Prior to spin-coating, the quartz substrates were placed overnight in conc. HNO_3 to activate the surface of the quartz, and then cleaned sequentially using water and ethanol. All films were spun at 2400 rpm using a Cammex Precima PRS14E spin-coater. After coating, all films were left in ambient laboratory conditions to stabilise for a period up to 28 days prior to analysis. This was to allow structural changes within the sol-gel matrix to evolve.[11] All membrane compositions are summarized in Table 5.2.

Complex immobilised in sol-gel film	TMOS: H_2O	TMOS: MeOH	Ageing (hours)	Stabilization (days)	Concentration of complex/mmol dm^{-3}
55	1:2	1:3.3	6	28	5
56 (1)	1:2	1:3.3	6	28	5
56 (2)	1:4	1:3	6	28	5
57 (1)	1:2	1:3.3	6	28	5
57 (2)	1:4	1:3	6	28	5
58	1:3*	1:2.2	2	14	15
59	1:4*	1:4.5	7	28	15
60	1:4*	1:4.5	6	28	7.5

*0.04 mol dm^{-3} HCl, (0.1 mol dm^{-3} HCl for all other films).

Table 5.2: Composition, aging and stabilization time of sol gel films for pH sensing.

5.2.4 Buffer Solutions for pH Sensing.

pH measurements were made using a Jenway 3320 pH meter (fitted with a combination glass electrode–microsample), calibrated with pH 4, 7 and 10 reference buffer solutions that were purchased from Sigma.

Sulfonic acids 2-[N-Cyclohexylamino]ethanesulfonic acid (CHES), 3-[N-Morpholino]propanesulfonic acid (MOPS) and 2-[N-Morpholino]ethanesulfonic acid (MES) were purchased from Sigma. The series of zwitterionic biological buffer solutions ranging from pH 5.5 to 10 (0.25-0.5 pH increments) were prepared at 0.1 mol dm^{-3} concentration of the free acid using 0.1 mol dm^{-3} NaOH to adjust the pH. To

sustain constant solution-solution and solution-sol gel film interfaces, the ionic strength of the buffer solutions was held constant at 100 mmol dm^{-3} or 20 mmol dm^{-3} using NaCl.[12] HCl dilutions were used to set the pH at pH $\leq$ 5. Their ionic strength was set in the same way. The solutions were pumped through the flow cell at a rate of 4 ml min^{-1} using a peristaltic pump (Gilson). All solutions were air saturated.

5.2.5 pH Measurements of Sol-Gel Films.

Spectra were recorded approximately 5 minutes after changing the pH of the solution and then at intervals typical of 10, 15 and 20 minutes to ensure the signal was stable. The excitation and emission wavelengths used in this work are shown in Table 5.3, as are the excitation and emission slit widths. Spectra were recorded at a 0.5 nm interval with a 0.25 s integration time. For response time and reversibility measurements, good signal to noise levels were achieved by using an increment of 2 and 25 seconds respectively, for the integration setting. The intensity data were fitted to the equation shown in Appendix I (using a non-linear iterative least squares fitting procedure operating on Excel® software), to determine protonation constants.

Complex immobilised in sol-gel film	λ_{ex} (nm)	λ_{em} (nm)	Excitation slit (nm)	Emission slit (nm)
55	365	617	25	2
56 (1)	311	544	10	1
56 (2)	311	544	3	1
57 (1)	311/370*	548**	3	1
57 (2)	311/370*	548**	3	1
58	265	547	15	4
59	265	544 544/549*	25	2
60	330	615	7	1

* Chosen wavelengths for ratiometric sensing. **Emission was monitored at this wavelength during the excitation scan.

Table 5.3: Excitation and emission parameters.

5.2.6 pH Titrations in Homogeneous Solution.

pH titrations of complexes **58** and **59** were carried out in a background of constant ionic strength (I = 0.1 mol dm^{-3} NaCl, 295 K). For luminescence measurements solutions with absorbances of < 0.1 at wavelengths ≥ λ_{ex} (where λ_{ex} = 265 nm) were used to avoid any errors due to the inner filter effect. Solutions were basified by the addition of 1 mol dm^{-3} NaOH and titrated to acidic pH using small aliquots (typically 0.5 μL) of either 1 mol dm^{-3} or 0.1 mol dm^{-3} HCl. Spectra were recorded for each respective pH using an increment of 0.5 nm and 0.25 s for the integration setting. Excitation and emission slits of 1.5 and 1 nm were used respectively. The intensity data were fitted to the equation shown in Appendix I (using a non-linear iterative least squares fitting procedure operating on Excel® software), to determine protonation constants.

5.2.7 Preparation of Sol-Gel Films for Dissolved Oxygen Sensing.

Sol-gel films were produced by adding acidified water (0.1 mol dm^{-3} HCl) to a solution of ethanol and ethyltriethoxysilane (ETEOS). The molar ratios of the precursors used to fabricate the films were based on sol-gel film preparations for dissolved oxygen sensing described by *MacCraith et al.*[13] The molar ratio of water to ETEOS (R) was either 2 or 4. All films were prepared with an ethanol to ETEOS molar ratio of 8. Following stirring of the sol at 295 K for 40 minutes, the relevant Tb complex was added (5 mmol dm^{-3}). The sol was then aged at 295 K for a fixed period. During this ageing period the sol was stirred. Films were cast as described in Section 5.2.3, then left to stabilise in ambient laboratory conditions to allow structural changes within the sol-gel matrix to evolve.[11] Details of membrane compositions are summarized in Table 5.4.

Complex immobilised in sol-gel film	ETEOS: H_2O	ETEOS: EtOH	Ageing (hours)	Stabilisation (days)	Concentration of complex/mmol dm^{-3}
61	1:2	1:8	4	126	5
62	1:2	1:8	26	75	5
62	1:4	1:8	26	75	5

Table 5.4: Composition, ageing and stabilisation time of sol-gel films for dissolved oxygen sensing.

5.2.8 Dissolved Oxygen Sensing.

Aqueous dissolved oxygen measurements were made using a Jenway Dissolved Oxygen meter model 9150. Prior to usage, a two-point calibration was preformed in which the probe was immersed in a 0.16 mol dm^{-3} solution of sodium sulphite to obtain a 0% dissolved oxygen reading. The probe was then rinsed with clean water and placed approximately 1 cm above a beaker of clean water to obtain a 100% dissolved oxygen reading. The experimental set-up used for dissolved oxygen sensing is shown in Figure 5.10. Sol-gel films incorporated into flow-cell B were exposed to water (flow-rate 4 ml min^{-1}) of a defined dissolved oxygen concentration. Using a peristaltic pump, the water was passed continuously round a closed flow system via a mixing chamber where the water was purged with argon and oxygen. Water and gases were stirred vigorously using a magnetic stirrer. Different dissolved oxygen concentrations were produced using fine needle valves to control the gas flow rate from the gas regulators to the mixing vessel. The dissolved oxygen sensing probe was immersed in the water inside the chamber to monitor the dissolved oxygen concentration which was displayed on the portable display meter attached to the probe.

Spectra were recorded when measuring the metal-based emission approximately 5 minutes after the concentration of dissolved oxygen in the water had stabilised (as indicated by a stable reading on the portable display attached to the dissolved oxygen probe), and then at intervals typical of 10 and 15 minutes to ensure the signal was stable. Excitation and emission wavelengths corresponding to λ_{ex} = 330nm and λ_{em} 547 nm were used. Excitation slits were set at 7 nm bandpass for the sol-gel film incorporating **61**, and 10 nm bandpass for the sol-gel films incorporating **62**. The emission slits were 2 nm and 3 nm bandpass respectively. All spectra were recorded using an increment of 0.5 nm and 0.25 s for the integration setting.

Intensity decay data were recorded following the excitation of the sol-gel films by a short flash of light (λ = 330 nm). The integrated intensity of emitted light (λ = 547 nm) was recorded following an initial delay of 0.01 ms, and then at delay times of t_d (t_d = 0.05 ms for the sol-gel films incorporating **61** or **62** where R = 2, t_d = 0.1 ms for the sol-gel film incorporating **62** where R = 4). The sampling window was set at 15 ms. The

time between flashes was set to 40 ms and the total number of flashes was 500. A schematic representation of the typical sequence of data acquisition is shown in Figure 5.9. Excitation and emission slits were set at 20 nm bandpass and 10 nm bandpass for the film incorporating complex **61**, and 25 nm bandpass and 20 nm bandpass for the films incorporating complex **62** respectively. Measurements were recorded approximately 7 minutes after the concentration of dissolved oxygen in the water had stabilised (as indicated by a stable reading on the portable display attached to the dissolved oxygen probe). All measurements were performed at 295 K. The analysis of the lifetime data for calibration purposes is described in Section 4.5.

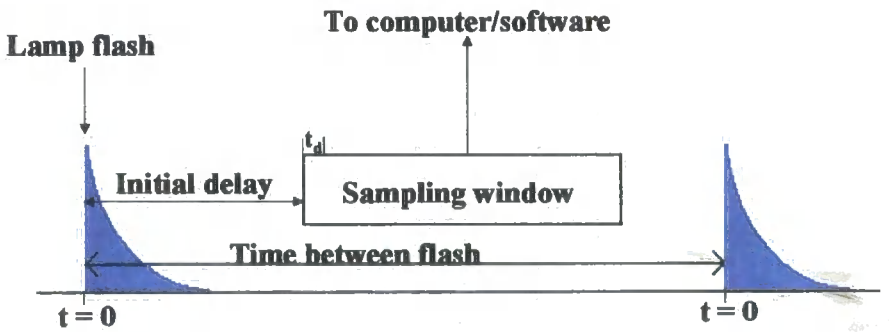

Figure 5.9: data acquisition timing sequence.

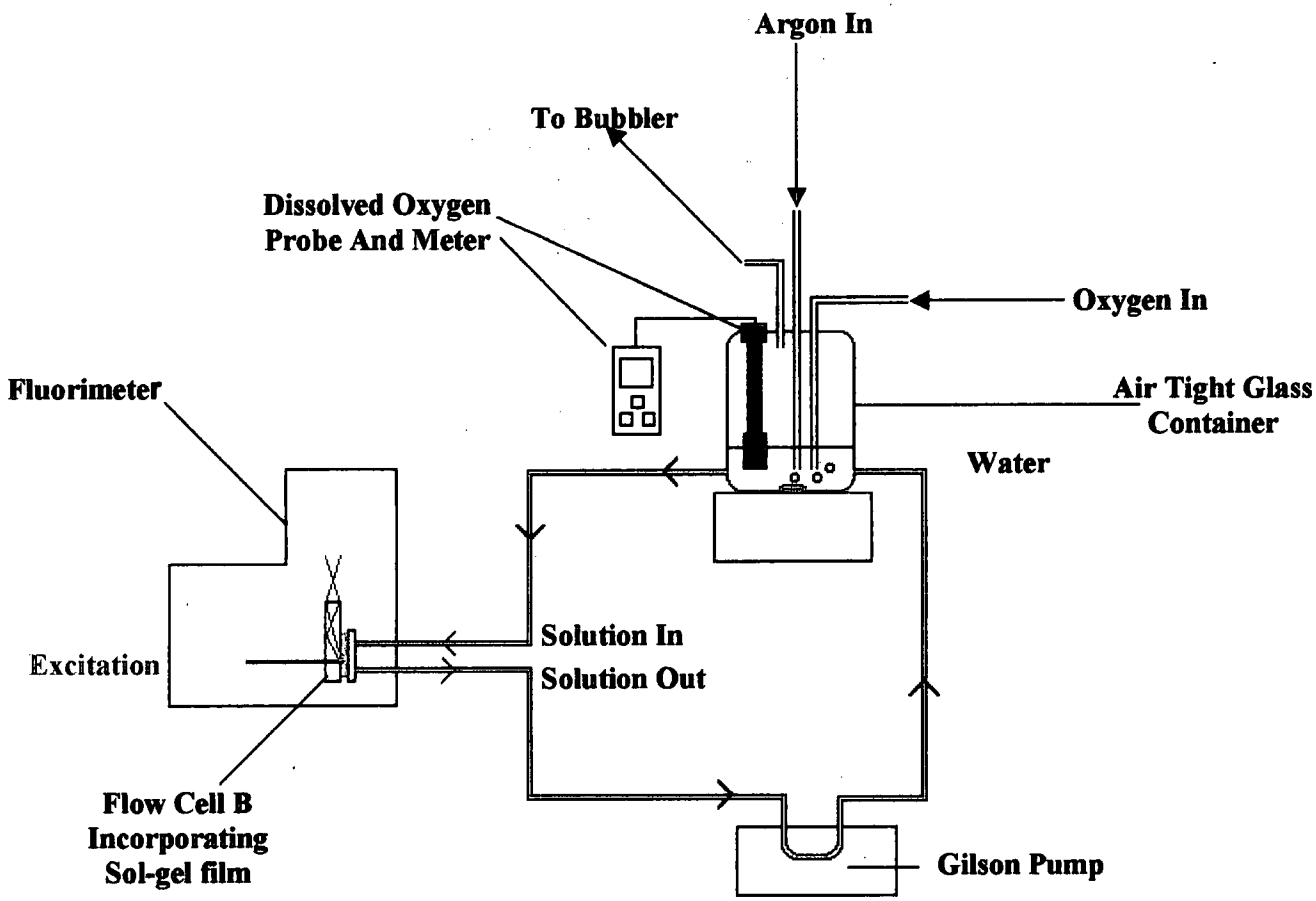

Figure 5.10: Schematic representation of apparatus used for dissolved oxygen sensing using sol gel film.

5.3 References for Chapter 5.

[1] Goodall M., Kelly P. M., Parker D., Gloe K., Stephan H., *J. Chem. Soc., Perkin Trans. 2*, 59 1997.
[2] Yoshio U., *Pure and Applied Chemistry.* **67**, 507, 1995.
[3] Horvai G., Toth K., Pungor E., *Anal. Chim. Acta.* **82**, 45, 1976.
[4] Schefer E., Ammann D., Pretsch E., Oesch U., Simon W., *Anal.Chem.* **58**, 2282, 1986.
[5] Lakowicz J. R., *Principles of Fluorescence Spectroscopy.* 2nd Edn., Kluwer Academic/Plenum Publishers, New York 1999.
[6] Eisinger J., FloresJ., *Anal. Biochem.* **94**, 15, 1979.
[7] Malins C., Glever H.G., Keyes T. E., Vos J. G., Dressick W. J., MacCraith B. D., *Sensors and Actuators.* **67**, 89, 2000.
[8] Geddes C. D., Douglas P., Moore C. P., Wear T. J., Edgerton P. L., *Meas. Sci. Technol.* **10**, N34, 1999.
[9] Gouin J. F., Doyle A., MacCraith B. D., *Electronic Letters.* **34**, 1685, 1998.
[10] Hecht E., OPTICS, 3rd Edn, Addison-Wesley-Longman Inc. 1998.
[11] Kimura K., Yajima S., Takase H., Yokoyama M., *Anal. Chem.* **73**, 1605, 2001.
[12] Geddes C. D., Douglas P., Moore C. P., Wear T. J., Edgerton P. L., *Journal of Flourescence.* **9**, 163, 1999.
[13] McDonagh C., MacCraith B. D., McEvoy A. K., *Anal. Chem.* **70**, 45, 1998.

Appendix I

Determination of apparent protonation constants of sol-gel immobilised complexes, from luminescence data.

The protonation of the immobilised complex was obtained by monitoring the pH-dependent change in luminescence intensity. The experimental data was then fitted to an expression to estimate the apparent pK_a. The derivation of this expression is shown;

The observed luminescence at any point during the pH titration comprises of the luminescence from the protonated and deprotonated forms, which depends on their mole fractions in the solution. This is represented in Equation 1.

$$I_{obs} = \alpha_{A^-} I_{A^-} + \alpha_{HA} I_{HA} \qquad \textbf{Equ.1}$$

I_{obs} Observed intensity.

I_{A^-} Intensity of complex when deprotonated.

I_{HA} Intensity of complex when protinated.

α denotes the mole fractions

$$\alpha_{A^-} = \frac{[A^-]}{[A^-]+[HA]} \qquad \textbf{Equ.2} \qquad\qquad \alpha_{HA} = \frac{[HA]}{[A^-]+[HA]} \qquad \textbf{Equ.3}$$

Substitution of Equation 2 and 3 into Equation 1, and rearrangement;

$$[A^-] = [HA]\frac{(I_{HA} - I_{obs})}{(I_{obs} - I_{A^-})} \qquad \textbf{Equ.4}$$

From the acid-base equilibrium;

$$[HA] \underset{}{\overset{K_a}{\rightleftharpoons}} [A^-]+[H^+]$$

$$[A^-] = \frac{K_a[HA]}{H^+}$$ **Equ.5**

Substitution of Equation 5 into Equation 4 and rearrangement;

$$I_{obs} = \frac{I_{A^-}K_a + I_{HA}[H^+]}{[H^+] + K_a}$$ **Equ.6**

Equation 6 was used to calculate the intensity (I_{calc}) at any point in the titration, in terms of I_{A^-}, I_{HA}, $[H^+]$, and K_a. The experimental intensity data (I_{obs}) was then fitted to this expression by varying K_a. This allowed the estimation of the apparent K_a for the sol-gel immobilised lanthanide pH-responsive complexes.

List of Publications.

Reany O., Blair S., Kataky R., Parker D., Solution complexation behaviour of 1,3,5-trioxycyclohexane based ligands and their evaluation as ionophores for Group IA/IIA metal cations. *J. Chem. Soc., Perkin Trans. 2,* 623-630, 2000.

Skinner P. J., Blair S., Kataky R., Parker D., A rotaxane of a 1,1'-disubstituted ferrocene and beta-cyclodextrin. *New. J. Chem., 24, 265-268, 2000.*

Blair S., Lowe M. P., Mathieu C. E., Parker D., Senanayake P. K., Kataky R., Narrow-range optical pH sensors based on luminescent europium and terbium complexes immobilised in a sol-gel glass. *Inorganic Chemistry, 40, 5860-5867, 2001.*.

Parker D., Bruce J. I., Blair S., Lowe M. P., Excitement in F-block: responsive lanthanide complexes. *J. Inorg. Biochem., 86, 84-84, 2001.*

Blair S., Kataky R., Parker R., Sol-gel immobilised terbium complexes for luminescence sensing of dissolved oxygen by analysis of emission decay. *New. J. Chem., Submitted for publication.*